2011

In-wheel Motors: Express Comparative Method for PMBL Motors

Pavani Gottipati
Louisiana State University and Agricultural and Mechanical College

IN-WHEEL MOTORS: EXPRESS COMPARATIVE METHOD FOR PMBL MOTORS

A Dissertation
Submitted to the Graduate Faculty of the
Louisiana State University and
Agricultural and Mechanical College
in partial fulfillment of the
requirements for the degree of
Doctor of Philosophy

in

The Department of Electrical and Computer Engineering

by
Pavani Gottipati
Bachelor of Technology, Andhra University, 2004
MSEE, Louisiana State University, 2007
May 2011

DEDICATION

This dissertation would not have been possible without the endless support from:

My Baby Boy, Suchir Narra
who missed his mom for countless hours, days and nights

My Husband, Vamsi Chandra Narra
who always believed that I would succeed in everything I do

My Mother, Ratnamala Gottipati
who motivated me to pursue a higher education

My Father, Subhash Babu Gottipati
who inspired me to become an electrical engineer

My Advisor, Ernest A. Mendrela
who always stood by me during my graduate studies and mentored me

ACKNOWLEDGEMENTS

I would like to express my gratitude to my advisor and mentor, Dr. Ernest A. Mendrela, for being a constant source of encouragement during all the years of my graduate school.

I would like to thank Dr. Leszek Czarnecki and Dr. Hsiao-Chun Wu not only for being a part of my dissertation committee, but also for providing valuable guidance in and out of class during my graduate studies. I would also like to thank the other dissertation committee members, Dr. Shahab Mehraeen, Dr. Sitharama Iyengar and Dr. Dirk Vertigan for their valuable time and suggestions in preparing this dissertation.

I would like to thank my brother, Satheesh S. Gottipati and my sister-in-law, Vidya Gottipati for all the time they spent with me when I needed them the most.

This work was supported by the National Science Foundation under Grant ECCS - 0801671: “Collaborative Research: High-Efficiency Gearless Power Conversion Systems with Silent Permanent-Magnet Machines”.

TABLE OF CONTENTS

LIST OF TABLES

LIST OF FIGURES

ABSTRACT

One of the challenges facing the electric vehicle industry today is the selection and design of a suitable in-wheel motor. Permanent Magnet Brushless (PMBL) motor is a good choice for the in-wheel motor because of its lossless excitation, improved efficiency, reduced weight and low maintenance. The PMBL motors can be further classified as Axial-Flux Twin-Rotor (AFTR) and Radial-Flux Twin-Rotor (RFTR) machines.

The objective of this dissertation is to develop a fast method for the selection of appropriate in-wheel motor depending on wheel size. To achieve this, torque equations are developed for a conventional single-rotor cylindrical, twin-rotor axial-flux and twin-rotor radial-flux PMBL motors with slot-less stators based on magnetic circuit theory and the torque ratio for any two motors is expressed as a function of motor diameter and axial length. The theoretical results are verified, on the basis of magnetic field theory, by building the 3-dimensional Finite Element Method (FEM) models of the three types of motors and analyzing them in magnetostatic solver to obtain the average torque of each motor. Later, validation of software is carried out by a prototype single-rotor cylindrical slotted motor which was built for direct driven electric wheelchair application. Further, the block diagram of this in-wheel motor including the supply circuit is built in Simulink to observe the motor dynamics in practical scenario.

The results from finite element analysis obtained for all the three PMBL motors indicate a good agreement with the analytical approach. For twin-rotor PMBL motors of diameter 334mm, length 82.5mm with a magnetic loading of 0.7T and current loading of 41.5A-turns/mm, the error between the express comparison method and simulation results, in computation of torque ratio, is about 1.5%. With respect to the single-rotor cylindrical motor with slotless stator,

the express method for AFTR PMBL motor yielded an error of 4.9% and that of an RFTR PMBL motor resulted in an error of -7.6%. Moreover, experimental validation of the wheelchair motor gave almost the same torque and similar dynamic performance as the FEM and Simulink models respectively.

CHAPTER 1: INTRODUCTION

1.1 Overview of Dissertation

The field of electric motors is a vast area to study. The applications for motors range from domestic to industrial such as fans, compressors, pumps, powered wheelchairs, electric vehicles, elevators, escalators, trams and the latest hybrid cars. Various industries that have commercial use of electric motors are automobile, aerospace, petroleum, manufacturing, etc. The nature of application dictates which kind of electric motor is to be used.

The primary classification of electric motors can be stated as DC motors and AC motors. The detailed classification of motors can be seen in Fig. 1.1.

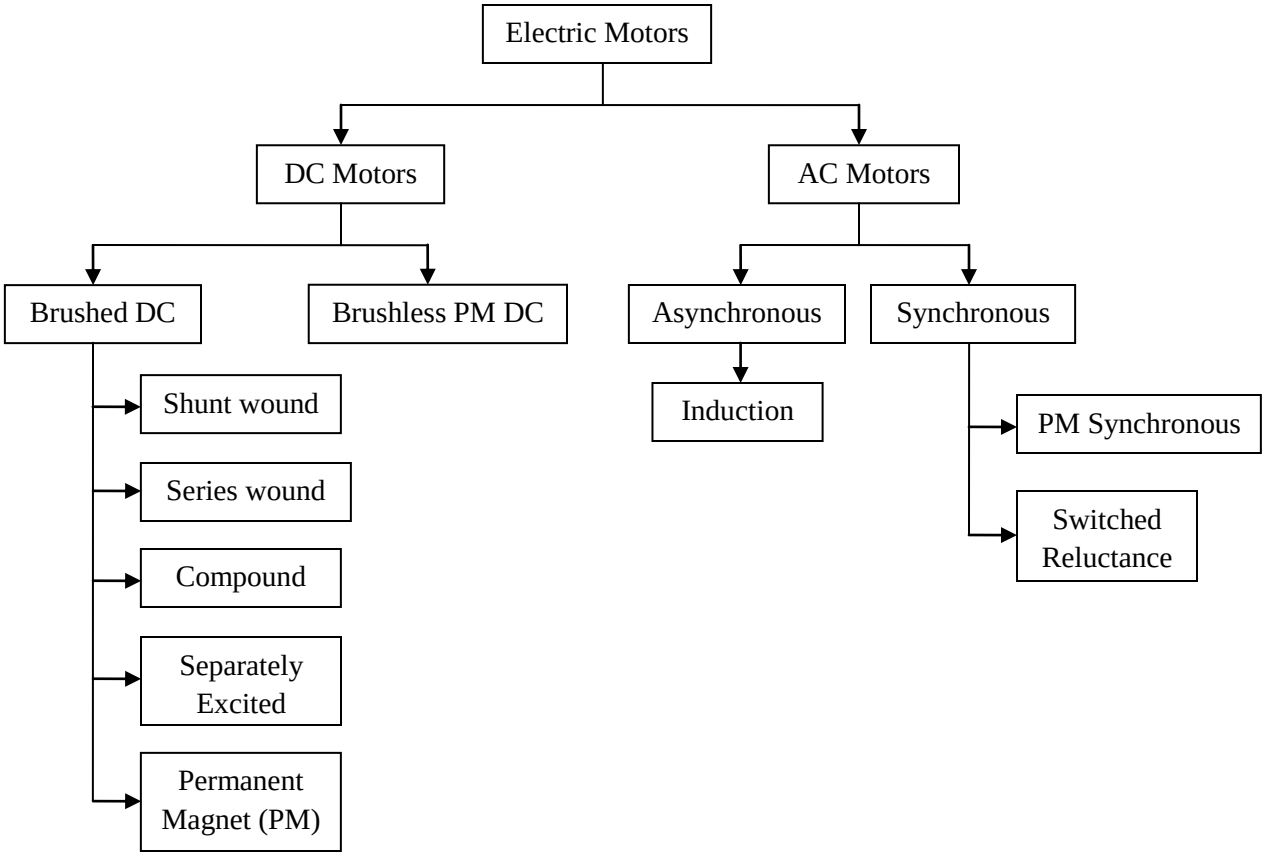

Fig. 1.1. Classification of electric motors

DC machines are generally less reliable and more expensive than their AC counterparts, because of the inherent need for a mechanical or electronic commutator. Hence, AC machines can be found in many applications; however a gear is required between the motor and load to reduce the high speed of these motors while operating at rated power. This results in increased cost and size of the drive simultaneously reducing the efficiency and reliability of the overall system. Gearless drives with brushless DC motors in fact operate similar to AC machines and serve as a good alternative for fractional-power applications. Induction motors, switched reluctance motors, permanent magnet dc motors and permanent magnet synchronous motors are among the most popular motors. As said earlier, the choice of motor depends on the application.

In the past few decades, electric motors have been the subject of in-wheel motors for electric vehicles (EVs). Besides electric and hybrid cars, electric drives of Motorized Personal Vehicles (MPVs) such as wheelchairs, electric scooters, electric carts for shopping, transportation and amusement employ electric motors. Practically, there are no commercial applications of in-wheel motors. These motors are mostly found only in the prototype versions of electric vehicles, as shown in Fig. 1.2(b). One of the obstacles for commercial use of in-wheel motors is the unsprung mass in the wheel. In-wheel motors for low speed vehicles are proposed in this dissertation. However, a few prototypes can be found in high speed vehicles, for example, army and military vehicles. Traditional MPVs employ mechanical gears between motors and main wheels. Fig. 1.2(a) shows the geared drive for electric vehicle application. Typically, two traditional DC motors drive the main wheels via mechanical transmission. The transmission is necessary to match the high-speed, low-torque motor with the low-speed, high-torque load. Application of high-speed motor results in relatively high efficiency and low volume of machine but the transmission itself reduces the overall drive efficiency besides adding extra cost to the

manufacturing and maintenance of MPV. Also, the same PM machine developed for use as a motor in an MPV can be used as low-speed electric generator in low-power wind energy system or for small Hydroelectric Power Plants (HPPs). This is a significant contribution especially in light of exploration for Renewable Energy (RE) sources.

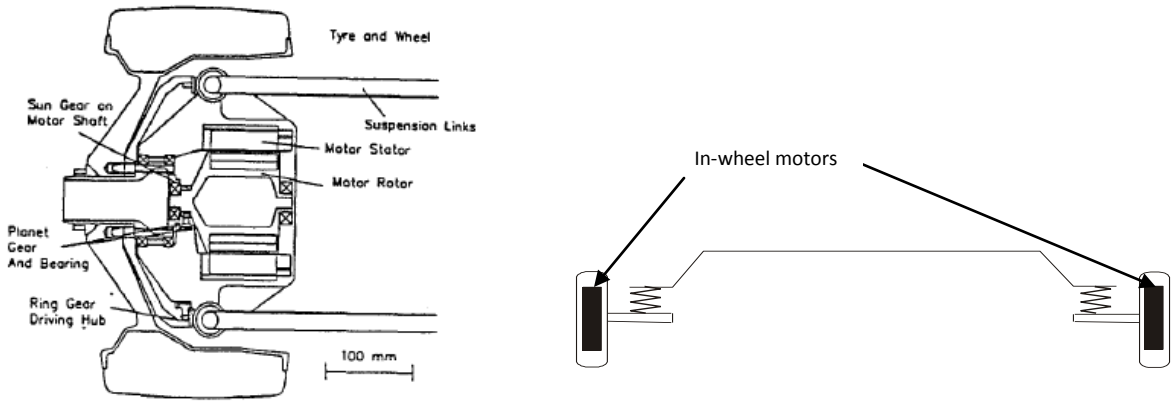

Fig. 1.2. (a) Traditional geared drive for an all-electric racing vehicle application [1], (b) In-wheel motors for the gearless electric drive of an EV

The hub-in motors or in-wheel motors are highly preferred for electric vehicle applications because of lower transmission losses, which results in better performance of the overall system, and low unsprung mass of the vehicle. These motors are impressive as they eliminate mechanical parts like gear trains and reduce the complexity as well as mass of the vehicle, not to mention the maintenance requirements. In-wheel motors demand high torque density, fast torque response to changing load conditions, high power density, high efficiency, low torque ripple, compactness in size and low mass. They should be able to provide high torque at low speed for start-up and acceleration and high power at high speed for cruising. Higher torque can be obtained with a larger motor size and volume, by providing more iron and copper for the flux linkages. However, the electric vehicles demand compact motors simultaneously

satisfying the high torque requirements giving rise to the optimization problem in the design of motors. Hence the selection and design of an appropriate motor for electric vehicles is a challenging issue. For indirect-drives, the maximum motor speed depends on maximum vehicle speed, wheel radius and gear ratio. However, for direct-drives, maximum motor speed depends only on the former two parameters [2]. In general, the operating requirements for MPVs can be listed as follows:

1. High power efficiency for a long range of the vehicle on a single battery charge
2. High starting torque necessary to negotiate road obstacles such as bumps, curbs and ramps
3. Smoothly running motor (low torque ripple) to ensure riding comfort of the passenger
4. Simplicity and versatility of control, including the remote control option
5. Low weight of drive for easy handling of MPV, for example, carrying it on stairs
6. Low cost of the drive for wide affordability of MPV
7. High reliability and low maintenance costs
8. Low acoustic noise and low electromagnetic interference

A few motors that can be sought for electric vehicle application are switched reluctance motors, induction motors, permanent magnet brushed and Permanent Magnet Brushless (PMBL) motors. Xue [2] carried out a detailed study to find which motor drive is appropriate for electric vehicles. The PM brushed DC motors are easy to be controlled and their speed-torque characteristic shows that we can obtain a high torque at low speed. The disadvantage of these motors is their bulky construction leading to heavy mass and periodic maintenance of mechanical brushes. Also, the maximum motor speed is restricted by the friction between commutator and brushes. Induction motors (IM), on the other hand, have simple construction and

need less maintenance. The maximum speed is not limited by brush friction and speed variation can be obtained by changing the supply voltage frequency as well as flux weakening. But, Field-Oriented Control (FOC) demands increased size of motor. Induction motors have lower efficiency than PM motors and Switched Reluctance Motors (SRM). SRMs are poor in terms of torque ripple and acoustic noise, but are simple to control, have high starting torque, weigh less and are suitable for high speed operations. However, torque ripple of the motor relates to the smoothness of the electric vehicle and thus is an important factor.

PMBL DC motors have lossless excitation and thus no rotor winding and rotor copper losses leading to higher efficiency than IM, SRM and PM brushed DC motor. As in the case of induction motors, the speed range of PMBL DC motors can be increased due to the absence of brushes. PMBL motors are also known for their low torque ripple and high power density. Further, the rotor discs act as natural fans making the heat dissipation easier. Needless to mention, PMBL motors make a good choice as in-wheel motors for the electric vehicle applications. This might sound as an easy conclusion, but the complication arises when one has to choose a particular PMBL motor design.

PMBL motors can be classified based on their construction and design variation. A simple classification is shown in Fig. 1.3. Further, the motors can have conventional slotted stator or slot-less (surface-wound) stator. The teeth on a slotted stator give rise to a significant value of cogging torque whereas the slot-less stator has a minimal torque ripple. The design factors that influence the torque ripple of a motor are discussed in Chapter 2. As seen from Fig. 1.3, the PMBL motors can be single-sided or double-sided. Also rotor structure varies depending on how the PM is placed on the rotor core. The detailed description of the PMBL motors and their classification is given in subsequent chapters.

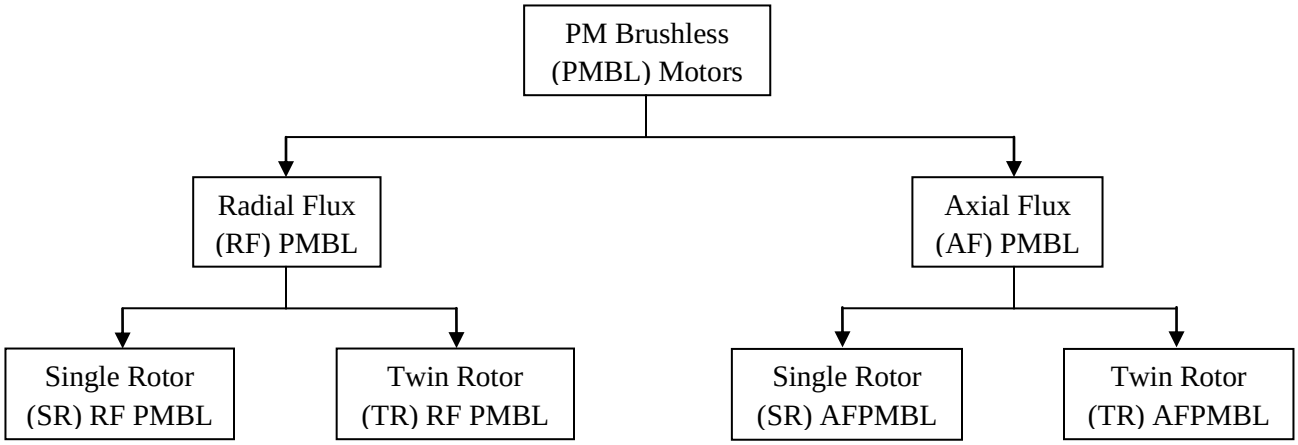

Fig. 1.3. Classification of Permanent Magnet Brushless (PMBL) motors

The current dissertation investigates Permanent Magnet Brushless (PMBL) DC motors for application as in-wheel motors of electric vehicles. Two geometrical variations of PMBL motors of interest are Axial-Flux Twin-Rotor (AFTR) PMBL motor and Radial-Flux Twin-Rotor (RFTR) PMBL motor with slot-less stators. A common and conventional version of the latter type of motor is cylindrical motor with single rotor and a slotted stator. The advantage of a slotless stator is that the motor will not have any cogging torque resulting in lower torque ripple and a better comfort for the rider. The AFTR PMBL motor and conventional cylindrical motor are often proposed as in-wheel motors, whereas the RFTR PMBL motor is still considered as an emerging area. Wheel size and diameter are a few of the governing factors in determining which kind of motor, among the three, suits the application. Another important factor in the design of in-wheel motors is the torque density (torque-to-volume ratio). This factor is also a criterion in choosing a particular PMBL motor for in-wheel drive application, as an electric vehicle demands a compact motor not compromising the value of torque output from the motor.

The dissertation provides an express method that allows comparing different kinds of PMBL motors and selecting a motor design which gives the maximum torque density for

particular wheel dimensions. In other words, it addresses the critical issue of motor selection for the electric vehicle industry.

1.2 Objectives of Dissertation

The following are the objectives of this dissertation:

1. To develop an express method that allows comparison of brushless PM slot-less motors of the same volume with respect to produced electromagnetic torque.
2. To determine and compare the electromechanical parameters of AFTR, RFTR and single-rotor cylindrical PMBL slot-less motors of the same volume, using FEM, in order to check the developed express method.
3. To validate the computational methods used in simulation of the above three PMBL slot-less motors on the basis of results obtained from calculations and measurements carried out for in-wheel brushless PM motor.

1.3 Dissertation Methodology

To achieve the objectives listed in previous section, a literature survey is the first and foremost step to study the work done in this field by other researchers. An in-depth knowledge of electric motors, especially PMBL motors, their design variations and operation as well as optimization is necessary. To develop an express method for comparison, the analytical expressions for AFTR PMBL, RFTR PMBL and single-rotor cylindrical motors with slot-less stators have to be derived and this requires profound experience in electric machine theory. The torque ratio of any two motors is then plotted as a function of wheel diameter. Further, these motors are modeled in Finite Element Modeling software. The 2-dimensional models are created and optimized using FEMM 4.2 [47]. The 3-dimensional models are then created in Maxwell

v13 from Ansoft [48] to perform magnetostatic and parametric analysis. The torque ratios are calculated from the simulation results of the three motors and are compared with the analytical approach. Thus a conclusion can be attained as to which motor makes a better selection for gearless drives of electric vehicles.

The 3-dimensional finite element analysis tests the software expertise pertaining to different solvers like magnetostatic and transient. Because Maxwell v13 is used as a benchmark to validate the analytical approach, it is equally important to validate Maxwell v13. This is achieved by comparing the software results for wheel chair motor (a single-rotor slotted stator cylindrical motor) with the laboratory results.

The prototype for single-rotor slotted stator cylindrical motor is manufactured and tested in the laboratory for wheel chair application. The experimental results from this motor are used to validate the simulation results obtained from Maxwell v13 for this motor, which also validates the software in general. The winding parameters determined from FEM are used with the block diagram of the motor in Simulink. The motor along with the supply circuit is analyzed to observe the dynamic behavior of the wheel chair motor.

1.4 Structure of Dissertation Chapters

The dissertation is structured as follows:

Chapter 2 gives an introduction to PM machines, their principle of operation and the various types of PM motors. The influence of stator structure on motor performance and torque ripple is discussed in detail.

Chapter 3 describes the axial-flux PMBL motor and the torus type disc motor in particular. A literature study is done on the design variations of disc motor and their applications are presented.

Chapter 4 provides the principle of operation of a Radial-Flux PMBL motor. The PMBL cylindrical motor is one of the widely used motors. Their application as in-wheel motors for various types of transportation is discussed.

Chapter 5 presents an extensive work on the existing techniques for comparison of PMBL motors. The proposed method for comparative study is described. The analytic torque expressions, for each of the motors, are derived based on electric and magnetic circuit theory and an express method is developed for comparison of different types of PMBL motors.

Chapter 6 discusses the design data and finite element modeling of disc type twin-rotor PMBL motor with slot-less stator. The torque ripple and average torque of the motor obtained from Maxwell v12 are provided.

Chapter 7 presents the three-dimensional finite element analysis of a cylindrical shape twin-rotor PMBL motor with slot-less stator. Magnetostatic as well as parametric analysis is performed in three-dimensional FEM software and the results are discussed.

Chapter 8 gives the design and modeling of a single-rotor cylindrical motor with slot-less stator. The torque ratios with respect to AFTR and RFTR PMBL motors are computed and compared with the ones from analytical approach developed in this dissertation.

Chapter 9 deals with the modeling and analysis of the conventional single-rotor slotted stator cylindrical PMBL motor for the gearless drive of an electric wheel chair. Experimental results performed on the hardware prototype of this motor are discussed and are used to validate the simulation results obtained from Maxwell and Simulink.

Chapter 10 compares the parameters and performance of AFTR, RFTR and single-rotor cylindrical PMBL motors with slot-less stators. The proposed dissertation method is verified and conclusions are presented, while pointing to the scope of future research.

CHAPTER 2: PM BRUSHLESS MOTORS FOR ELECTRIC VEHICLES

2.1 Introduction

Traditional DC motors rely on field winding to provide field excitation for machines. With the innovation in permanent magnet materials, it was found in early 1950s [24], that permanent magnets can be used as an alternative excitation source to the field windings of DC machines for producing the required air-gap magnetic flux. This led to the development of Permanent Magnet (PM) machines. Since then, the PM machines have gained popularity for many industrial applications, and are also highly suitable for MPVs and EVs. The features of brushless PM machines include, but are not limited to:

- loss-less excitation, or elimination of field circuit copper losses, leading to increase in efficiency
- higher specific torque (torque to mass ratio) and/or output power per volume when compared to machines excited by field windings
- higher magnetic flux density in air gap leading to better dynamic performance in smaller machines
- low maintenance requirements
- compactness of the motor owing to simple construction
- smaller PMDC motors with low power ratings are not only cost-effective, but also produce less noise and low electromagnetic interference
- very high speeds, up to 50,000rpm can be obtained [4]

All the above factors indicate why a PM motor is a strong competitor for EV applications. A permanent magnet can be best described by its hysteresis loop or the B-H curve, as shown in Fig.

2.1, and is usually wider than that of a ferromagnetic material. The second quadrant of B-H plot refers to the demagnetization curve of a PM. It gives information such as remanence or residual flux B_r which is defined as the magnetic flux density corresponding to zero magnetic field intensity, and coercive field strength H_c which is a measure of reverse magnetic field needed to drive the magnetization to zero after being saturated. The magnetic properties of PM stay intact as long as the operating point lies on the linear region of B-H characteristic. Ideally, the rotors and stators of machines are manufactured from ferromagnetic materials with small values of B_r and H_c to ensure low hysteresis losses. The poles of PM motors should have large value of B_r in order to have large flux in the machine and large value of H_c so that very large current is required to demagnetize the poles [4].

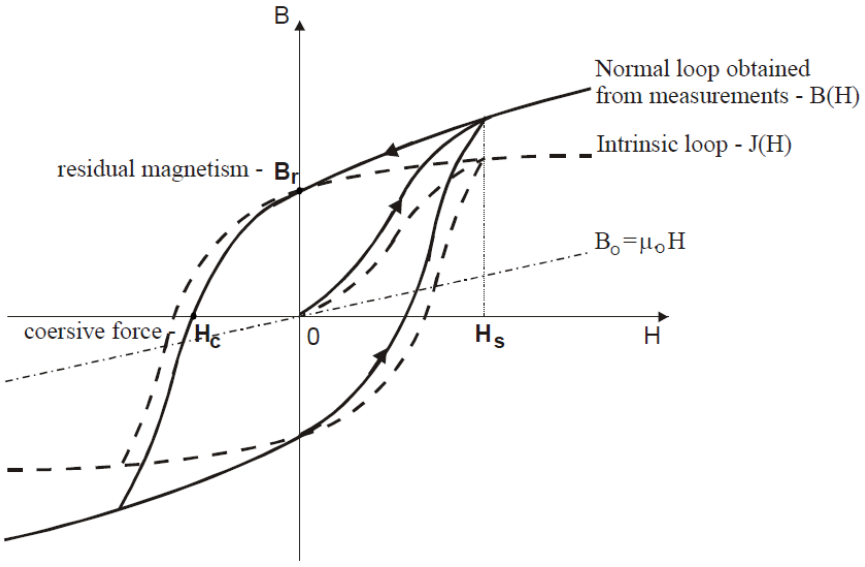

Fig. 2.1. B-H characteristic for a typical ferromagnetic material [3]

Different types of PMs used in DC motors are Alnico, ferrites or ceramics and rare-earth magnets like samarium cobalt (SmCo) and neodymium-iron-boron (NdFeB). Alnico magnets have very high flux density but low coercive force. Though ferrites have high coercive force, low

core losses and are cheap, they have low flux density. Rare-earth magnets are known for both high flux density and high coercive force, but are cost-prohibitive due to the expensive metals and manufacturing complexity. Bonded NdFeB magnets, unlike sintered NdFeB magnets, can be produced at lower cost at the expense of lower flux density.

The magnetic properties of PMs are temperature dependent. Overloading causes heating of the machine which may result in demagnetization of poles. Hence, care should be exercised in the selection of PMs for the poles. As an example, Fig. 2.2 shows the sensitivity of a PM from VacuumSchmelze, VACOMAX 240 HR, to temperature. Armature mmf resulting from excessive armature current might also contribute to demagnetization of the PMs and happens when a PM machine is improperly designed or by short-circuited current which is a few times the rated armature current. Thus, the choice of PM material depends on the operating temperature of machine, and is an important factor in the design of a motor.

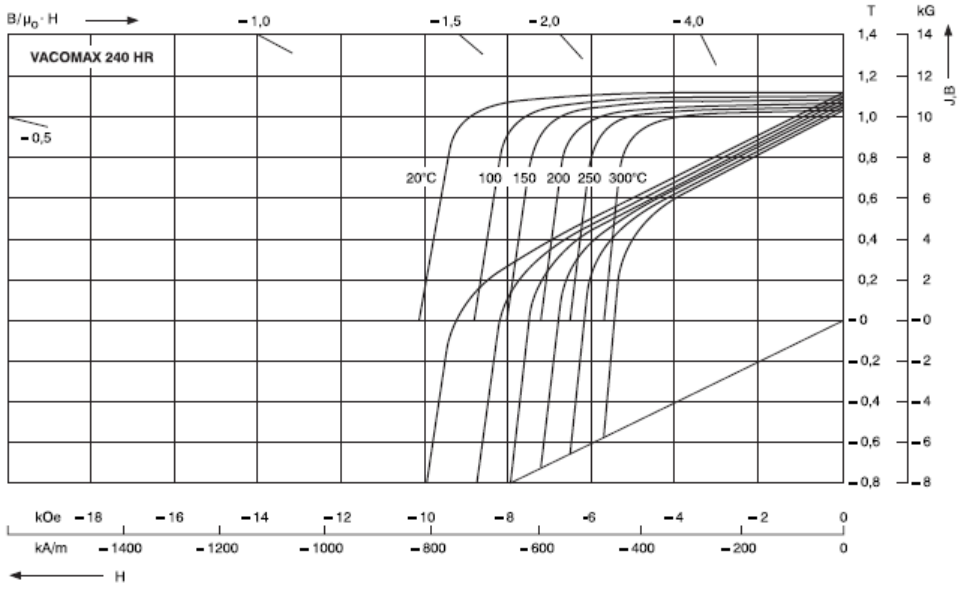

Fig. 2.2. Demagnetization curve for VACOMAX 240 HR, courtesy of VacuumSchmelze [5]

Since the flux of a permanent magnet is fixed, the speed of a PM brushed DC (PMBDC) motor cannot be controlled by varying the flux or field current. The speed control of a PM brushed DC motor can only be achieved by varying armature voltage or armature resistance. In case of PM brushless (PMBL) motors, the speed can be controlled also by changing supply frequency.

2.2 Principle of Operation

A brushless PMDC motor is a multi-phase PM motor supplied from multi-phase inverter operating as an electronic commutator. As an example, a three phase brushless PMDC motor is shown in Fig. 2.3.

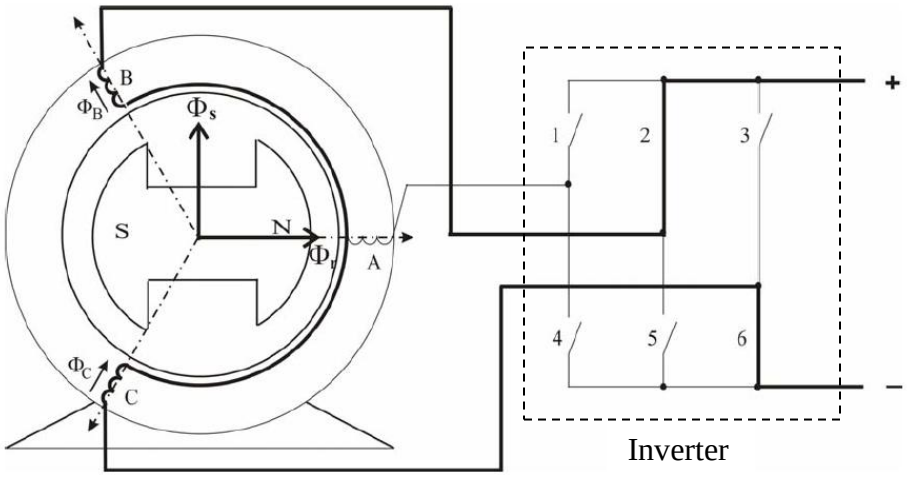

Fig. 2.3. Illustration of the principle of operation of a brushless PMDC motor

A three phase winding is placed in the stator and the rotor is equipped with permanent magnets. The armature windings are either surface wound on stator or located in the stator slots. The rotor angular position is sensed and fed back, so that the armature current is switched among the motor phases in synchronism with rotor motion. This is called as electronic commutation or self-controlled synchronization, and forms the basic principle of operation of a brushless PMDC

motor. The electronic inverter and position sensors of a brushless PMDC motor are analogous to mechanical commutator of a brushed PMDC motor. Thus, a brushless PMDC motor drive is composed of: (i) Permanent magnet rotor, (ii) Stator with the armature winding, (iii) Rotor position sensor and (iv) Electronic circuit to switch the phase currents [4].

In case of inverter shown in Fig. 2.3, for the phases connected in Y, only two of the three stator coils of the brushless PMDC motor are energized with a constant dc voltage at any point of time. This results in a stator magnetic field B_s, as shown in Fig. 2.3. The torque is produced because of interaction between rotor field B_r and stator field B_s and it rotates the rotor. As the rotor rotates, the particular phase windings are energized (due to control circuit responding to the signal from a rotor position sensor) so that the stator flux Φ_s produced by the stator winding is always perpendicular to the rotor flux Φ_r, similar as it takes place in brush PMDC motors (see Fig. 2.3). Thus the motor rotates continuously with the electronic commutation of phase currents. Referring to Fig. 2.3, commutation takes place in the sequence (1, 5), (1, 6), (2, 6), (2, 4), (3, 4) and (3, 5) turning the appropriate phase currents on and off. For a three phase motor supplied from a six-step power source, each stator coil remains energized until the rotor rotates for 60 electrical degrees, and this process is repeated six times during an electrical revolution. If B_R is the rotor magnetic field due to permanent magnets and k is the proportionality constant, the torque of a brushless PMDC motor is given by:

$$T = kB_R \times B_s \tag{2.1}$$

Hall sensors or optical sensors are usually employed to detect the rotor position of a brushless PMDC motor, and constitute an important component of control circuit. To prevent the interference of stator magnetic field with the operation of Hall sensors, the latter elements should

be placed far enough from stator winding. Hall sensors are highly accurate in position sensing, have long life and less radio frequency interference besides being suitable for different operating conditions [9].

The speed and direction of rotation of the motor can be controlled by the control circuit. The ease and simplicity of control made the brushless PMDC motors increasingly popular. A three-phase machine needs only six discrete rotor positions per electrical revolution to synchronize the rotor position with stator magnetic flux and produce the torque. This is achieved by mounting three hall sensors displaced in space by 120 degrees.

It should be noted that the induced back-emf in a brushless PMDC motor is trapezoidal in shape. The ideal phase currents and induced back-emf waveforms of a brushless PMDC motor are shown in Fig 2.4. The square-wave phase currents are supplied such that they are synchronized with the back-emf peak of the respective phase. The controller performs this task by using the rotor position feedback information (see Fig. 2.5(a)) [10].

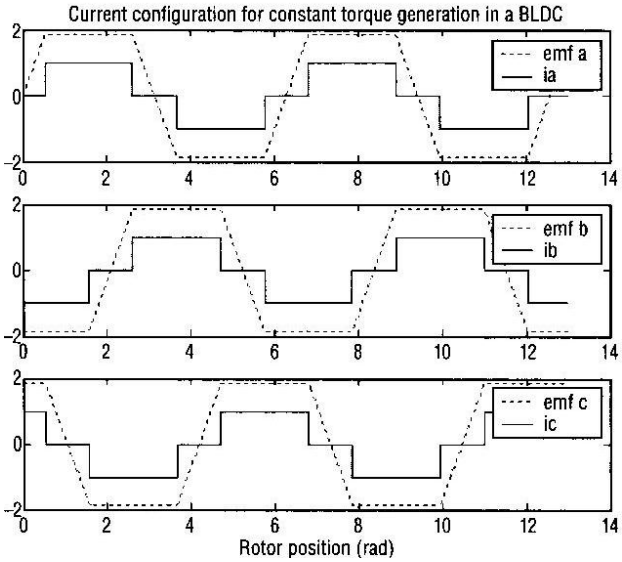

Fig 2.4. Ideal back-emf and phase currents of a three-phase brushless PMDC motor[10]

2.3 Classification of PM Brushless DC Motors

The permanent magnet motors can be grouped based on the construction of motor. A Permanent Magnet Synchronous Motor (PMSM) is similar to a brushless PMDC motor in construction. The PMSM does not need a position sensor; instead a reference frequency can be used by the controller to switch current among the three phases (see Fig. 2.5 (b)). The rotor rotates synchronously with the stator magnetic flux whose speed, ω_s is related to the supply frequency, f and number of poles, p as follows:

$$\omega_s = \frac{2\pi f}{p/_2} \tag{2.1}$$

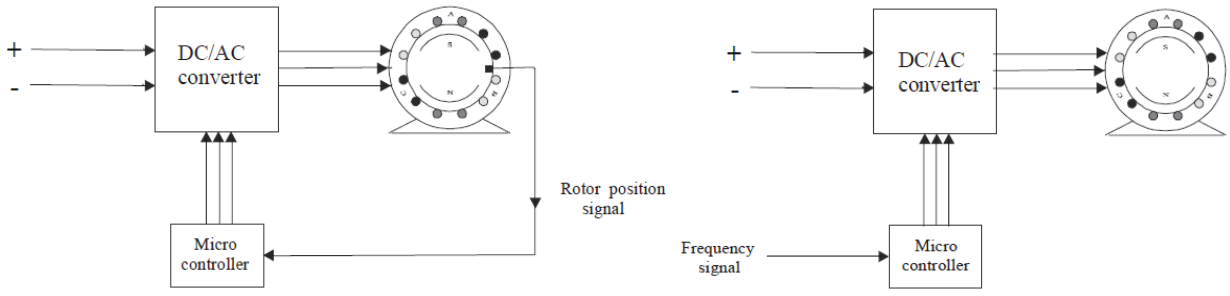

(a) **(b)**

Fig. 2.5. Control circuit for a: (a) brushless PMDC motor, (b) PM Synchronous motor [3]

The differences between a PMBLDC, PMBDC motors and PMSM are discussed in detail in [23]. Two major groups of PMBLDC motors can be identified according to the direction of magnet flux. Various constructions of the radial-flux (cylindrical shape) and axial-flux (disc type) motors are specified below [8]:

- Cylindrical type:

- Stator structure
    - Conventional slotted stators with teeth
    - Slot-less (surface wound) stators
    - Salient pole stators
- Rotor structure
    - Merrill's rotor (or the classical structure)
    - Interior magnet
    - Surface magnet
    - Inset magnet
    - Rotor with buried magnets symmetrically distributed
    - Rotor with buried magnets asymmetrically distributed
- Single-sided (conventional motor)
- Double-sided

- Disc type:
    - Stator structure
        - Motors with slotted stators
        - Motors with slot-less stators
    - Single-sided
        - Armature winding with distributed coils
        - Armature winding with concentrated coils
    - Double-sided
        - With internal rotor
        - With internal stator (torus motor)

The conventional permanent magnet motors are single-sided with cylindrical stator and a rotor. Brushless PM motors with twin-rotors (also called double sided) are a recent development and have two air-gaps resulting in higher torque output than a single-sided motor. Further, the slotless versions of PM motors have low torque ripple and no cogging torque when compared to their slotted counterparts. The construction of different types of permanent magnet motors is discussed in detail in [8] pp. 171-172. A few of the rotor constructions, distinguished by the position of permanent magnets, are shown in Fig. 2.6.

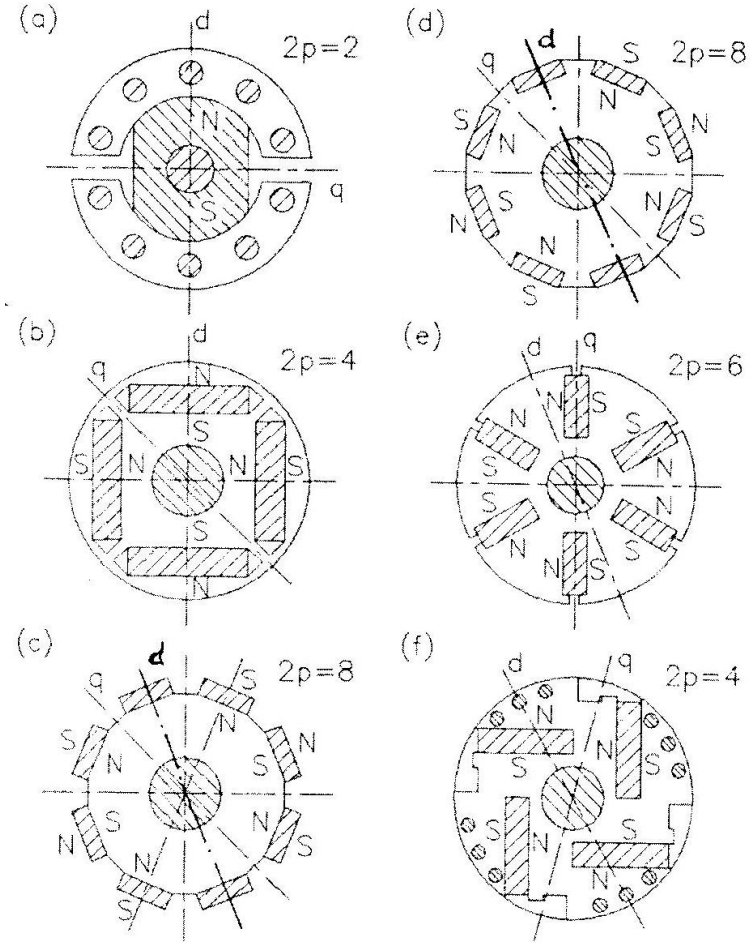

Fig. 2.6. Various rotor constructions of a PM motor: (a) Classical structure, (b) Interior PM rotor, (c) Surface magnet rotor, (d) Inset magnet rotor, (e),(f) Buried magnet rotors [8]

The interior magnet rotor has magnets located safe from the centrifugal forces and hence is recommended for high frequency high speed motors. The interior magnet and inset magnet rotors have PMs magnetized in radial direction whereas the PMs of a surface magnet rotor can be magnetized radially or circumferentially. However, the emf induced by PMs of an inset type rotor is lower than that of a surface magnet rotor. The PMs of a buried magnet rotor are magnetized circumferentially and are protected from armature fields unlike those of a surface magnet rotor. But, this is achieved by a trade-off with construction complexity: the former having a complicated one than the latter.

The inset PM rotor is not often met in literature. The advantage of inset PM rotor is that a large flux path exists in the rotor iron reducing its saturation. For sensorless control of a low-speed PMSM, this means that the rotor angle can be detected even at high currents [11]. Also, the initial rotor position can be precisely estimated because of high PM flux. When compared to a surface magnet rotor, the inset PM rotor provides higher peak torque per unit current for a high-speed PMSM [12]. These two types of rotor configurations are compared for a brushless PMDC motor in [12] and it was concluded that both types of rotors have similar torque capabilities due to averaging the torque over a 60 degree interval in the brushless PMDC motor unlike a PMSM in which the torque can be obtained at any point of the torque-angle curve.

The objects of this dissertation are conventional single-rotor cylindrical PMBL motors with slot-less and slotted stators, an axial-flux PMBL motor and a radial-flux PMBL motor, both with twin-rotor slot-less internal stator. Surface-mounted magnet rotors are chosen for all the four motors of interest.

2.4 Mathematical Model of Three-phase PM Motor

The mathematical model of PM motor is discussed in this subsection.

To analyze the performance of the motor, a circuit model for the PM motor along with the supply and inverter is used which is shown in Fig. 2.7. To apply this model, the following assumptions are made with respect to a three-phase PM motor:

- Motor magnetic circuit as well as electric circuit are linear
- The three-phase winding is connected in star
- Voltage drop across electronic elements as well as power losses in them are ignored
- Core losses are not considered

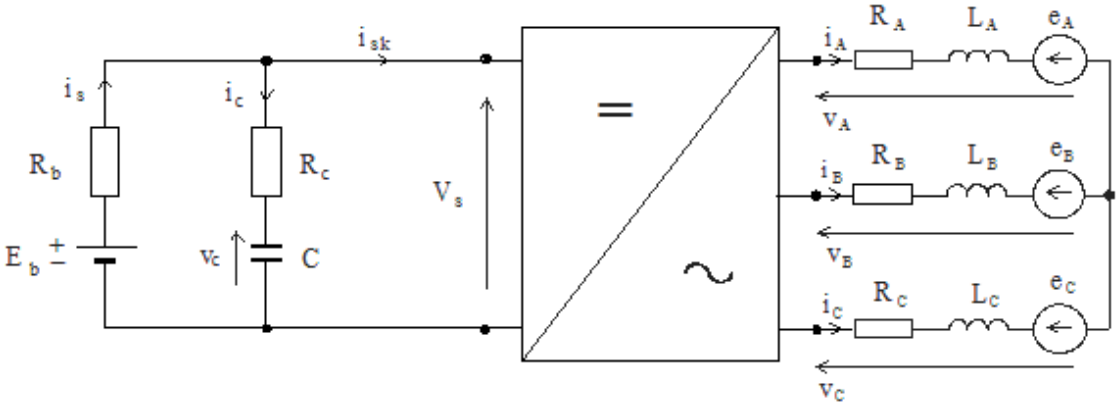

Fig. 2.7. Circuit model of supply + inverter + three-phase PM motor

The voltage equation that describes such a three-phase PM motor is as follows:

$$\begin{bmatrix} v_A \\ v_B \\ v_C \end{bmatrix} = \begin{bmatrix} R_A & 0 & 0 \\ 0 & R_B & 0 \\ 0 & 0 & R_C \end{bmatrix} \begin{bmatrix} i_A \\ i_B \\ i_C \end{bmatrix} + \begin{bmatrix} L_{AA} & L_{AB} & L_{AC} \\ L_{BA} & L_{BB} & L_{BC} \\ L_{CA} & L_{CB} & L_{CC} \end{bmatrix} p \begin{bmatrix} i_A \\ i_B \\ i_C \end{bmatrix} + \begin{bmatrix} e_A \\ e_B \\ e_C \end{bmatrix} \tag{2.2}$$

where v_A, v_B, v_C are the phase voltages

i_A, i_B, i_C are the phase currents

e_A, e_B, e_C are the phase back-emfs

R_A, R_B, R_C are the phase resistances

L_{AA}, L_{BB}, L_{CC} are the phase self-inductances

L_{AB}, L_{AC}, L_{BA}, L_{BC}, L_{CA}, L_{CB} are the mutual inductances between two phases

p is the operator d/dt

For identical phase parameters (assuming symmetrical winding and nonsalient rotor magnetic poles that do not affect the rotor reluctance with rotor angle):

$$R_A = R_B = R_C = R$$

$$L_{AA} = L_{BB} = L_{CC} = L$$

$$L_{AB} = L_{Ac} = L_{BA} = L_{BC} = L_{CA} = L_{CB} = M$$

Since the winding is connected in Y (without neutral wire), the stator phase currents are related as: $i_A + i_B + i_C = 0$, the equation (2.2) can now be transformed to the following form:

$$\begin{bmatrix} v_A \\ v_B \\ v_C \end{bmatrix} = R \cdot \begin{bmatrix} i_A \\ i_B \\ i_C \end{bmatrix} + (L - M) \cdot \begin{bmatrix} 1 & 0 & 0 \\ 0 & 1 & 0 \\ 0 & 0 & 1 \end{bmatrix} \cdot p \begin{bmatrix} i_A \\ i_B \\ i_C \end{bmatrix} + \begin{bmatrix} e_A \\ e_B \\ e_C \end{bmatrix} \tag{2.3}$$

After rearranging:

$$p \begin{bmatrix} i_A \\ i_B \\ i_C \end{bmatrix} = \frac{1}{L-M} \left(\begin{bmatrix} v_A \\ v_B \\ v_C \end{bmatrix} - R \cdot \begin{bmatrix} i_A \\ i_B \\ i_C \end{bmatrix} - \begin{bmatrix} e_A \\ e_B \\ e_C \end{bmatrix} \right) \tag{2.4}$$

Applying Laplace transform to the voltage equation we obtain:

$$(R + L_s s) \begin{bmatrix} i_A \\ i_B \\ i_C \end{bmatrix} = \begin{bmatrix} v_A \\ v_B \\ v_C \end{bmatrix} - \begin{bmatrix} e_A \\ e_B \\ e_C \end{bmatrix} \tag{2.5}$$

where synchronous inductance, $L_s = L - M$

The electromagnetic torque, T_{em} is a function of flux linkage, $\lambda(\theta)$ and current in the stator phase winding, i_{ph}. It can be expressed as:

$$T_{em} = \lambda(\theta) \cdot i_{ph} = K_T \cdot i_{ph} \tag{2.6}$$

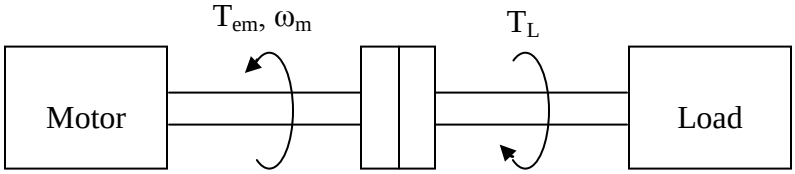

Fig. 2.8. Electromechanical system with the motor, load and coupling

For the mechanical system consisting of motor and the load, as shown in Fig. 2.8, with an equivalent moment of inertia, J and friction coefficient, D, the equation of motion is described in terms of electromagnetic torque, T_{em} and load torque, T_L as:

$$T_{em} - T_L = J \cdot \frac{d\omega_m}{dt} + D \cdot \omega_m \tag{2.7}$$

Laplace transform on the above equation yields

$$T_{em} - T_L = J \cdot s \cdot \omega_m(s) + D \cdot \omega_m(s) \tag{2.8}$$

Rearranging,

$$\omega_m(s) = \frac{T - T_L}{Js + D} \tag{2.9}$$

The voltage equation for the supply is given as:

$$E_b - i_s \cdot R_b - i_c \cdot R_c = 0 \tag{2.10}$$

$$v_s = v_c + i_c \cdot R_c \tag{2.11}$$

$$i_s = i_{sk} + i_c \tag{2.12}$$

where E_b and R_b are voltage and resistance of the source; R_c is the capacitor resistance; i_s is source circuit current; i_{sk} is converter input current; v_c is voltage across capacitor given by

$$v_c = \frac{Q_c}{C} \tag{2.13}$$

Q_c is charge in capacitor, C is capacitance and i_c is current flowing through the capacitor:

$$i_c = \frac{dQ_c}{dt} \tag{2.14}$$

The equation that links the supply and motor sides results from the equality of the powers at input and output of the converter

$$i_{sk} = \frac{1}{v_s}(i_A v_{sA} + i_B v_{sB} + i_C v_{sC}) \tag{2.15}$$

where supply voltages for the phases (v_{sA}, v_{sB} and v_{sC}) results from the operation of converter.

The magnetic flux due to the PMs on rotor induces a back-emf, e_{ph} in the stator windings given by:

$$e_{ph} = \omega_m \cdot \lambda(\theta) = K_E \cdot \omega_m \tag{2.16}$$

where ω_m is the speed of rotor and λ is the flux linkage which is dependent on the rotor position. K_E is the back-emf constant and K_T is the torque constant. Ideally,

$$K_E = K_T \tag{2.17}$$

From (2.6) and (2.16), the electromotive force in (2.16) can be re-written as:

$$e_{ph} = \omega_m \cdot \frac{T}{i_{ph}} \tag{2.18}$$

For the three-phase winding,

$$e_A = K_E \cdot f_a(\theta_e) \cdot \omega_m \tag{2.19}$$

$$e_B = K_E \cdot f_b(\theta_e) \cdot \omega_m \tag{2.20}$$

$$e_C = K_E \cdot f_C(\theta_e) \cdot \omega_m \tag{2.21}$$

where $f_a(\theta_e) = \sin(\theta_e)$, $f_b(\theta_e) = \sin\left(\theta_e - \frac{2\pi}{3}\right)$, $f_c(\theta_e) = \sin\left(\theta_e - \frac{4\pi}{3}\right)$ (2.22)

and θ_e is the electrical angle.

The electrical power transferred to rotor, P_e is equal to mechanical power, P_m at the shaft.

$$P_e = P_m \tag{2.23}$$

where $P_e = e_A i_A + e_B i_B + e_C i_C$ (2.24)

and $P_m = T_{em}\omega_m$ (2.25)

The total electromagnetic torque of a three-phase PM motor is then,

$$T_{em} = \frac{e_A i_A}{\omega_m} + \frac{e_B i_B}{\omega_m} + \frac{e_C i_C}{\omega_m} = K_E(f_a(\theta_e) \cdot i_A + f_b(\theta_e) \cdot i_B + f_c(\theta_e) \cdot i_C) \tag{2.26}$$

Combining all the above equations, the system can be expressed in state-space form as

$$\dot{x} = Ax + Bu \tag{2.27}$$

$$x = \begin{bmatrix} i_A & i_B & i_C & \omega_r & \theta_e \end{bmatrix}^t \tag{2.28}$$

$$A=\begin{bmatrix} -\frac{R_s}{L_s} & 0 & 0 & -\frac{K_E(f_a(\theta_e))}{L_s} & 0 \\ 0 & -\frac{R_s}{L_s} & 0 & -\frac{K_E(f_b(\theta_e))}{L_s} & 0 \\ 0 & 0 & -\frac{R_s}{L_s} & -\frac{K_E(f_c(\theta_e))}{L_s} & 0 \\ \frac{K_E(f_a(\theta_e))}{J} & \frac{K_E(f_b(\theta_e))}{J} & \frac{K_E(f_c(\theta_e))}{J} & -\frac{D}{J} & 0 \\ 0 & 0 & 0 & \frac{p}{2} & 0 \end{bmatrix} \tag{2.29}$$

where p is the number of poles.

$$u=\begin{bmatrix} v_A & v_B & v_C & T_L \end{bmatrix}^t \tag{2.30}$$

$$B=\begin{bmatrix} \frac{1}{L_s} & 0 & 0 & 0 \\ 0 & \frac{1}{L_s} & 0 & 0 \\ 0 & 0 & \frac{1}{L_s} & 0 \\ 0 & 0 & 0 & -\frac{1}{J} \\ 0 & 0 & 0 & 0 \end{bmatrix} \tag{2.31}$$

A PMSM is supplied by a three-phase sinusoidal voltage whereas a brushless PMDC motor operates with square-wave phase voltages. However, both the motors differ in their control circuits as discussed earlier, with the brushless PMDC motor having simple requirements than a PMSM.

The mathematical equations stated in this section are used to build the block diagram of a three-phase brushless PMDC motor in Simulink in the subsequent chapters. The supply circuit is modeled to observe the dynamics of motor drive. The above model can be extended to any

number of phases of a brushless PMDC motor assuming no iron and stray losses and that there are no currents induced in rotor due to stator harmonic fields.

2.5 Torque Ripple and Its Minimization

Despite many advantages of a brushless PMDC motor, it suffers from an inherent drawback of ripple in the electromagnetic torque developed. Some of the factors giving rise to torque ripple are cogging torque (due to stator teeth), harmonics in armature current and back-emf. The torque ripple is more evident in case of low-speed motors. Smooth operation is an important criterion for MPV and electric vehicle applications. This demand addresses the necessity for minimizing the torque ripple and improving the quality of torque output.

Many definitions of torque ripple are often met in literature [8]. One of them is defined as follows:

$$T_r = \frac{T_{max} - T_{min}}{T_{av}} \tag{2.32}$$

where T_{max} is the maximum torque and T_{min} is the minimum torque over 60 degrees electrical angle assuming ideal commutation. T_{av} is the average torque computed as:

$$T_{av} = \frac{3}{\pi} \int_{\theta_1}^{\theta_1 + \frac{\pi}{3}} T(\theta) d\theta \tag{2.33}$$

Another definition is formulated as:

$$T_r = \frac{T_{max} - T_{min}}{T_{max} + T_{min}} \tag{2.34}$$

The next definition relates the maximum and minimum torque to the rms value:

$$T_r = \frac{T_{max} - T_{min}}{T_{rms}} \tag{2.35}$$

T_{rms} is the rms torque computed as:

$$T_{rms} = \sqrt{\frac{1}{T_p}\int_0^{T_p} T^2(\theta) d\theta} \tag{2.36}$$

where T_p is the period of torque waveform.

According to the research carried out in [13], the torque ripple can be divided into four components:

(i) Pulsating torque, due to interaction between stator and rotor magnetic fields rotating with different speeds but having the same number of poles

(ii) Fluctuating torque, due to current fluctuations arising from bounded switching time intervals

(iii) Cogging torque, owing to non-uniform magnetic field distribution between stator teeth and rotor permanent magnets

(iv) Inertia and mechanical system torque (external source of ripple), due to dynamic motion of mechanical components of the motor

The inertia and mechanical system torque is lower in low speed systems. But, at low speed, the fluctuating torque can be higher due to larger current fluctuations arising from bounded switching times and higher source voltage. In other words, perfect square wave currents cannot be obtained as the current commutation between phases is not instantaneous in practice. This causes deviation of the waveform from its ideal shape and appears as ripple in the torque output. Under various loads, if either the armature currents or dc link current are adjusted instead of varying the back-emfs, the ripple due to fluctuating torque can be reduced.

The pulsating torque is absent in a PMSM due to spatially sinusoidal air gap flux distribution and sinusoidal armature currents in time. However, it is inherently present in brushless PMDC motor because of its trapezoidal back-emfs and square wave currents. Studies show that the ripple due to pulsating torque can be reduced by producing fluctuating counter torque [13].

2.5.1 Torque Ripple Reduction by Motor Design Modification

Cogging torque is a predominant component of the torque ripple, caused by the interaction of stator teeth with permanent magnets on the rotor. It can be approximated as follows:

$$T_c(\theta) = -\frac{\partial E_g(\theta)}{\partial \theta} \tag{2.37}$$

where $E_g(\theta)$ is the magnetic energy stored in the air gap of motor and θ is the relative position of PM with respect to iron core.

Besides contributing to torque ripple, cogging torque also produces noise and vibration. It is detrimental to the performance of the system particularly at low speeds. This torque can be reduced either by skewing the rotor magnets or the stator slots. Due to manufacturing convenience, skewing the stator slots is often preferred. However, skewing results in increased leakage inductances and stray losses lowering the torque output, especially in motors with a small number of teeth per pole. According to [19], not only the torque ripple but also the average torque output reduced with increased skew angle from half-slot to full-slot. Traditionally, the magnets are skewed by one full slot. Underskew or overskew results in a stronger torque ripple. But, skewing by one full slot can make the waveform more sinusoidal than trapezoidal

increasing the torque ripple [18]. Thus determining an optimal skew angle is an important criteria in minimizing the torque ripple.

Other technique to reduce cogging torque is by appropriate selection of magnet width to slot pitch ratio. It was shown by Li [14], that the cogging torque for a surface mounted PM motor can be minimized by choosing a magnet width which is somewhat greater than an integral number of slot pitches. It can be further reduced by rotating one pair of poles relative to the other pair in a four pole motor and also by bifurcating the stator teeth.

Another way to lower the torque ripple and improve torque linearity is by reducing the electrical loading [15]. With higher stator ampere-turns, the air gap magnetic field is distorted due to increase armature reaction. The electrical loading can be decreased by substituting the number of turns with increased stack length. But, this is not an economical design approach considering the high cost of permanent magnets.

While magnet pole shaping and magnet edge shaping are design techniques to reduce the torque ripple without sacrificing the peak output torque, reduction of magnet arc length is another method for torque ripple minimization but with compromising the maximum output torque value to some extent [16].

It should be noted that the motors being compared in the Express Comparative Method in this dissertation have slot-less stators. This means that the cogging torque is absent and does not contribute to torque ripple of these motors. Also, the small power slot-less motors have higher efficiency for high speed ranges not to mention low acoustic noise [8]. However, they need more PM material than an equivalent slotted motor to maintain the torque density. The conventional single-rotor cylindrical motor for electric wheel chair application has a slotted stator and the

method employed in this dissertation to lower the torque ripple of this motor is by skewing the stator teeth.

2.5.2 Torque Ripple Reduction by Power Electronics Modification

One of the significant sources of torque ripple is the commutation of phase currents. When the three-phase PM motor operates as a brushless DC motor, position sensors are employed to detect the rotor position and then the phase currents are switched accordingly. This is a simple approach but an alternative method is based on direct current sensing which allows elimination of torque ripple due to commutation especially at low speed ranges [20]. In this method, current sensors are placed in the DC link at inverter input and the current amplitude is controlled by PWM or by hysteresis. In a research carried out by Liu [21], the commutation torque ripple minimization is achieved by controlling the torque directly rather than controlling the current as in the case of a current shaping PWM technique which increased the complexity of system. The torque error is minimized between the reference torque and estimated torque, and the phase current waveform is adaptively adjusted to maintain the constant electromagnetic torque output.

Harmonics in phase currents is another factor that causes ripple in torque output. An experimental testing is carried out in [17] to reduce the torque ripple of a brushless PMDC motor used an in-wheel motor for electric bicycle. This method is based on the analytical computation of current harmonics to cancel the torque harmonics. The experimental analysis shows that the vibration behavior of the motor is improved by supplying it with optimal currents.

Other approaches to reduce torque ripple that are found in literature are: shaping the back emf to better match the drive signal; doubling the number of hall sensors, without changing the

number of poles, to double the number of commutation cycles; and by applying more than three phases to the stator. The torque ripple of a six-phase brushless PMDC motor is reduced by 50% when compared to a three-phase motor operating with the same phase currents and rotor speed [22]. Misalignment of hall sensors with respect to the back-emf might also be a cause for torque ripple [18]. Hence, proper care should be exercised in assembling the motor drive.

2.6 PM Motor Applications

The permanent magnet motors provide a cost-effective and compact alternative to wound-field motors in applications demanding smaller fractional horsepower size motors. Besides, they also provide better torque and dynamic performance at this size while saving the space of a separate field circuit. The brushless PM motors, in particular, need less maintenance and are relatively lighter than their brushed competitors enabling them to attain much higher speeds [9]. Thus, the brushless PM motors are more commonly used in various domestic and industrial appliances as well as in automotive sector.

Industrial applications that demand variable speed motors, for example, cooling fans, compressors, blowers, conveyor belts employ PMDC motors due to their ease of speed control. Some of the domestic applications of these motors include air conditioners/heaters, refrigerators, microwave ovens, blenders, laundry machines, vacuum cleaners, toys, etc. They can also be found in power tools like drills, screwdrivers, grinders and chain-saws [8]. Large and small-scale businesses make use of these motors in computer hard disk drives, CD players, photocopiers, printers and scanners. The low maintenance factor makes PMBL DC motors ideal for biomedical applications like artificial heart, Positive Airway Pressure (PAP) respirators, medical analyzers, electric wheelchairs, etc. Further the rotor position can be sensed by monitoring the motor back-

emf. In other words, a sensorless PMBL DC motor drive can be created by eliminating the hall sensors and making these motors more cost competent in the medical market.

The PMBL motors are used in sophisticated equipment like robots. They can operate in low pressures because of little brush wear, for example, in aircrafts, space shuttles and satellites flying at high altitudes. High reliability, low electromagnetic interference and precise speed control make PMBL motors strong contenders for propulsion systems like missiles, torpedos and submarines. As discussed in the previous chapter, these motors have an edge over the induction, switched reluctance and brushed PM motors for electric vehicles. An electric vehicle powered by PMBL motor has 15% longer driving range than the one with an induction motor [8]. Transportation systems like hybrid vehicles, electric vehicles, elevators, escalators, trams, electric boats and ships make use of PMBL motors. A few examples of electric vehicles are electric cars in airports for passenger transportation, golf carts, military vehicles, forklifts in industries, lawn mowers, etc. Besides propulsion, miniature versions of these motors can also aid in automotive applications like power steering, windshield wipers, power seats, power locks, power windows, traction control and alternator/starter.

Earlier, in-wheel motors were employed in high power army vehicles. The current dissertation investigates PMBL DC motors as a propulsion source and employs a conventional cylindrical PMBL DC motor prototype as an in-wheel motor of electric wheel chair. Two twin-rotor axial flux and radial flux slot-less PMBL DC motors are modeled for electric vehicle applications. An express method developed in this dissertation compares the three motors with respect to their torque capabilities as in-wheel motors for the automobile industry.

CHAPTER 3: AXIAL FLUX PM MOTORS

3.1 Introduction

The earliest electrical machine developed was an axial flux machine by M. Faraday in 1831 [25]. Axial flux machine can be classified as a PMBL machine with the permanent magnet flux direction parallel to the motor shaft. The Axial Flux (AF) PM motors are known for their compact construction, high power density and acceleration making them more suitable for high performance applications. Their principle of operation is the same as that of a PMBL DC motor discussed in Chapter 2.

The AF PMBL motor, seen in Fig. 3.1, has rotor in the shape of a disc. The permanent magnets are glued with epoxy on the rotor surface (surface-mounted), or buried in the rotor disc (buried-magnet). Alternatively this motor can also be called as disc-type motor or pancake motor due to its shape. The rotor faces the stator with armature winding. The winding can be either placed in stator slots or placed between stator yoke and rotor disc in case of a coreless stator. Non-magnetic, non-conducting material, like stainless steel or carbon fiber sleeves [10], is used to support the stator coils and rotor permanent magnets.

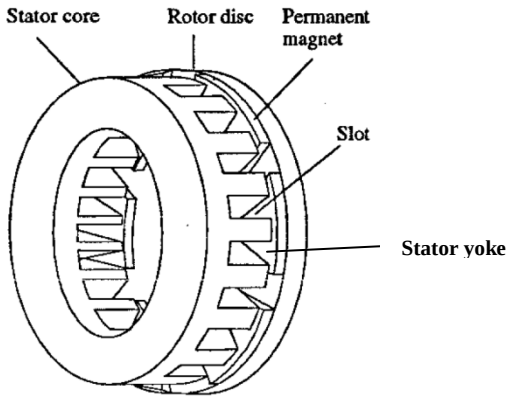

Fig. 3.1. Structure of an AFPM motor [26]

Since the dimensions of AFPM machine change with the radius, precise analysis of such a motor requires 3D finite element modeling. But, 2D modeling can be made possible by unfolding a cross-section of the motor taken at the mean radius of magnets [8], and this yields sufficiently accurate results (although some errors might be induced because of the fact that the pole pitch is different at different radius of the disc).

The torque output of an AFPM machine is proportional to the cube of the diameter. Thus, the torque can be improved by increasing the motor diameter. However, the advantages disappear at very large diameters and it is difficult to have mechanical integrity between the disc and shaft. An alternative solution for increase torque output is by forming multi-stage disc motor, or by having multiple air-gaps.

3.2 Types of AFPM BLDC Motors

The simplest AF machine met in literature is the PMDC motor with disc type rotor, and can be considered as a primitive design, as seen in Fig. 3.2.

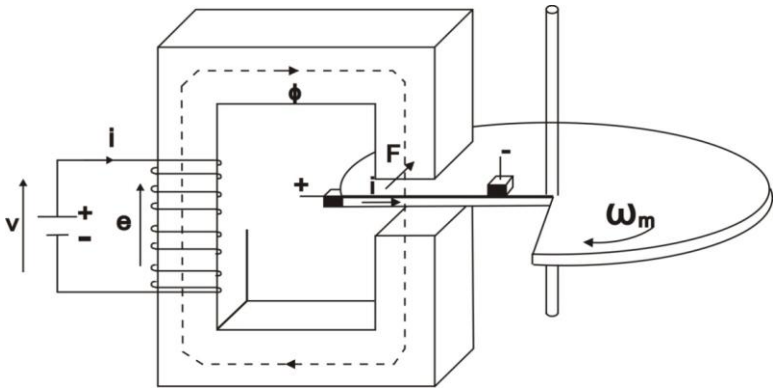

Fig. 3.2. Idea of Faraday's design of AFPM motor

Further classification of AFPM motors can be made based on their construction, as shown in Fig. 3.3.

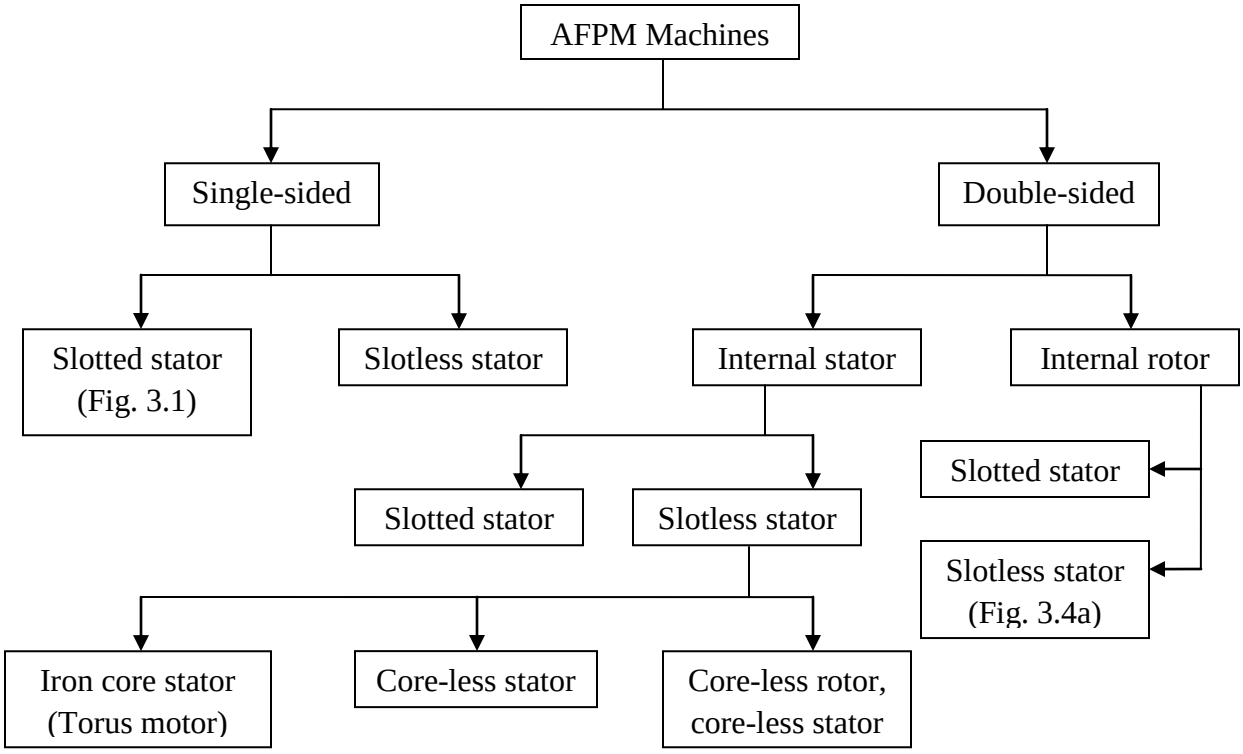

Fig. 3.3. Classification of AFPM motors

The double-sided motors produce higher torque than a single-sided AFPM motor of the same volume. In general, the multi-disc AF PM machines (see Fig. 3.5) require lower volume of iron and have limited iron losses contributed by the harmonic components of armature MMF. On the other hand, AFPM motors with slot-less stators have larger air-gap than a slotted machine. Thus the former kind needs heavier and thicker magnets to produce the required magnetic flux density than the latter ones. For a slot-less machine, the rotor is equipped with surface mounted magnets (to accommodate larger airgap) in most cases and a slotted machine can have either surface mounted or buried magnet rotors. Also, the wires of winding coil interfere with the main air gap flux resulting in eddy currents in the copper. However, it can be emphasized that the slot-less motors have lower torque ripple than a slotted motor due to the absence of cogging torque.

Machines with core-less stators have printed circuit stator windings or film coil windings while those with iron-less rotors have PMs arranged in Halbach array [25]. The core-less AFPM machines are free of iron losses but have lower synchronous reactances while the iron core machines have iron losses yet higher synchronous reactances. While weighing relatively light, the core-less machines can yield higher efficiency due to elimination of core losses, but need more PM material due to larger airgap than an iron core machine. Also, due to absence of magnetic saturation, a core-less machine has a linear torque-current characteristic and an improved low speed control. The peak torque of core-less AFPM machine can be up to ten times the rated torque [25]. A double-sided disc type AFPM with internal slot-less stator and twin rotors is called as torus motor, and is shown in Fig. 3.4.

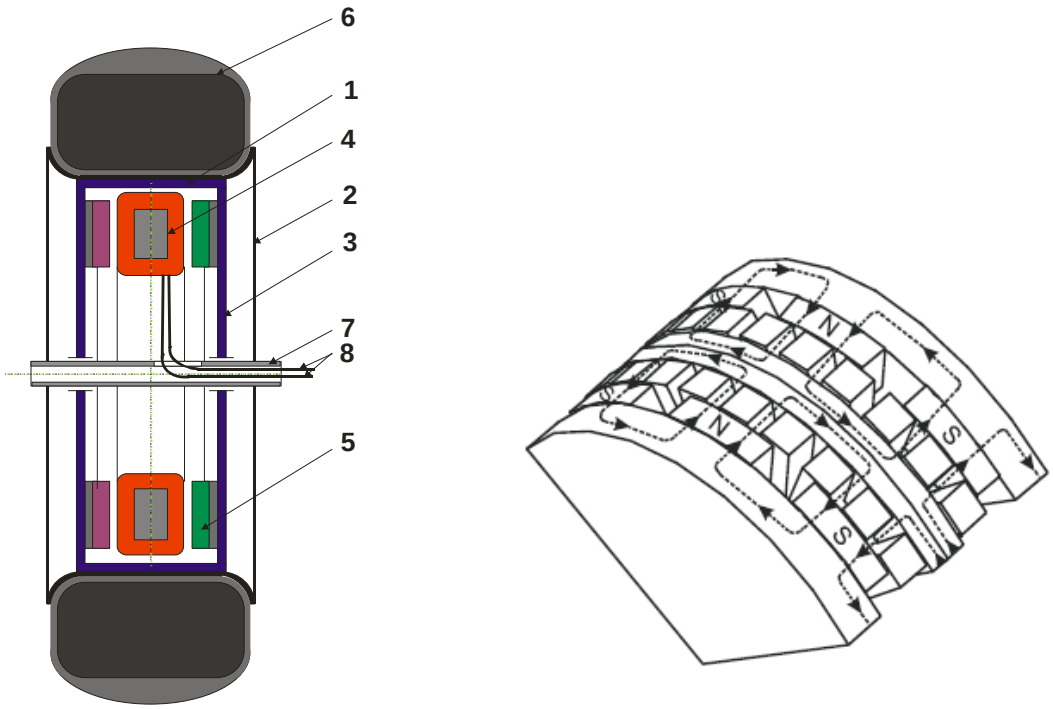

(a) **(b)**

Fig. 3.4. Torus motor: (a) Applied as hub drive: 1 - motor, 2 - wheel rim, 3 - rotor, 4 - stator, 5 - permanent magnets, 6 - tire, 7 - wheel axle, 8 - supply leads, (b) Flux distribution

Advantages of torus motor include balanced stator-rotor attractive forces unlike strong axial attractive forces in a single-sided machine, better winding utilization, better heat disposal due to the rotating rotor discs and adjustable air-gap. In a torus motor, the stator core is sandwiched between two rotor discs (with surface mounted permanent magnets) rotating at the same speed, and is made of laminated iron equipped with Gramme's type winding. A multi-disc axial flux PM motor is shown in Fig. 3.5.

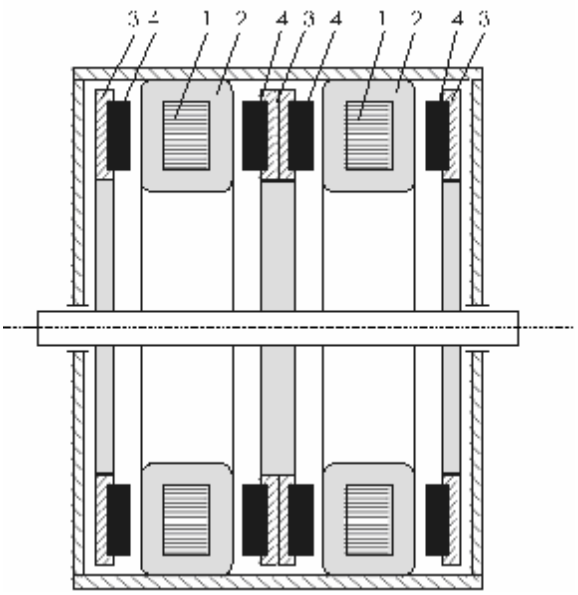

Fig. 3.5. Multi-disc AFPM machine: 1-stator core, 2-stator winding, 3-rotor, 4-magnets [43]

The torus motor has become topic of interest for electric vehicles in the latest years. For a desired torque value, a strategy to determine the optimum magnet length and coil depth, of a torus motor for electric two-wheeler application is presented in [28]. As the magnet length increases, the flux density increases and thus the torque initially increases, but beyond a certain value, the torque value reduces due to reduction in electrical loading. Improper assembling of rotor and stator results in a non-uniform air gap causing vibration, torque pulsations, noise and

ultimately deteriorates the machine performance. A double-sided internal rotor motor is employed as an in-wheel motor of electric vehicle by Hredzak [29] and the torque pulsations due to stator-rotor misalignments caused by uneven road conditions are successfully eliminated using a vector control scheme.

It is found that the shape of PM pole has an influence on the axial flux PMDC machine performance. The effect of trapezoidal and rectangular poles, of the same volume, on torque ripple of a torus and disc-type axial flux motor is investigated by E.A. Mendrela [6]. For a slotted torus type motor, the rectangular shaped magnets, shown in Fig. 3.6.(b), proved to reduce the cogging torque and thus the torque ripple. However, for a salient pole disc motor, the shape of PM poles did not influence the cogging torque. Another study [30] compares torus type brushless DC motors with slot-less stator and slotted stator having short teeth and long teeth both having either laminated iron or magnetic composite to fill the space between adjacent stator coils. It was concluded that the average torque and motor efficiency increased when the empty space between coils is filled with these materials. A recent study is focused on the usage of advanced magnetic materials for axial field brushless permanent magnet motor drives for automotive applications [7] and is not discussed here as it is out of scope of this dissertation.

Fig. 3.6. (a) Trapezoidal PM pole, (b) Rectangular PM pole

One of the objects of this dissertation is a double-sided AFPM brushless DC machine with salient-pole twin-rotor and internal slot-less stator. This motor is modeled and analyzed to study the torque performance for the application as in-wheel motor of an electric vehicle.

3.3 Applications

In general, the topology of an AFPM motor is complicated and the torque is produced at a continuum of radii on the disc rather than at a single radius. Strong attraction forces exist between the rotor permanent magnet and stator disc causing difficulties in assembling the machine as well as maintaining a uniform air gap [25]. However, due to their high efficiency, low cost and simple drive requirements, the AFPM BL motors make a good choice for the in-wheel motors of electric vehicles. An AF (double-sided, internal rotor) PM BLDC motor is designed for the direct-driven wheel of an electric motorcycle in [27]. The motor is optimized with respect to parameters like limited space, current density of conductors, flux density saturation and source voltage while providing a long driving range. It was found that the larger the air gap, larger the reluctance and lower the efficiency. Also, thicker rotor produces more Magneto-Motive Force (MMF) and thus improved the efficiency. The four-phase motor provided lower torque ripple and higher efficiency than a three-phase motor.

Double-sided AFPM BL motors are becoming increasing popular for direct-driven electric vehicle applications due to their compact structure and high power density. Liquid cooled AFPM BL machines are employed in HEVs [49]. The AFPM machines can be used as propulsion sources in ships, unmanned submarines and aerospace applications. By accommodating large number of poles, they can be used for low speed applications such as electromechanical traction drives and hoists. Gearless drives for elevators utilize AFPM BL

motor installed between the guide rails of car and hoistway wall [25]. The multi-disc AFPM machines can also be applied for power generation as high-speed and low-speed generators, and make good renewable energy sources. Other applications of AFPM motors include computer hard disk drives, in-wheel motor of electric wheel chairs, adjustable speed pump drives, fly wheel energy storage system particularly for vehicular applications, fans, robots and industrial equipment like machine tools.

CHAPTER 4: RADIAL FLUX PM MOTORS

4.1 Introduction

The first patent on a Radial Flux (RF) machine was filed by Davenport in 1837, much after the existence of axial flux machines is known. Radial flux PMBL motors have magnets in the shape of arc placed on the rotor. The rotor and stator cores have cylindrical construction with permanent magnets and armature windings respectively placed on them. The name is justified by the radial direction of flux lines in the air-gap with respect to the motor shaft. The motor dimensions such as the pole pitch of an RFPM cylindrical motor are not a function of radius as in the case of AFPM disc motor. Thus, the torque produced can be obtained as a product of force and radius of the motor at a constant radius. The construction of a RFPM machine is not as compact as an AFPM machine. However, the RFPM machine is easier to build than an AFPM machine which is associated with manufacturing complexities. The axial length to motor diameter ratio of an RFPM machine is higher than that of an AFPM machine with the same output power making it look bulkier.

4.2 Types of RFPM BLDC Motors

Based on geometry, the RFPM motors can be categorized as follows:

- with respect to stator and rotor position
    - Single-sided: Inner rotor / Outer rotor
    - Double-sided: Dual-rotor with internal stator/Dual stator with internal rotor
- with respect to stator structure
    - Slotted stator / Slot-less stator
- with respect to rotor magnet position

- Surface magnet / Interior magnet / Inset magnet

A detailed discussion on various rotor structures and the comparison of slotted versus slot-less stators is already provided in Chapter 2. The slotted stator motors can be found in many applications but the slotless motors are considered as specialty motors.

The single-sided machines are common configurations, however, the double-sided one is rarely found in literature. The inner rotor motor has lower inertia and offers better heat disposal as the stator windings are exposed to air. It has smaller motor diameter when compared to the outer rotor motor and is suitable for applications demanding low mechanical time constant as well as small-size. On the other hand, constant speed applications require larger inertia which is provided by an outer rotor motor [31]. Since the rotor, that is, the rotating part is the peripheral part, it is easy to integrate it into the wheel rim of an electric vehicle for propulsion purpose. The drawing of an outer rotor radial flux PMBL motor is shown in Fig. 4.1.

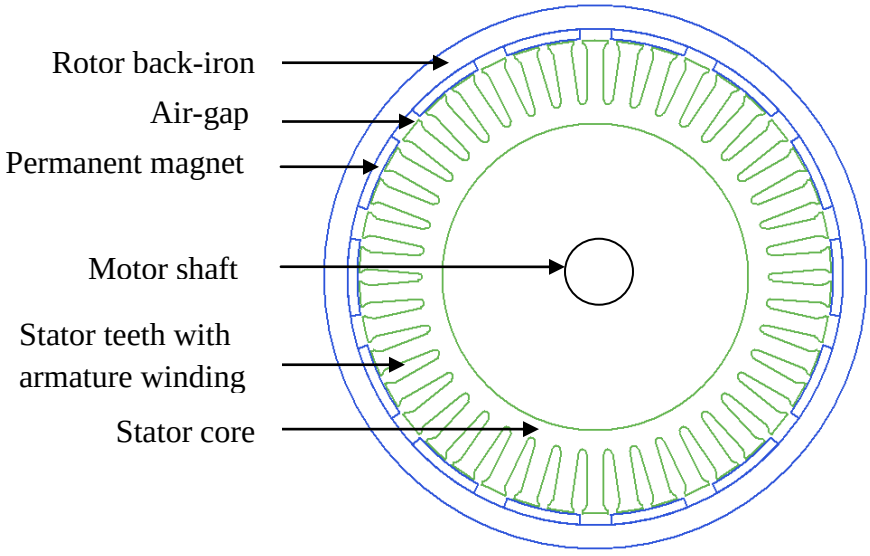

Fig. 4.1. Schematic of a single-sided outer rotor slotted stator RFPM BL motor

In this dissertation, an outer-rotor surface-magnet slotted-stator cylindrical RFPM BLDC motor is designed and the prototype is employed as an in-wheel motor of a gearless drive for electric wheelchair application.

The output torque of a PM machine, with same electrical and magnetic loading, is proportional to the air-gap cylindrical surface. The twin-rotor RFPM motor has two air-gaps and hence produces significantly higher torque than a single-sided machine. A twin-rotor toroidally wound RFPM motor prototype built by Qu [32], provided a torque density almost three times that of a conventional induction machine operating with the same power and speed while maintaining a high efficiency. As the rated power increases, the torque density of a twin-rotor RFPM motor increases more rapidly than a conventional induction machine. The twin-rotor internal stator RFPM BLDC machine considered in this dissertation, for in-wheel motor application, has iron core slot-less stator with armature windings embedded in between two rotors, with surface mounted permanent magnets, rotating at same speed. The structure of this machine is shown in Fig. 4.2.

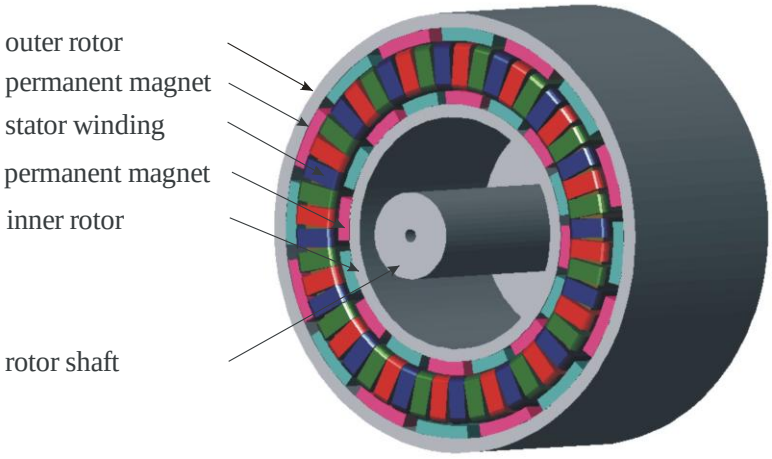

Fig. 4.2. Structure of a twin-rotor RFPM BL motor with slot-less stator

The magnetic flux from PM passes through the air-gap to the stator core and takes a path in return through the stator laminated iron to the air gap and then the rotor back-iron, as shown in Fig. 4.3. The magnetic flux of the PMs on inner rotor and outer rotor are directed in/out and out/in respectively. This flux through the stator core, during rotation, induces back-emf in the phase windings. The armature windings are supplied with trapezoidal or square-wave voltages. The flux and currents in the outer airgap have a direction opposite to those in the inner airgap (as the PMs on outer and inner rotor are magnetized in North-South configuration), but the torques obtained by the interaction of these fluxes and currents aid each other and sum up to produce the resultant torque of the motor. The principle of operation of the twin-rotor RFPM BL motor is essentially the same as that of a brushless PM motor discussed in Chapter 2.

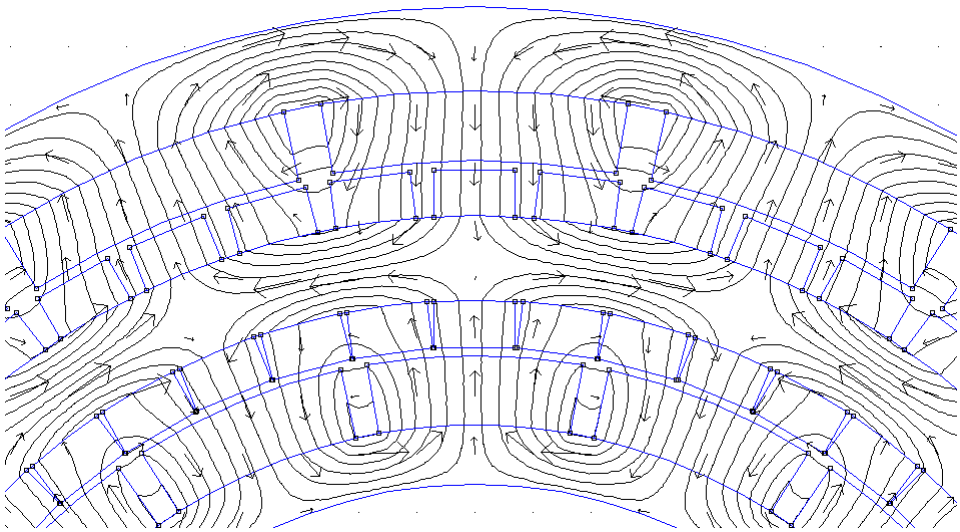

Fig. 4.3. Magnetic flux direction in a twin-rotor RFPM motor

Due to the absence of stator teeth, the twin-rotor RFPM BLDC motor has no cogging torque, lower torque ripple (which means smooth operation for EVs) and produces less noise. The slot-less motor has larger air-gap than a slotted one and thus, only a little armature reaction is present. Thus, the back emf of stator windings practically does not vary with mechanical load

leading to high overload capability. However, the larger air-gap machines need thicker and expensive magnets to produce the required flux density.

The task of machine optimization is a critical problem and it depends on the desired performance criteria such as required torque, output power and the motor design parameters like outer diameter, magnetic flux density in the stator and rotor cores, number of poles, electrical loading, length of air gap, etc. Often the optimization is an iterative process between the variable design parameters and the desired machine performance. In order to achieve this, a few parameters might be fixed based on the application requirements. For example, the magnetic loading can be fixed and the rotor and stator core thickness can be varied to obtain the desired value of flux density; the electrical loading can be fixed and the number of conductors, conductor cross-section area can be varied to achieve the required current density. An optimization study on the dual rotor RFPM motor is found in [33].

The twin-rotor RFPM machine has higher torque density than a conventional PM machine of the same volume due to a higher torque produced in the outer air-gap of the former [32]. Also, the end connection length of the windings for a RFTR PM machine is much shorter than a conventional RF PM machine resulting in lower losses and higher efficiency of a RFTR PM motor. Further, an RFPM machine with larger diameter yields higher torque whereas the end winding connection length is independent of machine diameter resulting in the same copper loss for a larger diameter machine with the same volume of copper and same current density. However, keeping the number of poles constant, the end winding connection length of a pancake or single-sided AFPM machine increases linearly with machine diameter contributing to higher losses for bigger machines, making the RFTR PM machine a strong competitor. A further insight into the end-winding effects can be obtained from [32]. It is also proposed that connecting both

the rotors by a disc, with punched holes, at one end will serve as a cooling fan for the machine and makes the heat removal easy.

Dual stator induction machine drives are frequently found in literature but, a dual-stator RFPM motor is not quite common. The latter does have an increased torque density than a conventional RFPM motor, but may be less than a dual rotor topology due to longer end winding connection lengths arising from two stators needing dual excitation. The experimental results showed that the dual stator RFPM machine had a low torque ripple and it yielded a torque about 1.5 times that of a conventional RFPM motor of the same size, but it suffers from high iron losses, which are at least 13% at the rated shaft torque [34], [35].

4.3 Applications

The outer rotor RFPM motor is an attractive choice for automobile applications since it is easy to attach load to the exposed rotating rotor and it can be easily integrated into the gearless direct driven electrical drive of any MPV such as electrical wheel chairs, EV such as golf carts, or HEV. For the same reason, it is also applied in machine tools. Other applications of outer rotor motor are magnetic and optical data storage systems and cooling fans [31]. A prototype of the outer rotor RFPM motor is applied as in-wheel motor of an electric wheel chair in the current dissertation. The inner rotor RFPM motors are found in conveyors, elevators, pumps and compressors. They are also employed in servo applications like robotics and in manufacturing sector for automation.

Twin-rotor RFPM machines are apt for moderately high speed applications. Because of the outside rotor being exposed, they are more suitable for applications like fans. Due to their high torque density and high efficiency, they can be used as propulsion source for automobiles,

and other applications in the aerospace industry. This dissertation investigates it for in-wheel motor applications of EVs.

The energy from rotational flow of main propeller stream can be recovered by employing an additional counter-rotating propeller in marine propulsion systems. In a research by Paplicki [45], dual-rotor slotless PM disc and cylindrical motors with counter-rotating rotors are studied and compared for the application of contra-rotating propellers (CRP) in ship propulsion drives. Both the motors employ same mass of magnets; have same active length and current density. It was found that the dual-rotor cylindrical motor produced highest electromagnetic torque. The advantages of motors with counter-rotating motion of active elements are minimum noise, vibrationless operation, high dynamics, energy saving and reliability.

The dual-stator RFPM machine is not well known in literature. It is capable of providing high torque at low speed, which makes it suitable for direct drive applications. A novel hybrid excited dual-stator PM synchronous machine for the application of wind generator is reported in [36].

CHAPTER 5: TECHNIQUES FOR COMPARATIVE STUDY

As seen from the previous chapters, both AFPM and RFPM motors are suitable for electric vehicle applications. The choice of a motor for in-wheel application of EV is a critical issue. It depends on the torque and power required to drive the vehicle, and is restricted by factors like volume or size (space occupied by motor), efficiency and cost of the motor. Therefore, there exists a necessity to compare the AFPM and RFPM motors with respect to these criteria for the selection of a more appropriate in-wheel motor.

Twin-rotor PMBL motors are considered as specialty machines. Traditionally, the torque performance of such machines is computed by modeling and analyzing the motor in Finite Element Modeling software, which not only requires the expertise pertaining to the software but also take long hours. The more complicated the model, the longer the simulation time. Thus, a comparative study requires analysis of more motors in FEM, which means it would take at least a few days or worse, a few weeks, to determine which motor gives better performance. On the other hand, not much literature exists on the twin-rotor motor, and not a lot is known about the torque expressions for the twin-rotor motors. This issue gave rise to the problem statement of the current dissertation and analytical torque equations are developed for the twin-rotor AFPM and twin-rotor RFPM motors. With the help of the Express Comparative Method (ECM) developed in this research, one would be able to determine which motor gives better torque output for particular wheel dimensions, in a fraction of minute.

5.1 Existing Literature and Techniques

The dual rotor RFPM machines are not studied extensively until the past decade, and only very few researchers have carried out its comparison with a dual rotor AFPM (or torus)

machine. Also, the single sided outer rotor RFPM motor is not found in many comparative studies though the inner rotor configuration is most commonly found. This dissertation compares the above mentioned three motors by means of analytical calculations. Finite element modeling and analysis is carried out to evaluate the accuracy of the newly developed analytical approach.

In many cases, the comparison method depends on the nature of application of motors. Six different types of double-sided AFPM and single-sided RFPM machines with slotted and slot-less stators, with internal rotor and external rotors, with the same output power, speed and number of poles are compared in [37] and the sizing equations are developed for each motor. Chen [38] compared a conventional single sided inner-rotor RFPM motor, a multi-stage AFPM motor and a three-phase Transverse Flux (TF) PM motor for downhole applications in wells. Analytical calculations were carried out to vary the pole number and machine axial length and to find their effect on torque density, machine efficiency and power factor. The sizing and comparison of internal rotor double-sided AFPM and internal rotor single-sided RFPM machines is discussed in [39] and the manufacturing as well as mechanical constraints are not ignored.

While numerous comparative studies exist on multistage AFPM and single sided RFPM machines, only a handful used the double-sided RFPM machine as an object of their comparative study. A couple of those publications are briefly discussed to get an insight into the dissertation topic. In a research by Bomme [40], radial flux and axial flux PMSMs with dual rotors and slotted stators are modeled analytically for medium and high speed applications. The radial flux machine has buried magnets on inner rotor and surface mounted magnets on outer rotor, whereas the axial flux machine has buried magnets on both rotors. The outer radius and current density are chosen to be identical for both machines. The electromagnetic torque and power are compared analytically. The results indicate that the dual air-gaps AFPM machine provides a

higher torque, as well as good cost to performance ratio than the dual rotor RFPM machine for any combination of the number of pole pairs and number of slots. However, the analytical computation and 3D Finite Element Modeling of AFPM machine differed in torque value by 30%, which is a huge number.

In another study by Qu [41], the performance of slotted AFPM and RFPM BLDC machines with surface mounted magnet dual-rotors, operating at constant speed and at four power levels, are compared. The output power, electrical and magnetic loadings, air gap and air gap flux density of both the machines are identical at each power level. Some of the entities compared are torque per unit active weight, torque and power per unit active volume, pole number effect, efficiency, material cost and weight, magnet material effect, etc. Also, the machine length-to-diameter ratio of RFPM machine and stator inner diameter-to-outer diameter ratio of AFPM machine are optimized to obtain maximum torque density and the highest efficiency. For RFPM machine, the length-to-diameter aspect ratio at which the optimization is achieved is found to be 0.5 and for the AFPM machine the diameter ratio is between 0.5 and 0.6.

Analysis is carried out in [41] with an aspect ratio of 0.5 for RFPM and diameter ratio of 0.55 for AFPM. It was also found that at same torque density but for higher power levels, the RFPMs may obtain higher torque-to-mass ratio than AFPMs. The iron mass is almost the same for both machines. Both machines use the same number of poles at each power level. Since AFPMs use more magnet material and RFPMs use more copper, the total active material cost for AFPMs is higher than that of RFPMs. RFPM need better cooling as its air gap is smaller and the loss per airgap area is higher than that of an AFPM. As the pole number increased, the efficiency decreased and RFPMs are more sensitive than the AFPMs to this factor.

A generalized geometric approach is adopted by Chrisanov [42] to develop an express comparison analysis of radial and axial flux PMSMs. Based on the derived expressions, a 3D plot of the volume ratio of these machines is obtained at various geometric sizes and at different number of poles. It indicates that the AF PMSM has higher torque density and power density (about 1.5 to 2 times) than the RF PMSM at increased number of poles (>4) and at certain stator and rotor configuration. This particular rotor and stator configuration refers to the design parameter n, which is the ratio of rotor radius of RFPM motor to the torque radius of AFPM motor, and $n < 0.65$ to achieve the above performance criteria.

The above technical publications provide an insight into the comparison of dual rotor AFPM and RFPM motors. However, it should be understood that no attempt is made earlier to compare the torque capabilities of these motors with respect to the motor external diameter. This dissertation predicts the torque output ratio of twin-rotor AFPM and RFPM motors for various wheel diameters and axial lengths.

5.2 Express Comparative Method

Testing in automobile industry related to vehicle performance is time consuming, labor intensive and expensive to deal with. Thus, comparing motors on a case to case basis is not a suggested approach. Comparison by means of universal analytical expressions is a smart way to quickly evaluate the motors and it saves labor, cuts the cost and is reliable. On the other hand, the analytical approach provides us an idea about the performance of motors even before attempting to model the machines and simulating them. Upon determining which motor meets the application requirements, this particular motor can then be analyzed using advanced modeling software tools based on Finite Element Method (FEM) to verify the analytical result

and to optimize the construction of this motor. Once this is done, one can confidently build a prototype of the motor and test it. In this dissertation, an analytical approach, free of computer simulations, is developed to compare RFTR PMBL, AFTR PMBL and conventional single-rotor RF PMBL motors with slot-less stators. Later, 3D FEM software models of the motors are built to validate the theoretical results.

RFPM motors compete with AFPM motors in terms of efficiency and torque density. In order to be able to compare two motors, they should obey some initial conditions or have certain identical design parameters such as current and magnetic loading, and identical performance characteristics as output power, speed of rotation, etc. The current research aims at finding which of these two motors (of the same motor diameter) when fit into the wheel of an electric vehicle delivers higher torque at same speed and same electromagnetic load. To achieve this, the formula for electromagnetic torque of each of these motors in terms of the wheel dimensions, that is its axial length and diameter, needs to be derived. A sketch of the objects of comparison, AFTR PMBL, RFTR PMBL and single-rotor RFPM motors with slot-less stators is shown in Fig. 5.1, and the dimensions are marked.

Before proceeding further, the following assumptions are made:

- Electric load J (A/m) of the inner part of the radial flux motor (at radius r_i^r in Fig. 5.1(b)) is equal to the electric load of the disc motor at the inner radius r_i^a of the stator core of axial flux motor (see Fig. 5.1(a))
- Magnetic load B_{av} (T) of all three motors is the same
- Speed ω_m of the motors is the same

- Outer diameter and axial length of the active elements (stator and rotor cores as well as windings) of the motor are the same.

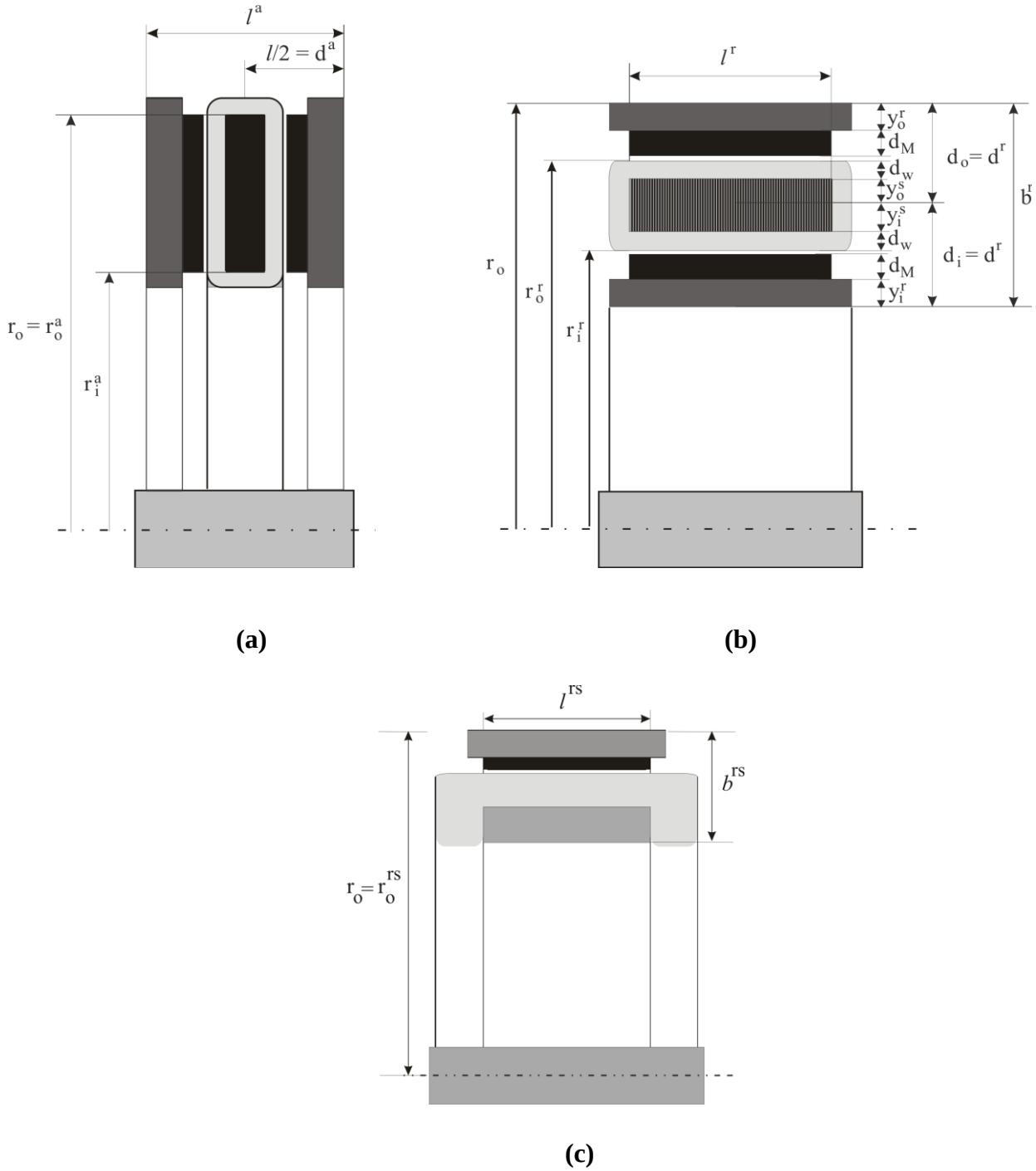

Fig. 5.1. Section of: (a) twin-rotor AFPM motor, (b) twin-rotor RFPM motor, (c) single stage outer-rotor RFPM motor

Other simplifying assumptions are introduced:

- Resistance and leakage inductance of the stator windings are neglected
- Dimensions of end windings are ignored
- Eddy current and hysteresis power losses are ignored
- Saturation of magnetic circuit is not considered
- Permanent magnets on rotor disc have temperature independent properties

Since the geometry of AF PM and RF PM motors is different, a formula for electromagnetic torque as a function of geometrical dimensions will be derived separately for all three types of motor.

5.2.1 Torque Expression for RFTR PMBL Motor

In general, the electromagnetic force density, F_x exerted on a surface with current density, J_z being under the influence of a magnetic flux density, B_y (illustrated in Fig. 5.2) is given as:

$$F_x = J_z \cdot B_y \tag{5.1}$$

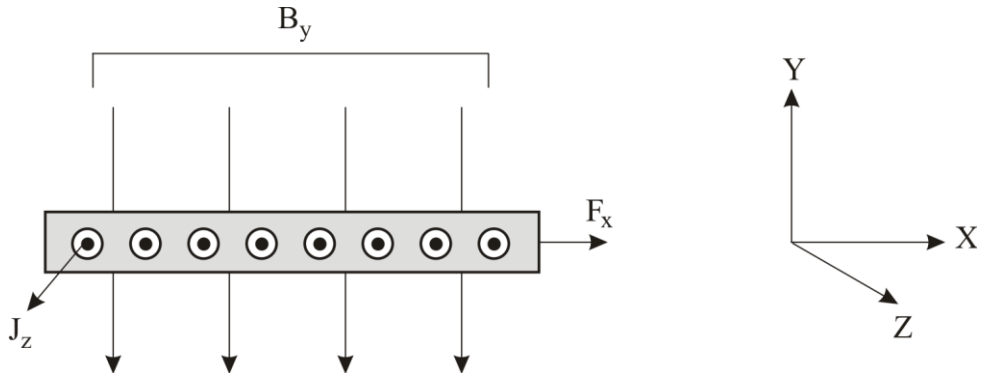

Fig. 5.2. Explanation to equation (5.1)

In case of brushless DC motors, the rotating magnetic flux vector, $\vec{B}$ is perpendicular to the current vector $\vec{i}$ (see Fig. 5.3).

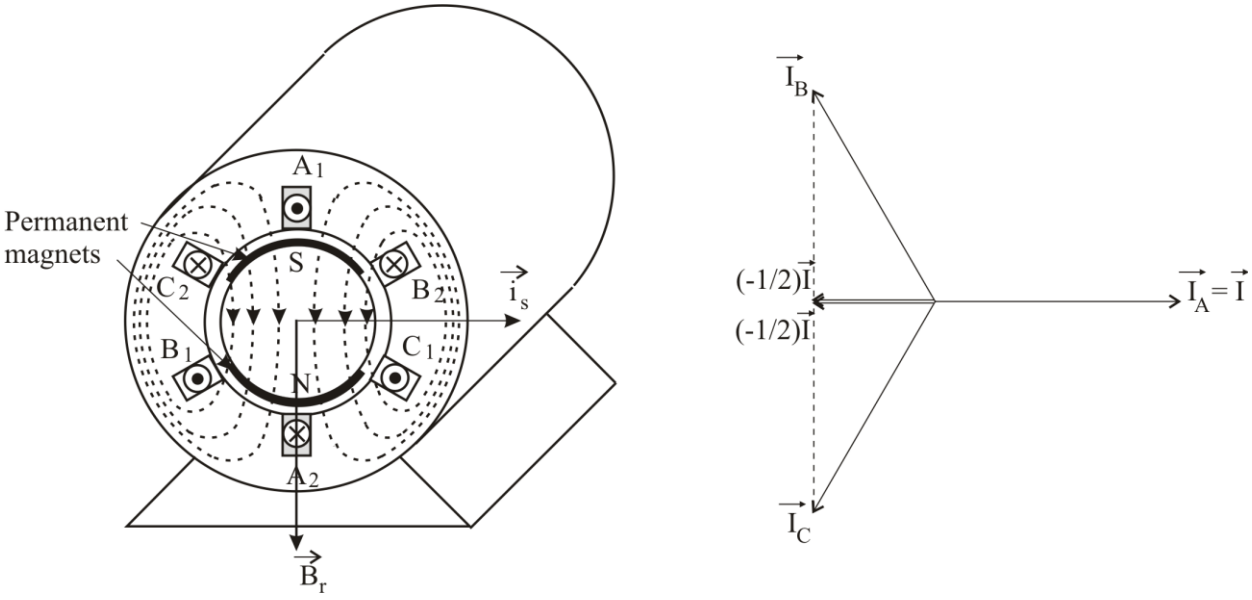

(a) **(b)**

Fig. 5.3. (a) Rotor flux and stator current directions in PMBL DC motor, (b) Winding currents at time instant t_1

Let us assume that the currents shown in Fig. 5.3(b) correspond to the time instant t_1. For the same time instant t_1, the position of rotor permanent magnet with respect to the stator winding, in case of slot-less winding, is as shown in Fig. 5.4 (a).

The electromagnetic force, F_{em} produced by the motor of length, l over the area, Ap of one pole pitch, τ_p can be expressed as follows (from (5.1) and Fig. 5.4(b)):

$$F_{emp} = \frac{2}{3} A_p \cdot J \cdot B_{av} \tag{5.2}$$

where $A_p = \tau_p \cdot l$ and $J = \frac{N_t \cdot I_{max}}{\tau_c}$

N_t is the number of turns of the coil, I_{max} is the maximum current in the coil and τ_c is the coil pitch.

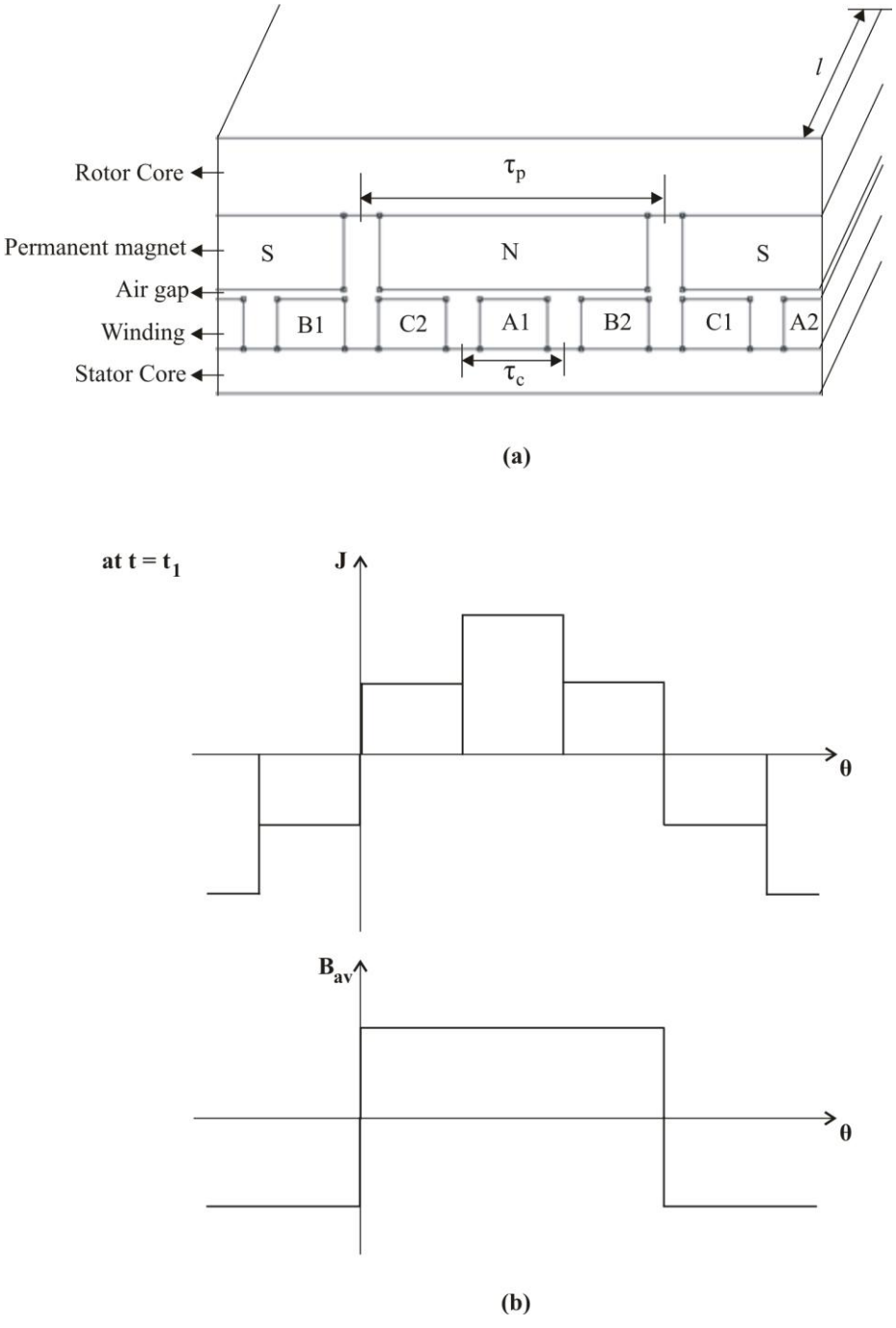

Fig. 5.4. (a) Position of rotor PM with respect to stator coil at time instant t_1, (b) Profiles of current density and magnetic loading

The electromagnetic torque produced by the motor is then obtained as:

$$T_{em} = p \cdot F_{emp} \cdot r_g = \frac{2}{3} \cdot A_g \cdot J \cdot B_{av} \cdot r_g \tag{5.3}$$

where $A_g = 2\pi r_g \cdot l = p \cdot A_p$ is the total area of the air gap.

The above expression allows to calculate the maximum torque of slot-less winding motor.

Due to switching of current in the winding phases, the torque waveform varies with time, which is exhibited as torque ripple (Fig. 5.5).

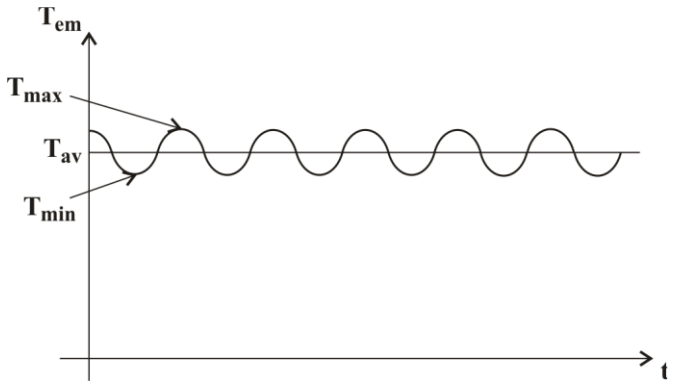

Fig. 5.5. Waveform of the varying torque

Thus, the average torque is slightly lower than the maximum torque. Besides, in case of winding with more coils per pole per phase (greater than 1) and coil span different than pole pitch (short pitched or fractional winding), the torque equation in (5.3) must be multiplied by winding coefficient k_w. The torque in such a case is given as:

$$T_{em} = \frac{2}{3} \cdot A_g \cdot J \cdot B \cdot r_g \cdot k_w \tag{5.4}$$

where $k_w = k_d \cdot k_c$

and k_d is the winding distribution factor, k_c is the chording (pitch) factor.

For a twin-rotor motor, the total torque T_{em}^r is a sum of outer part torque T_o^r and inner part torque T_i^r:

$$T_{em}^r = T_o^r + T_i^r \tag{5.5}$$

The torques T_o^r and T_i^r are the products of force densities F_o^r and F_i^r with radii r_o^r and r_i^r respectively:

$$T_{o(i)}^r = F_{o(i)}^r r_{o(i)}^r \tag{5.6}$$

In general, the electromagnetic force is:

$$F = \frac{2}{3} \cdot B_{av} \cdot J \cdot A \cdot k_w \tag{5.7}$$

where A is the area of air-gap (m^2), k_w is the winding coefficient, B_{av} is the specific magnetic loading in Tesla (average flux density over the air-gap) and J is the specific electric loading given by $J = \frac{N_t.I}{\tau_c}$. Here, N_t is number of turns of the coil, *I* is the maximum phase current and τ_c is the coil pitch.

Thus the electromagnetic force for the outer part is:

$$F_o^r = \frac{2}{3} \cdot 2\pi r_o^r l^r B_{av} J_o^r k_w^r \tag{5.8}$$

where: $J_o^r = \frac{N_t^r \cdot I}{\tau_{ci}^r}$ (5.9)

And for inner part:

$$F_i^r = \frac{2}{3} \cdot 2\pi r_i^r l^r B_{av} J_i^r k_w^r \tag{5.10}$$

where: $J_i^r = \frac{N_t^r \cdot I}{\tau_{ci}^r}$ (5.11)

The coil pitches of both parts are:

$$\tau_{co}^r = \frac{2\pi r_o^r}{N_c^r} \text{ and } \tau_{ci}^r = \frac{2\pi r_i^r}{N_c^r} \quad (5.12)$$

where N_c^r is the number of coils on stator

After substitution of (5.12) into (5.9) and (5.11), and then into (5.8) and (5.10) respectively, we obtain:

$$F_o^r = F_i^r = \frac{2}{3} \cdot B_{av} I^r N_t^r N_c^r l^r k_w^r \quad (5.13)$$

It means that the forces of both parts are equal. Since the number of coils N_c^r (each of the same number of turns N_t^r) on the inner part limits this number on the outer part, the force of both parts is expressed in terms of dimension of inner part. Thus the total torque is equal to:

$$T_{em}^r = F_i^r r_o^r + F_i^r r_i^r = \frac{2}{3} \cdot 2\pi r_i^r l^r B_{av} J_i^r k_w^r (r_o^r + r_i^r) \quad (5.14)$$

5.2.2 Torque Expression for AFTR PMBL Motor

The torque developed by axial flux motor expressed in terms of force acting on different values of motor radius is as follows:

$$T_{em}^a = 2 \int_{r_i^a}^{r_o^a} r dF^a \quad (5.15)$$

where dF^a is the force increment at radius r given by:

$$dF^a = \frac{2}{3} \cdot 2\pi r B_{av} J_r^a k_w^a dr \quad (5.16)$$

The current loading is different at each radius and is equal to:

$$J_r^a = \frac{N_t^a . I^a}{2\pi r} N_c^a \tag{5.17}$$

When (5.17) is substituted into (5.16), we obtain:

$$dF^a = \frac{2}{3} \cdot B_{av} I^a N_t^a N_c^a k_w^a dr \tag{5.18}$$

It means *dF* is the same at any value of radius *r*, it is also at r_i^a. Thus at radius r_i^a, the force:

$$dF^a = \frac{2}{3} \cdot 2\pi r_i^a B_{av} J_i^a k_w^a dr \tag{5.19}$$

By replacing dF^a of (5.19) in (5.16) and next in (5.15), the expression for torque is:

$$T_{em}^a = 2 \cdot \frac{2}{3} \cdot 2\pi r_i^a B_{av} J_i^a k_w^a \int_{r_i^a}^{r_o^a} r dr \tag{5.20}$$

After integration:

$$T_{em}^a = \frac{2}{3} \cdot 2\pi r_i^a B_{av} J_i^a k_w^a [(r_o^a)^2 - (r_i^a)^2] \tag{5.21}$$

5.2.3 Torque Expression for Single-rotor Slot-less Conventional Cylindrical RF Motor

The equations for a conventional RF PM motor can be obtained in a similar way as that followed for a RFTR PM motor, and are less complicated due to presence of only one rotor. From (5.8), the electromagnetic force on the outer rotor is given by:

$$F_o^{rs} = \frac{2}{3} \cdot 2\pi r_o^{rs} l^{rs} B_{av} J^{rs} k_w^{rs} \tag{5.22}$$

where the superscript ‘rs’ stands for single-rotor RFPM motor with usual meanings for all the quantities as listed before.

The current density is given by:

$$J^{rs} = \frac{N_t^{rs} \cdot I}{\tau_c^{rs}} \tag{5.23}$$

where coil pitch, $\tau_c^{rs} = \frac{2\pi r_o^{rs}}{N_c^{rs}}$ (5.24)

Substituting (5.24) into (5.23) and then into (5.22),

$$F_o^{rs} = \frac{2}{3} \cdot B_{av} I^{rs} N_t^{rs} N_c^{rs} l^{rs} k_w^{rs} \tag{5.25}$$

Therefore, the torque is obtained as:

$$T_{em}^{rs} = F_o^{rs} r_o^{rs} = \frac{2}{3} \cdot 2\pi l^{rs} B_{av} J^{rs} k_w^{rs} (r_o^{rs})^2 \tag{5.26}$$

5.2.4 Expressing Torques of All Motors in Terms of Outer Radius and Axial Length

As it was mentioned, the flux density B and current loading at inner radius are the same in all three motors. It means that

$$J_i^a = J_i^r = J^{rs} = J_i \tag{5.27}$$

To express torque in terms of outer radius of axial-flux motor, it is assumed that the relation between inner and outer radius is [44]:

$$r_i^a = k_{i/o} r_o^a$$

Substitution of this into (5.21) gives:

$$T_{em}^a = \frac{2}{3} \cdot 2\pi B_{av} J_i^a k_w^a (r_o^a)^3 (k_{i/o} - k_{i/o}^3) \tag{5.28}$$

The axial length l^a of torus motor and the radial thickness b^r, of twin-rotor radial-flux motor depend on B and J, and are assumed to be equal if the same number of magnetic poles is assumed. In both twin-rotor motors, this length is a sum of length of two regions, each being the sum of rotor yoke, magnets, air-gap winding layer and stator yoke (Fig. 5.1). In axial flux motor, these two parts are of the same length. In radial flux (Fig. 5.1(b)), the outer rotor yoke Y_o^r thickness is expected to be greater than the yoke of inner part Y_i^r, if the flux density B in two air-gaps are equal and the permissible flux density in yokes are equal. It is similar in case of stator yoke thickness Y_o^s of outer part which is expected to be slightly greater than the yoke Y_i^s of the inner part. However, in this simplified analysis, it is assumed that the thickness of both parts of the twin-rotor radial flux motor are equal to d^r and equal to d^a, the thickness of each part of axial-flux motor. It means $l = l^a$ and since $d_o = d_i$ (Fig. 5.1(b)), we have

$$2d^r = 2d^a = l^a = l \tag{5.29}$$

In case of single-rotor radial flux motor, the thickness of motor $b^{rs} = \frac{1}{2}b^r$ and its length l^{rs} is equal to the length *l*. Since it was assumed that the axial length *l* and outer diameter of each motor are equal, their torque values can be expressed in these two dimensions. The electromagnetic torque of axial-flux motor is then:

$$T_{em}^a = \frac{2}{3} \cdot 2\pi B_{av} J_i k_w r_o^3 (k_{i/o} - k_{i/o}^3) \tag{5.30}$$

For radial flux motor, according to relation shown in Fig. 5.1(b),

$$r_i^r = r_o - \left(\frac{d^r}{2} + d^r\right) \text{ and } r_o^r = r_0 - \frac{d^r}{2} \tag{5.31}$$

The relation (5.31) is true if assumption is made that:

$$Y_o^r + d_M = Y_o^s + d_w = Y_i^s + d_w = Y_i^r + d_M = \frac{l}{4} \tag{5.32}$$

The electromagnetic torque, after substitution of (5.31) into (5.14), takes the form:

$$T_{em}^r = \frac{2}{3} \cdot 2\pi B_{av} J_i k_w l \left[r_o - \frac{3}{2} d^r \right] [2r_o - d^r] \tag{5.33}$$

Since $l = 2d^r$, we have

$$T_{em}^r = \frac{2}{3} \cdot 2\pi B_{av} J_i k_w l \left[r_o - \frac{3}{4} l \right] \left[2r_o - \frac{l}{2} \right] \tag{5.34}$$

From (5.26), for the single-rotor RFPM motor, we have:

$$T_{em}^{rs} = \frac{2}{3} \cdot 2\pi l B_{av} J_i k_w (r_o)^2 \tag{5.35}$$

In the above equations, the radius r_o may be the inner radius of wheel rim, and length l depends on the axial length of the axial flux motor.

5.3 Results of Express Comparative Method (ECM)

Using the torque expressions in (5.30), (5.34) and (5.35), the torque for AFTR, RFTR and single-rotor cylindrical PMBL motors can be plotted as a function of motor diameter and axial length for a constant magnetic loading, electric loading and winding coefficient.

As an example, illustrations for such 3-D plots are provided here for a magnetic loading of 0.7 T, electric loading of 41.5 A-turns/mm and winding coefficient of 1. The ratio of inner to outer radius of the disc motor ($k_{i/o}$) is taken as 0.613. The three-dimensional plot for the torque of AFTR PMBL motor for different radii and lengths is shown in Fig. 5.6.

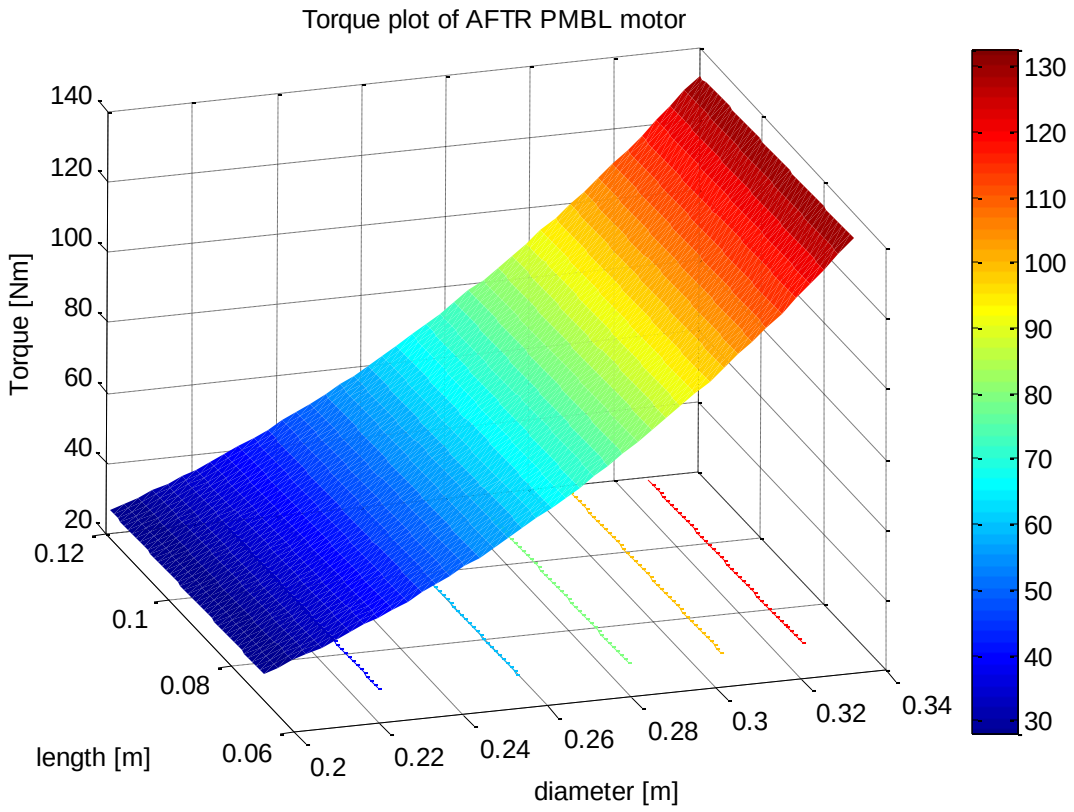

Fig. 5.6. Torque of AFTR PMBL motor as a function of wheel diameter and axial length

As can be seen from the expression in (5.30) and from Fig. 5.6, the torque output of a twin-rotor axial-flux PMBL motor is independent of the motor length and varies only with the motor diameter. The torque of the AFTR PMBL motor increased as the motor diameter increased.

The torque of a RFTR PMBL motor can be plotted in a similar way with the help of the expression in (5.34). This torque plot is shown in Fig. 5.7. Both the plot and the torque expression in (5.34) indicate that the torque output of this motor varies with motor diameter and length. The electromagnetic torque increased with an increase in the motor diameter and length.

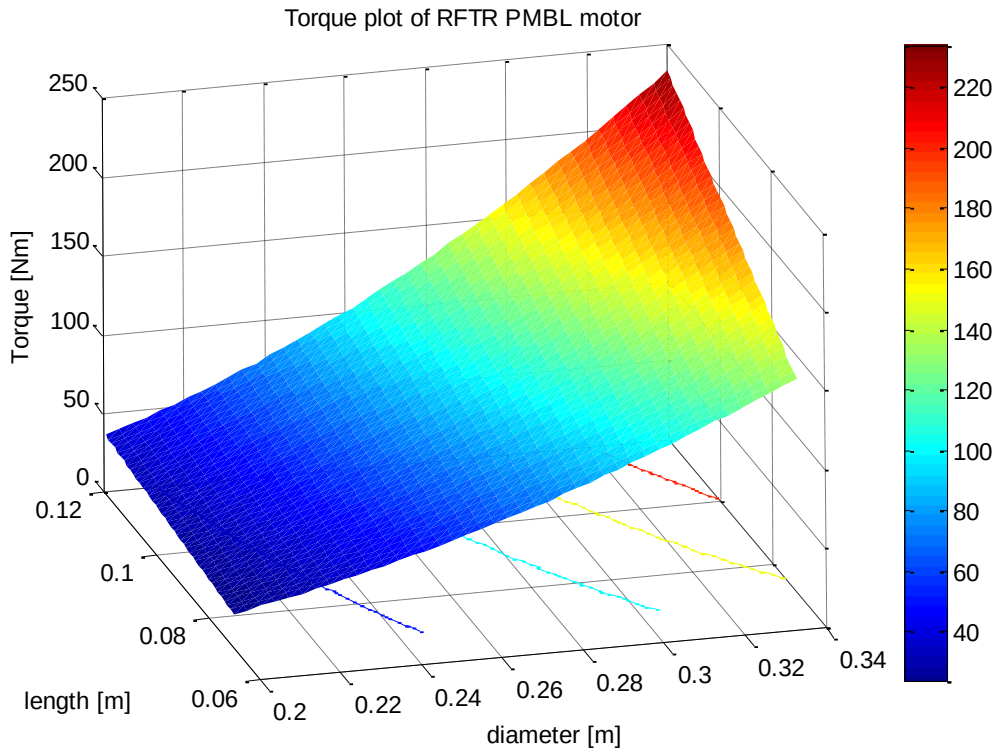

Fig. 5.7. 3D torque plot of RFTR PMBL motor

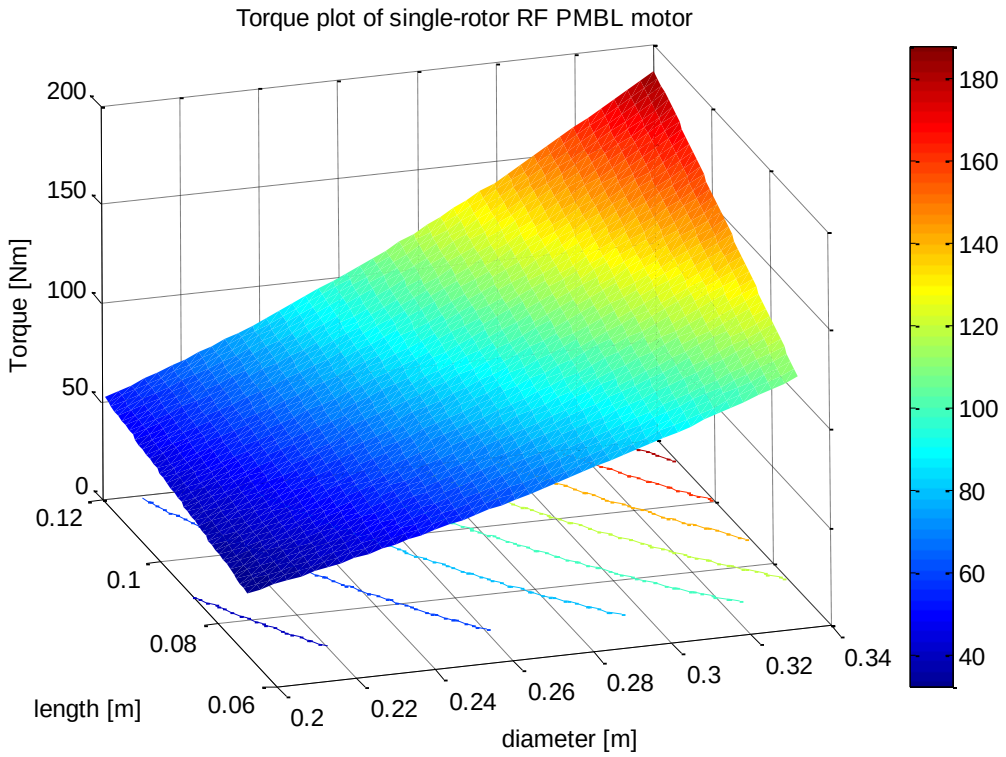

Fig. 5.8. Electromagnetic torque of single-rotor RFPM motor

From the expression in (5.35), the electromagnetic torque of a single-rotor RFPM motor is plotted as shown in Fig. 5.8. The torque output of this motor is proportional to the length and square of the diameter.

To evaluate the validity of Express Comparative Method derived in this dissertation, all the three kinds of motors are modeled in Finite Element Magnetics software, Maxwell (from Ansoft), for an outer diameter of 334 mm and axial length of 82.5 mm, with the same electrical loading, magnetic loading and winding coefficient as stated earlier. The modeling and analysis, and the simulation results obtained from the software are discussed in detail in the subsequent chapters. The electromagnetic torque values, obtained from ECM for all the three motors are plotted in 2-D space as a function of motor diameter for a fixed axial length of 82.5 mm, as shown in Fig. 5.9. The software results and the ECM results are compared in Chapter 10 and the error of the newly derived ECM technique is then obtained.

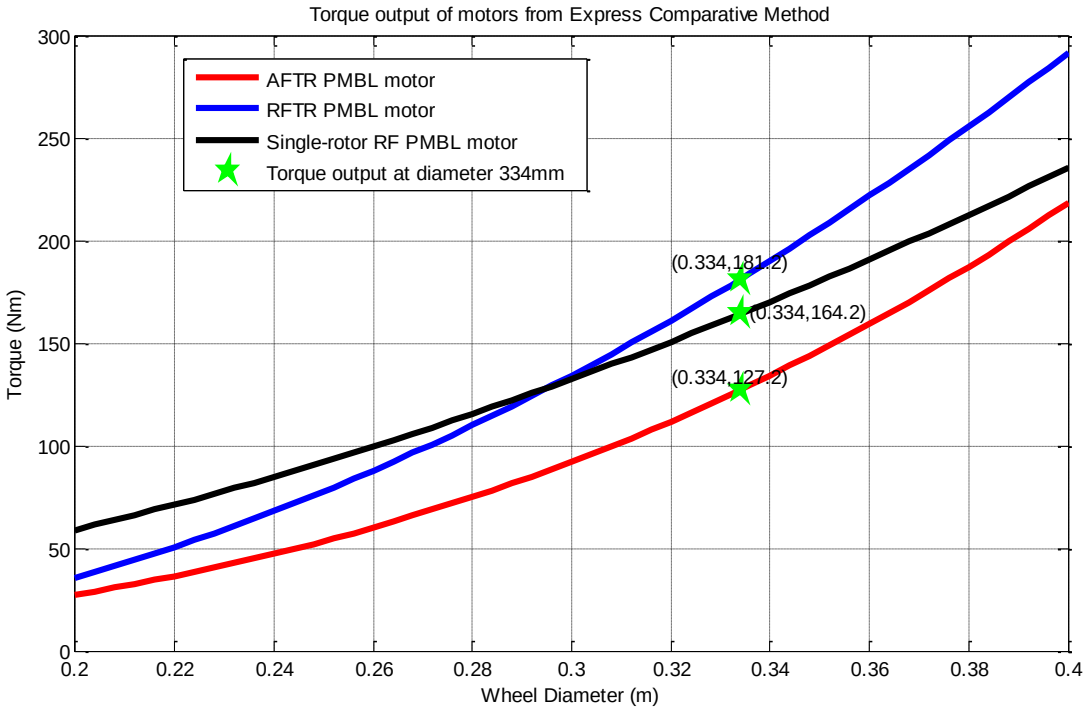

Fig. 5.9. Electromagnetic torque plots for the motor axial length of 82.5 mm

It can be seen from Fig. 5.9 that for diameters lower that 295 mm, the conventional single-rotor RF PMBL provides higher torque than both the twin-rotor motors. However, for larger diameters, over 295 mm, the twin-rotor RF PMBL motor quickly took over the single-rotor RF PMBL and the AFTR PMBL motors. The wheel diameter considered in this dissertation is 334 mm, for electric vehicle application. Hence, at this wheel diameter of 334 mm and axial length of 82.5 mm, the torque values obtained from the proposed ECM are tabulated in Table 5.1

Table 5.1. Electromagnetic torque values from ECM

	Single-rotor RF PMBL motor	**RFTR PMBL motor**	**AFTR PMBL motor**
Torque (Nm)	164.2	181.2	127.2

The electromagnetic torque values give us a quantitative estimate of the performance of individual motors. However, for a comparative study, we need to compare the torque output of one motor with respect to the other. Thus, we need to obtain the torque ratios for any two motors. Since we assume same magnetic loading, electric loading and winding coefficients for all the three motors, the torque ratio can be expressed as a function of the motor diameter and axial length. The twin-rotor radial flux to axial flux motor torque ratio with regard to (5.30) and (5.34) is:

$$T_{a/r} = \frac{T_{em}^{a}}{T_{em}^{r}} = \frac{r_o^3(k_{i/o} - k_{i/o}^3)}{l\left(r_o - \frac{3}{4}l\right)\left(2r_o - \frac{l}{2}\right)} \tag{5.36}$$

The above expression in (5.36) can be plotted in 3-dimensional space as shown in Fig. 5.10. The plot indicates that the AFTR PMBL motor provides better torque capability than the RFTR PMBL motor only at smaller diameters and lower axial lengths. For higher diameters and larger lengths, the RFTR PMBL motor is supreme than the AFTR PMBL motor. It should be

remembered that this plot corresponds to $k_{i/o}$ (inner radius to outer radius of AFTR PMBL motor) value of 0.613.

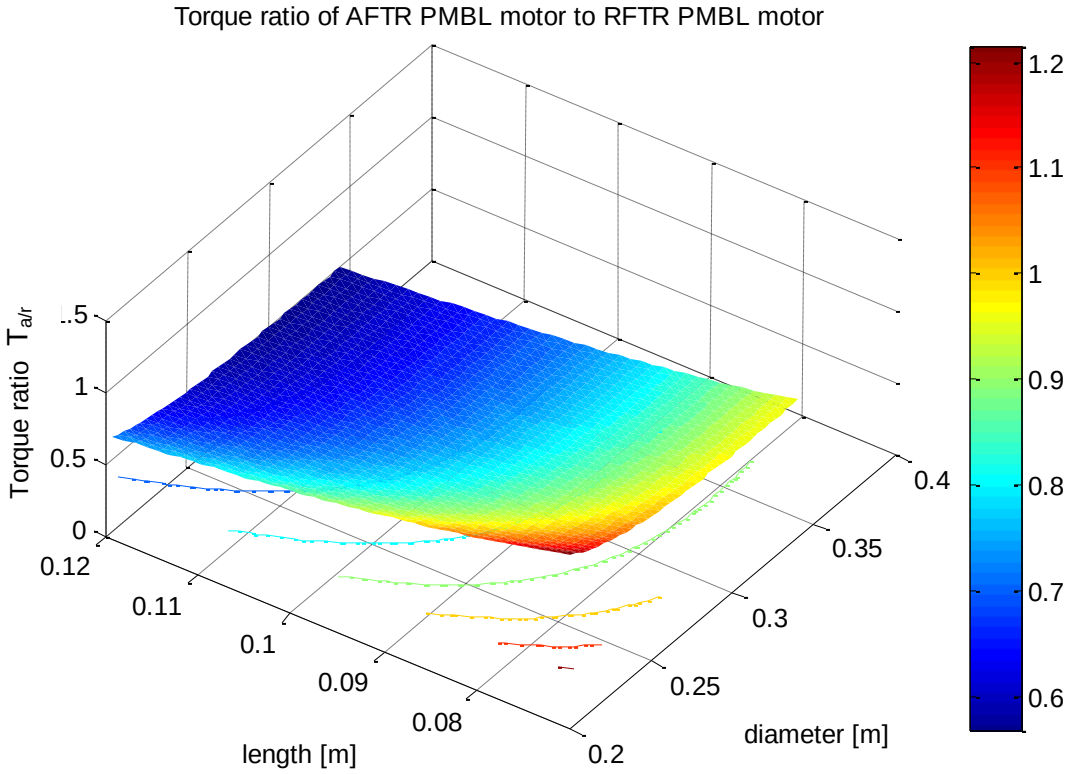

Fig. 5.10. Torque ratio of twin-rotor axial flux to twin-rotor radial flux PM motor

Similarly, the torque ratio of twin-rotor RFPM motor to single-rotor RFPM motor can be obtained from (5.35) and (5.34) as:

$$T_{r/rs} = \frac{T_{em}^{r}}{T_{em}^{rs}} = \frac{\left(r_o - \frac{3}{4}l\right)\left(2r_o - \frac{l}{2}\right)}{(r_o)^2} \tag{5.37}$$

The 3-D plot for the above torque ratio in (5.37) is shown in Fig. 5.11. This torque ratio is less than 1 for diameters lower than approximately 290 mm. However, for relatively higher diameters, the RFTR PMBL motor produced more torque, up to 1.3 times that of a conventional single-rotor RF PM motor with slot-less stator.

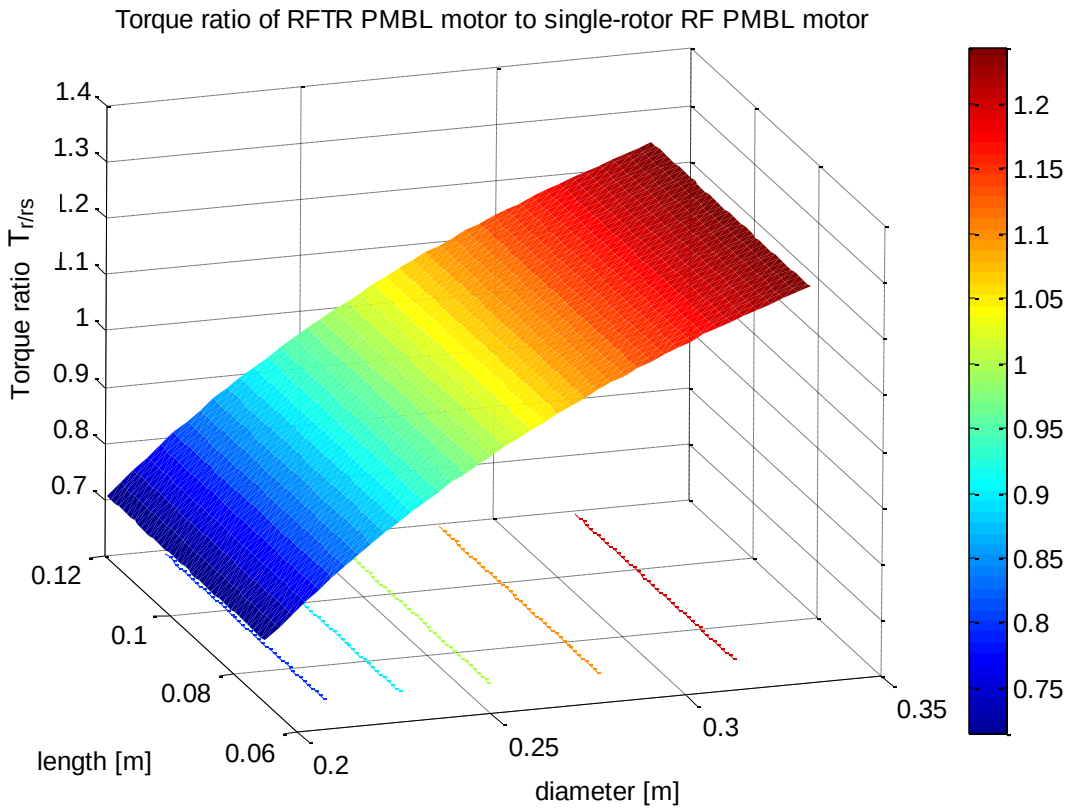

Fig. 5.11. Torque ratio of twin-rotor RF to single-rotor RF PMBL motor

The ratio of torque of twin-rotor AFPM motor to that of single-rotor RFPM motor is given from (5.30) and (5.35) as:

$$T_{rs/a} = \frac{T_{em}^{rs}}{T_{em}^{a}} = \frac{l}{r_o(k_{i/o} - k_{i/o}^3)} \tag{5.38}$$

The torque ratio in (5.38) is plotted and is shown in Fig. 5.12. The single-rotor RF PMBL motor clearly provided higher torque than the AFTR PMBL motor for most of the diameter and length range. For smaller length and higher diameter, the AFTR PMBL motor may be slightly advantageous than the single-rotor RF PM motor.

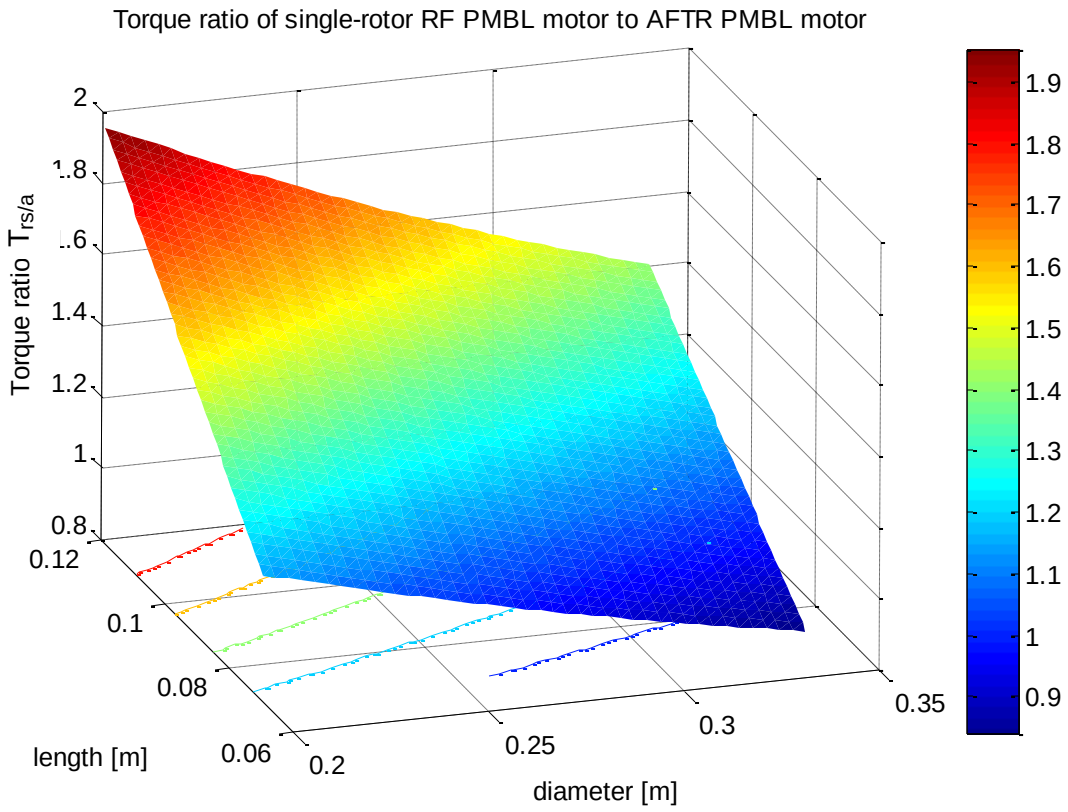

Fig. 5.12. Torque ratio of single-rotor RF to twin-rotor AF PMBL motor

To validate the ECM, the three torque ratios are calculated using FEM software in the later chapters for the motor length of 82.5 mm and diameter of 334 mm. The FEM analysis results are then compared with the results from ECM. The different torque ratios for all the three motors of axial length 82.5 mm, obtained from ECM are plotted as a function of motor diameter and this graph is shown in Fig. 5.13. The same electrical loading, magnetic loading and winding coefficient are assumed for the three motors, and these values are the same as the ones mentioned earlier in this subsection.

The torque ratio values for any two motors of diameter 334 mm and length 82.5 mm, obtained from ECM, can be read from Table 5.2.

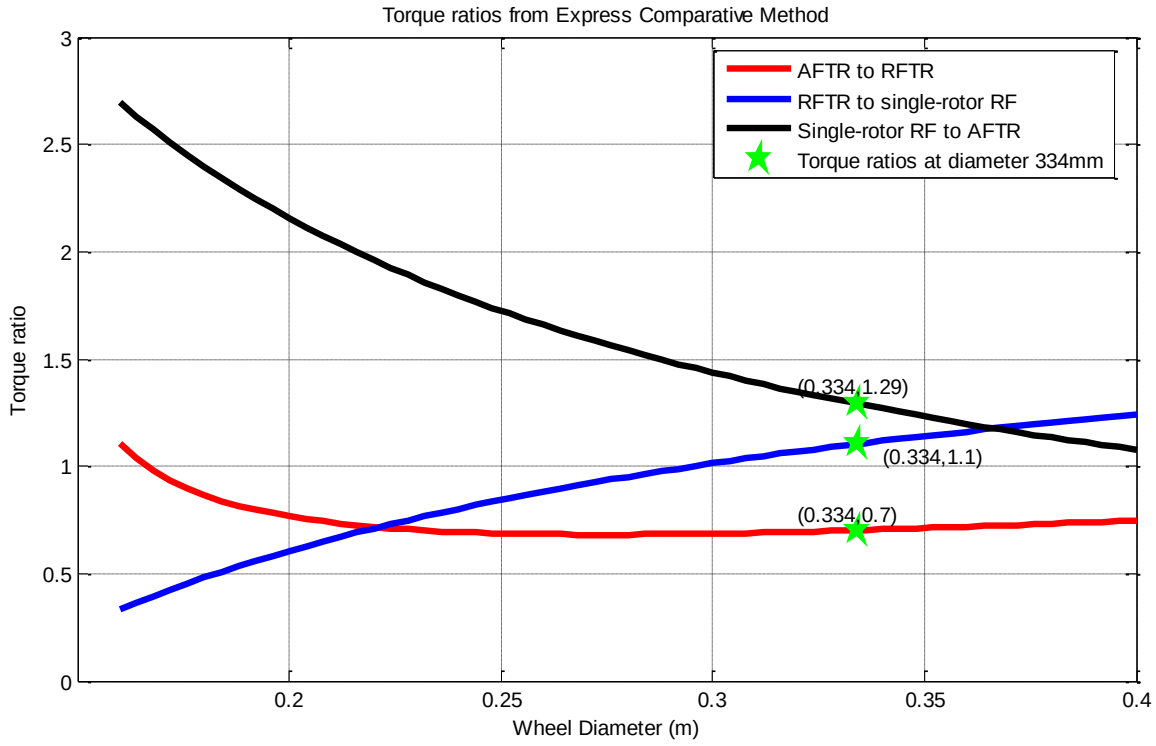

Fig. 5.13. Torque ratios obtained from ECM for a motor length of 82.5 mm

Table 5.2. Torque ratios from ECM for different motors

	Single-rotor RF to AFTR	**RFTR to Single-rotor RF**	**AFTR to RFTR**
Torque Ratio	1.29	1.1	0.7

To summarize the various results obtained from ECM, it can be stated that:

- The electromagnetic torque of an AFTR PMBL motor is independent of the motor length and is proportional only to the outer diameter and radius ratio, $k_{i/o}$.
- For motor diameters lower than approximately 295 mm, the single-rotor RF PMBL motor yielded higher torque than a RFTR PMBL motor of the same volume.
- For a wheel of diameter below 167 mm and axial length 82.5 mm, the AFTR PMBL motor is better to apply when compared to a RFTR PMBL motor. However, the single-

rotor RF PMBL motor always provided higher torque than the AFTR PMBL motor within the analyzed range of diameters from 100 mm to 400 mm.

- Table 5.3 shows the appropriate in-wheel motor for an axial length of 82.5 mm at different diameters.

Table 5.3. Determination of appropriate in-wheel motor using ECM

Wheel Diameter	**Motor Selection**
< 295 mm	Single-rotor RF PMBL motor
> 295 mm	RFTR PMBL motor

- FEM software modeling and analysis is complex and time-consuming. The proposed ECM method can be used to compute the torque output of any single-rotor RF, RFTR and AFTR PMBL motors with slot-less stator without the necessity of any FEM software. The torque ratios for any two motors are expressed as a function of motor diameter and axial length.
- The torque for the above three motors can be compared provided they have the same magnetic loading, electric loading and winding coefficients. This is a design challenge to have the same electromagnetic parameters for all the three motors, not only during the initial determination of motor design parameters and dimensions but also while modeling in FEM software, which is discussed in the subsequent chapters.

CHAPTER 6: TWIN-ROTOR AF PM MOTOR: MODELING AND ANALYSIS

6.1 Motor Data

The AF PM motor considered in this dissertation is a disc type twin-rotor PM BLDC motor with slot-less stator, as shown in Fig. 6.1. In other words, it is a disc motor supplied by three-phase winding connected in 2-Y structure. The data for this motor is provided in Table 6.1.

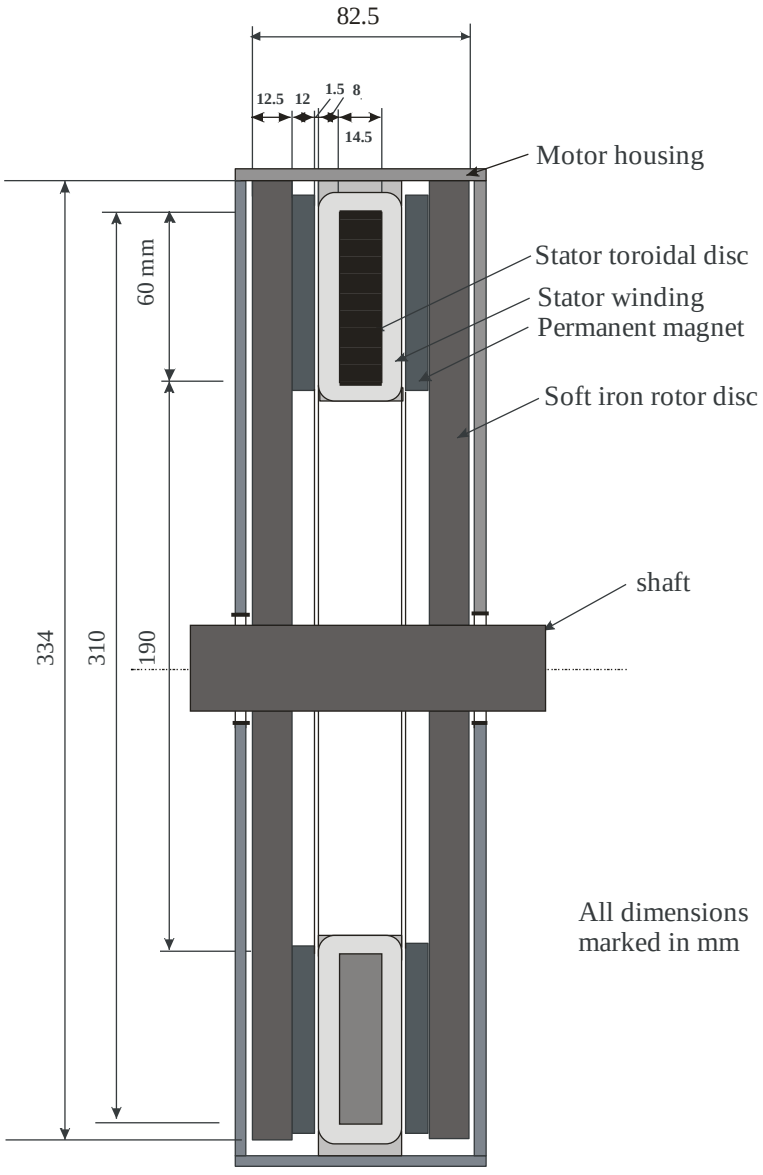

Fig. 6.1. Dimensions and structure of AFTR PMBL motor

Table 6.1. Design data of twin-rotor AFPM motor

STATOR:	
Stator structure	Internal, slot-less
Stator outer diameter (mm)	310
Stator inner diameter (mm)	190
Stator thickness (mm)	14.5
Permissible flux density in stator disc (T)	1.4
Stator core	Steel 1008
WINDING:	
Number of phases	3
Number of coils	48
Number of parallel winding paths	2
Number of coils per phase per pole	1
Cross-section area of coil (mm^2)	88
Turn number per coil	17
Wire diameter (mm)	2.0523 (AWG 12)
Wire cross-section area (mm^2)	3.308
Winding filling factor, k_{Cu}	0.61
Current Density (A/mm^2)	41.2
Rated Current (A)	21.33
Current Loading (A.turns/mm)	41.5
ROTOR:	
Rotor configuration	External twin-rotor with surface mounted NdFe magnets
Rotor diameter (mm)	334
Rotor thickness (mm)	12.5
Permissible flux density in rotor disc (T)	1.2
Rotor Speed (rpm)	936
Rotor core	Iron

MAGNET:	
Number of PM poles	16
Magnet Grade	NdFe30
μ	1.045
H_c (kA/m)	838
B_r (T)	1.1
Magnet thickness (mm)	12
Magnetic flux density in air gap (T)	0.7
OTHER PARAMETERS:	
Length of air-gap (mm)	1.5
Motor length (mm)	82.5

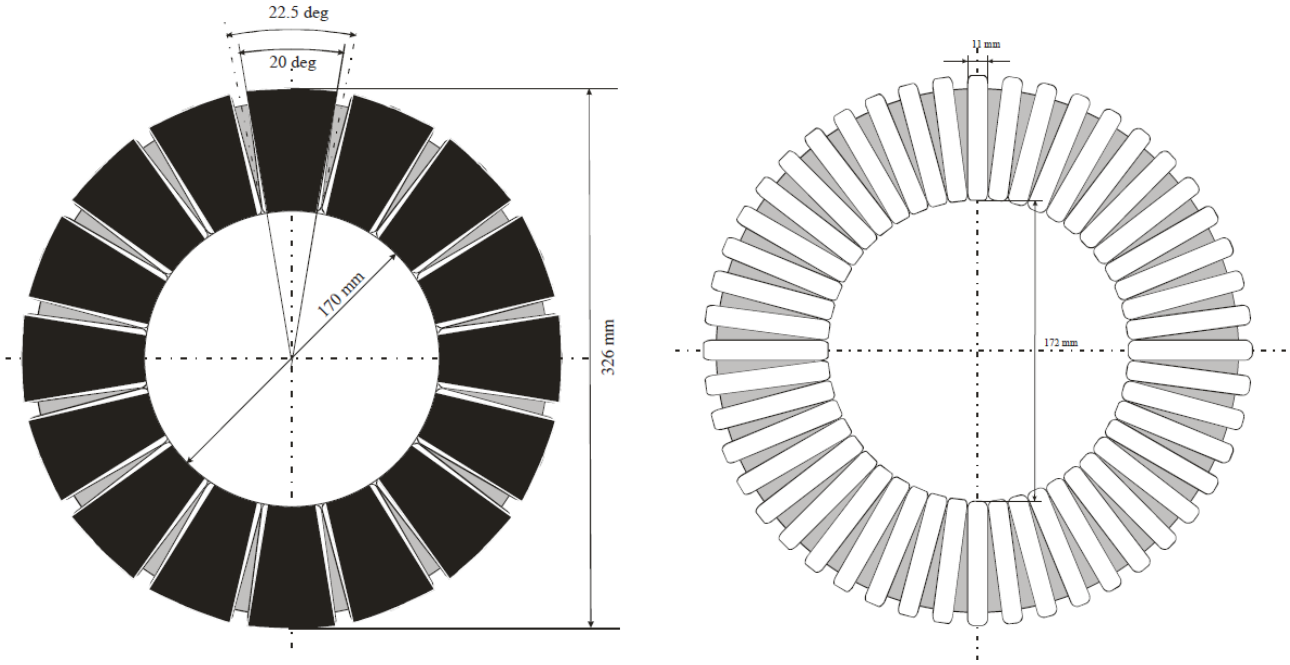

Fig. 6.2. AFTR PM motor: (a) Surface mounted PMs, (b) Three-phase armature winding

The objective of this chapter is to obtain the torque output of the AFTR PMBL motor, by Finite Element Modeling and analysis, so that the result can be used to validate the proposed

ECM. For this purpose, Maxwell 13, a three-dimensional FEM package from Ansoft is used. This is discussed in detail in Subsection 6.2.

The motor is supplied by a rated current of 21.33 A through three-phase armature windings displaced in space by 120 degrees. The distribution of the rotor magnets and armature windings is shown in Fig. 6.2. The winding configuration for twin-rotor motors, both axial flux and radial flux can be seen in Fig. 6.3.

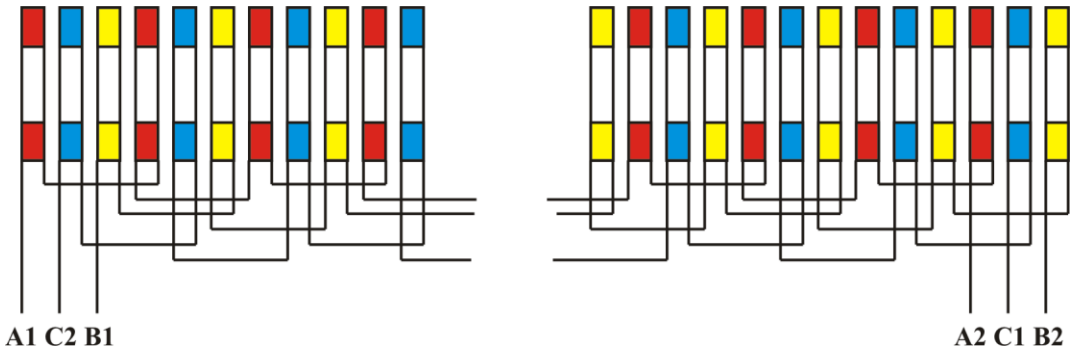

Fig. 6.3. Three phase winding configuration for the twin-rotor motors

6.2 Finite Element Modeling of Motor

As discussed in Chapter 2, the dimensions of a disc motor change with radius and the torque is produced over a continuum of radius. To accurately represent this phenomenon, 3D modeling is required, although a 2D model may be used for the preliminary assessment of motor magnetic flux distribution and performance [46]. Such a 2D model could be produced by cutting it through the PMs and windings and unfolding this cross-section. A partial section of one-half of the 2D model of the twin rotor AFPM motor built in FEMM 4.2 software [47] is shown in Fig. 6.4. This model can be used to optimize the thickness of rotor disc and stator core, so that the desired magnetic flux density is obtained in them. This is mostly an iterative process (trial and error method) until the required flux densities are achieved. Since the optimization is an iterative

procedure, modeling in 2D and not in 3D saves time and labor. The axial length of the AFTR PMBL motor is determined as a result of this 2D modeling [46]. Once the optimized dimensions are obtained and the axial length is determined, the motor is modeled in 3D space.

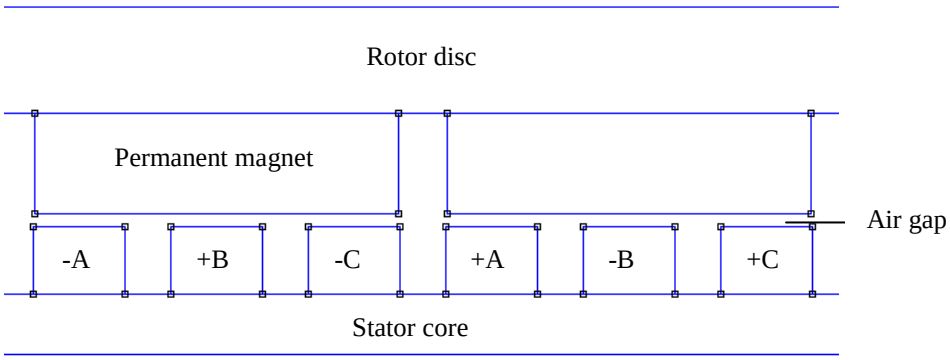

Fig. 6.4. 2D modeling of a section of the AFTR PMBL motor with slot-less stator using FEMM 4.2 [47]

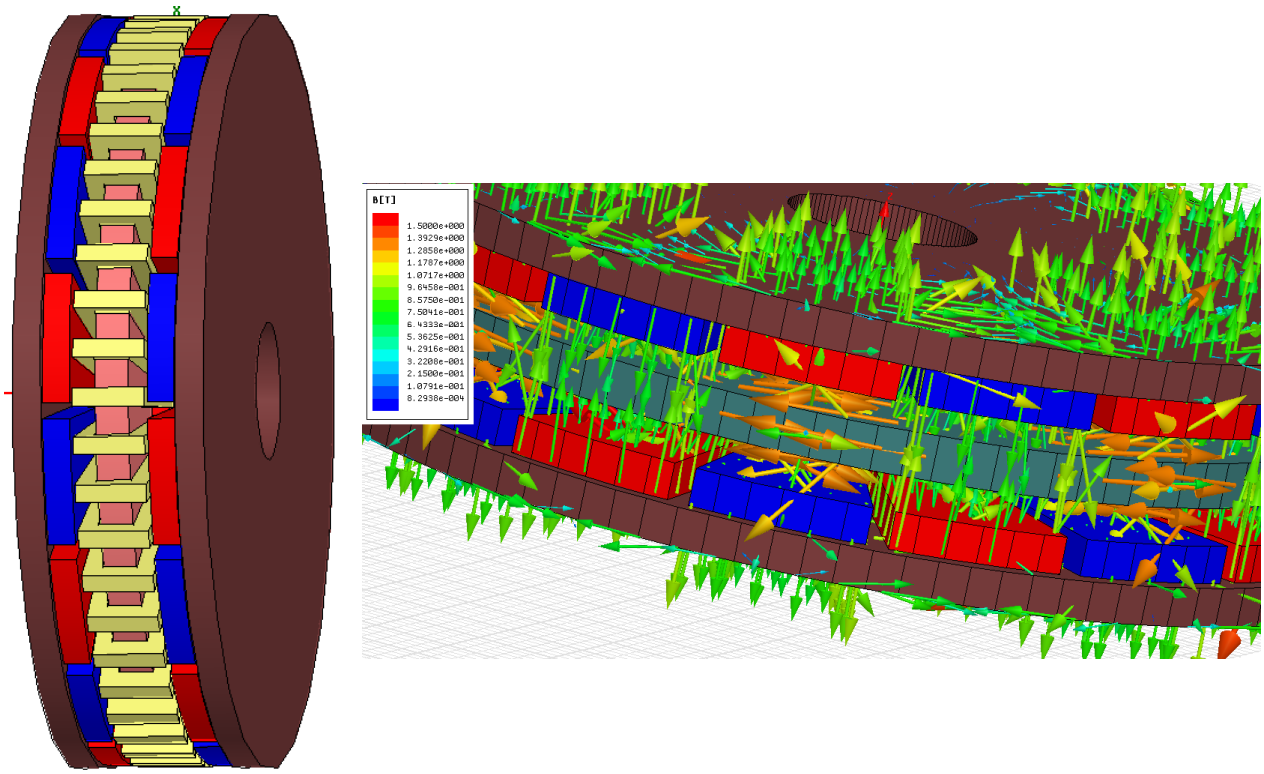

(a) **(b)**

Fig. 6.5. (a) 3-dimensional FEM model of torus motor built in Maxwell, (b) Direction of magnetic flux in rotor and stator cores

A 3-dimensional model of AFTR PMBL motor built in Maxwell software [48] can be seen in Fig. 6.5 (a). The axial length, rotor and stator core thicknesses determined from 2D modeling are used to build the 3D model. Although the computation complexity increases in three-dimensional space, the accuracy of analysis is more precise than that carried out in two-dimensional space. Fig. 6.5 (b) shows the magnetic flux direction in the motor. As the name suggests, the flux lines are parallel to the motor shaft.

Fig. 6.6 gives the magnetic flux density plot of the AFTR PMBL motor. The maximum flux density in the rotor core is about 1.2 T and that in the stator core is about 1.4 T.

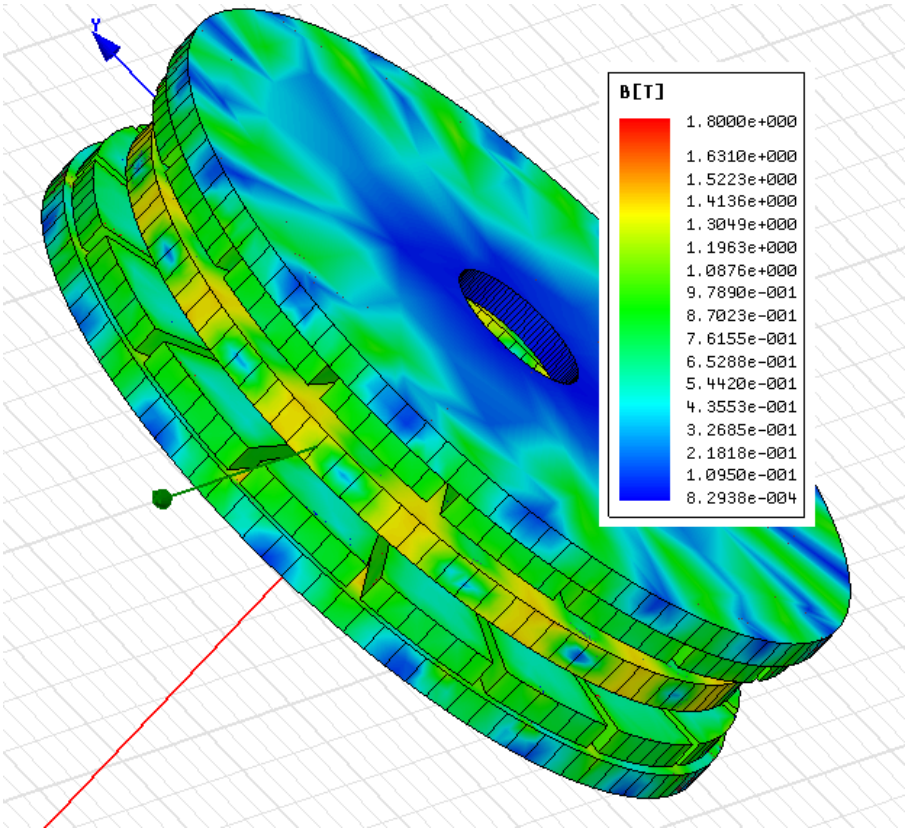

Fig. 6.6. Magnetic flux density distribution in AFTR PMBL motor

The normal component of magnetic flux density, over two pole pitches, is shown in Fig. 6.7 and it can be seen that the average flux density in the air-gap is approximately 0.7 T.

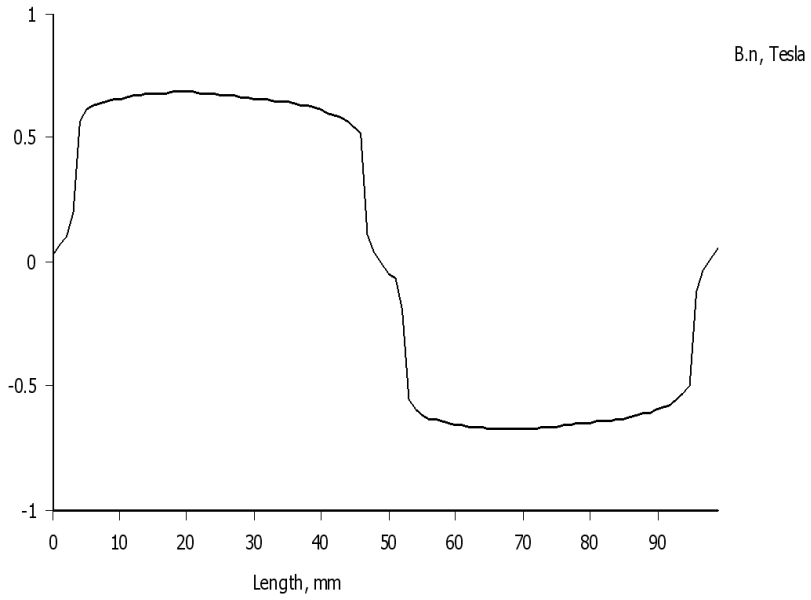

Fig. 6.7. Air-gap magnetic flux density distribution

The assignment of current vectors in the three phases of stator winding is shown in Fig. 6.8. To determine the maximum torque output of AFTR PMBL motor, phase A is supplied with a rated current of 21.33 A whereas phases B and C are each supplied with a current of -10.66 A.

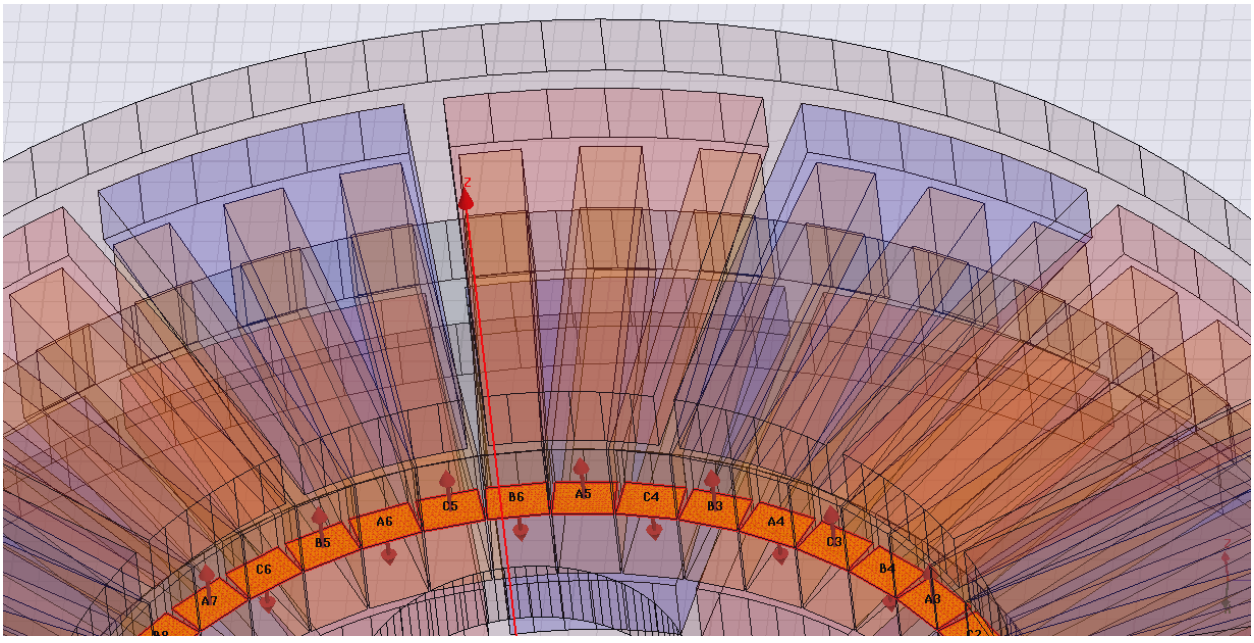

Fig. 6.8. Current vectors in the three-phase stator winding

The electromagnetic torque output of the motor is determined by changing the phase currents in accordance with the rotor angle, using the following relations:

$$i_A = I_{max} \cos \theta_e \tag{6.1}$$

$$i_B = I_{max} \cos\ (\theta_e + 120^0) \tag{6.2}$$

$$i_C = I_{max} \cos\ (\theta_e - 120^0) \tag{6.3}$$

where θ_e is the electrical angle and is related with the mechanical angle by the relation:

$$\theta_m = \frac{\theta_e}{(P/_2)} \tag{6.4}$$

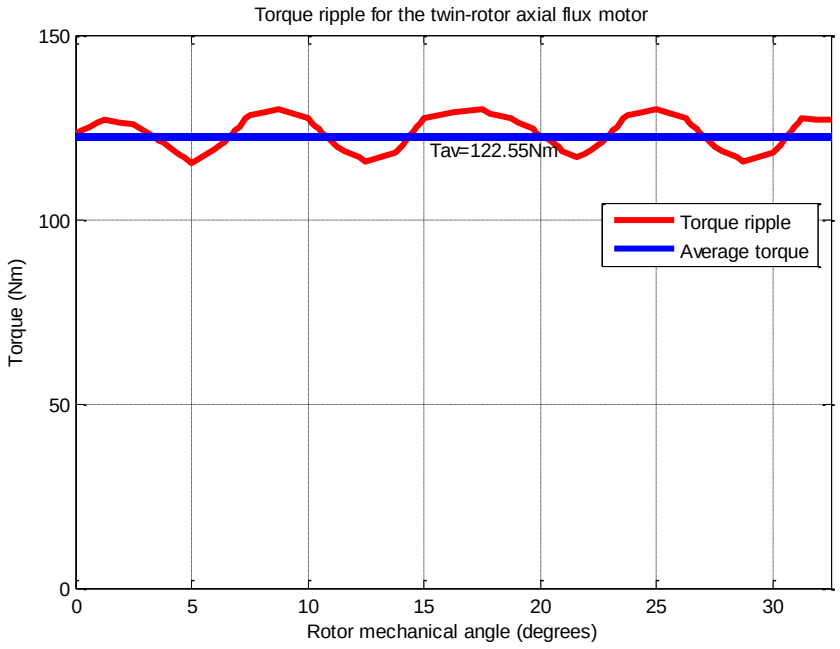

Fig. 6.9. Torque response of AFTR PMBL motor

Thus, parametric analysis is carried out in Maxwell to determine the torque at each step by simultaneously changing the phase currents and rotating the rotor over six coil pitches. The torque response of the AFTR PMBL motor obtained in such a way is plotted with respect to the

rotor mechanical angle, as shown in Fig. 6.9. As seen from this figure, the average torque output of the twin-rotor axial flux motor is 122.6 Nm. The maximum torque is obtained when the angle between the stator current vector and rotor flux is 90°. This value as read from Fig. 6.9 is 129.7 Nm. The minimum torque obtained is 115.4 Nm. The torque ripple can be calculated using the relation in (2.26):

$$T_r = \frac{T_{max} - T_{min}}{T_{av}} \times 100 = 12\ \%$$

One of the factors influencing the torque ripple is the shape of permanent magnets [6]. In this case, the AFTR PMBL motor uses trapezoidal PM poles which can be cited as one of the reasons contributing to the above torque ripple. The ripple might be reduced slightly by the use of rectangular pole pieces.

6.3 Validation of ECM

The primary purpose of FEM modeling of AFTR PMBL motor is to compare the torque output from FEM with the torque value computed using ECM. The electromagnetic torque obtained from ECM for an AFTR PMBL motor of diameter 334 mm and axial length 82.5 mm, for a magnetic loading of 0.7 T and electric loading of 41.5 A-turns/mm with winding coefficient of 1.0 can be referred from Chapter 5 as 127.2 Nm. The average electromagnetic torque obtained from FEM analysis of the AFTR PMBL motor with the same dimensions and parameters is 122.6 Nm. Both the ECM and FEM results are for AFTR PMBL motor with radius ratio ($k_{i/o}$ = 95/155) taken as 0.613.

Thus, the error of proposed ECM for AFTR PMBL motor is 3.8 %.

CHAPTER 7: TWIN-ROTOR RF PM MOTOR: MODELING AND ANALYSIS

7.1 Motor Data

The twin-rotor cylindrical motor with a slot-less stator, which is the subject of this chapter, is still considered a novel structure as it is rarely found in literature. Both the inner and outer rotors have surface mounted permanent magnets with magnets on the outside and inside rotor surfaces respectively, as shown in Fig. 7.1.

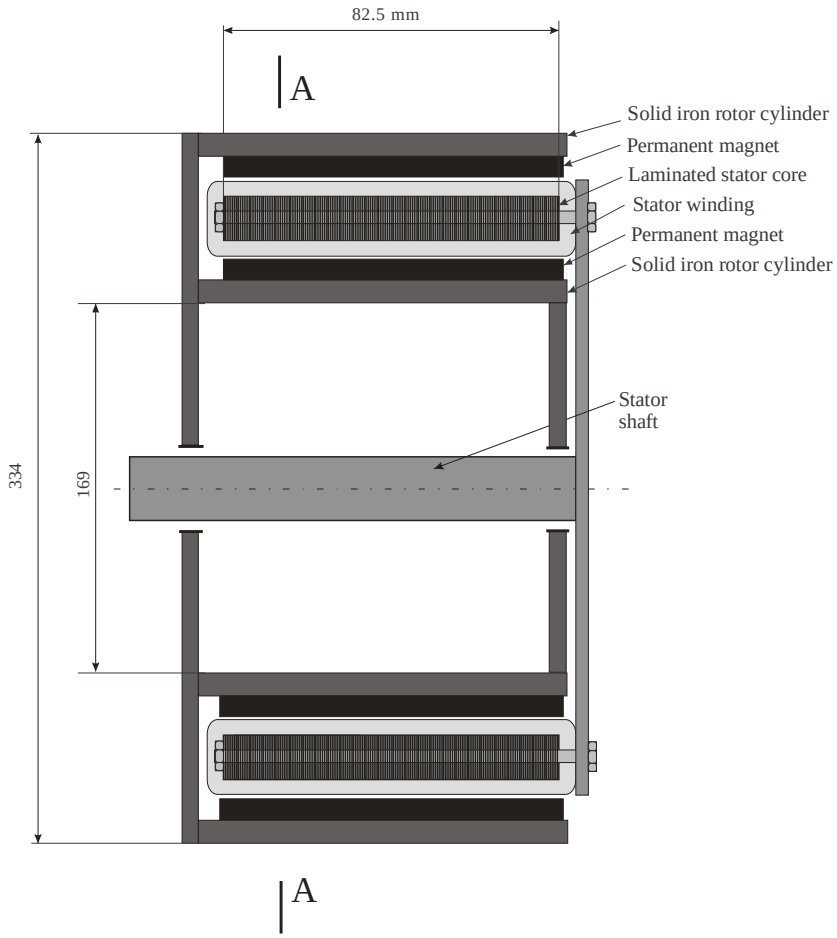

Fig. 7.1. Topology of a twin-rotor cylindrical motor with slot-less stator

Since ECM assumes that the motors under comparison have the same outer diameter and axial length, these dimensions for the RFTR PMBL motor are the same as that of the AFTR

PMBL motor. A cross-sectional view of the twin-rotor RF PM motor is shown in Fig. 7.2 with the dimensions marked.

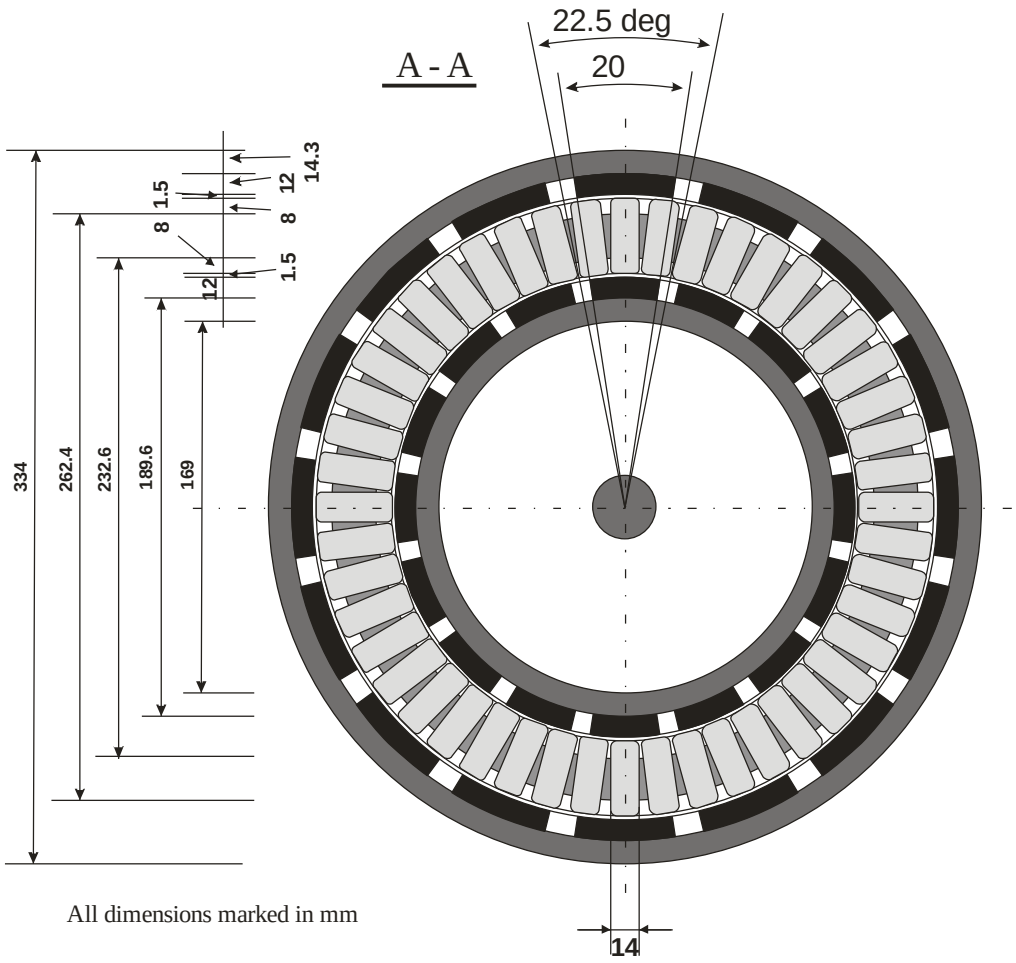

Fig. 7.2. Cross-sectional view of RFTR PMBL motor

The design data of this motor is provided in Table 7.1. The length of this machine is chosen to be equal to the thickness of the twin-rotor AFPM motor for comparison purpose. The thicknesses of the rotor and stator cores are optimized to obtain desired magnetic flux density. It should be noticed that the electrical and magnetic loading of the AFTR and RFTR PMBL motors are same. The speed of rotation of both motors is chosen to be identical too. The stator winding is provided with a rated current of 48 A.

Table 7.1. Design data of twin-rotor RFPM motor

STATOR:	
Stator structure	Internal, slot-less
Stator core	Steel 1008
Permissible flux density in stator disc (T)	1.4
Stator outside diameter/thickness (mm)	262/14.5
WINDING:	
Number of phases	3
Number of coils	48
Number of parallel winding paths	2
Number of coils per phase per pole	1
Cross-section area of coil (mm^2)	112
Turn number per coil	13
Wire diameter (mm)	2.588 (AWG 10)
Wire cross-section area (mm^2)	5.26
Winding filling factor, k_{Cu}	0.61
Current Density (A/mm^2)	4.56
Rated Current (A)	33.94
Current Loading (A.turns/mm)	41.5
ROTOR:	
Rotor Configuration	External twin-rotors with surface mounted NdFe magnets
Outer rotor outside diameter/thickness (mm)	334/15.5
Inner rotor outside diameter/thickness (mm)	190/10.15
Permissible flux density in rotor core (T)	1.2
Rotor Speed (rpm)	936
Rotor core	Iron
MAGNET:	
Number of PM poles	16

Magnet Grade	NdFe30
μ	1.045
H_c (kA/m)	838
B_r (T)	1.1
Magnet thickness (mm)	12
Magnetic flux density in air gap (T)	0.7
OTHER PARAMETERS:	
Length of air-gap (mm)	1.5
Motor length (mm)	82.5

7.2 Finite Element Modeling of Motor

To validate the proposed analytical ECM, the RFTR PMBL is modeled in three-dimensional FEM software and is analyzed to obtain the electromagnetic torque output.

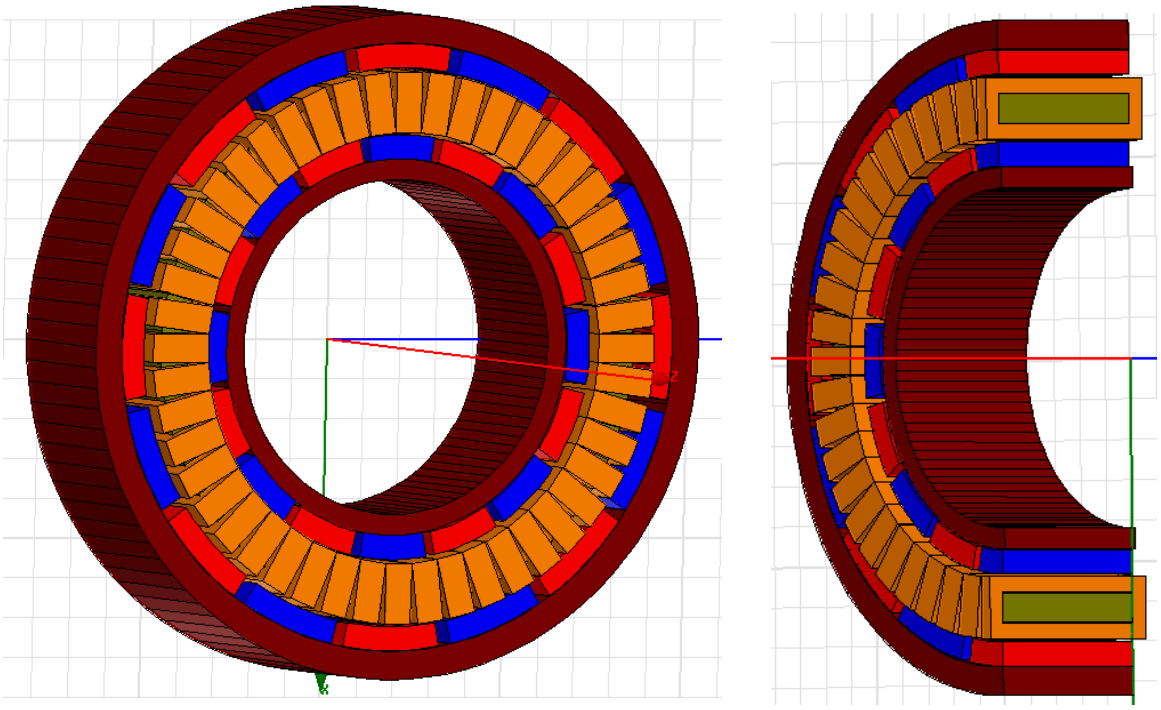

Fig. 7.3. (a) 3D model of RFTR PMBL motor built in Maxwell v13, (b) Cross-sectional view

However, before modeling in 3D space, the motor dimensions are optimized using 2D FEM to save time and labor. The rotor and stator core thicknesses are thus determined in 2D FEM and a 3D model is then built to obtain a precise analysis. Fig. 7.3 (a) shows the three-dimensional model of RFTR PMBL motor. A cross-sectional view of this motor cut in half is shown in Fig. 7.3 (b).

The direction of magnetic flux lines is shown in Fig. 7.4. The magnetic flux is directed either radially inward or outward and is perpendicular to the motor shaft.

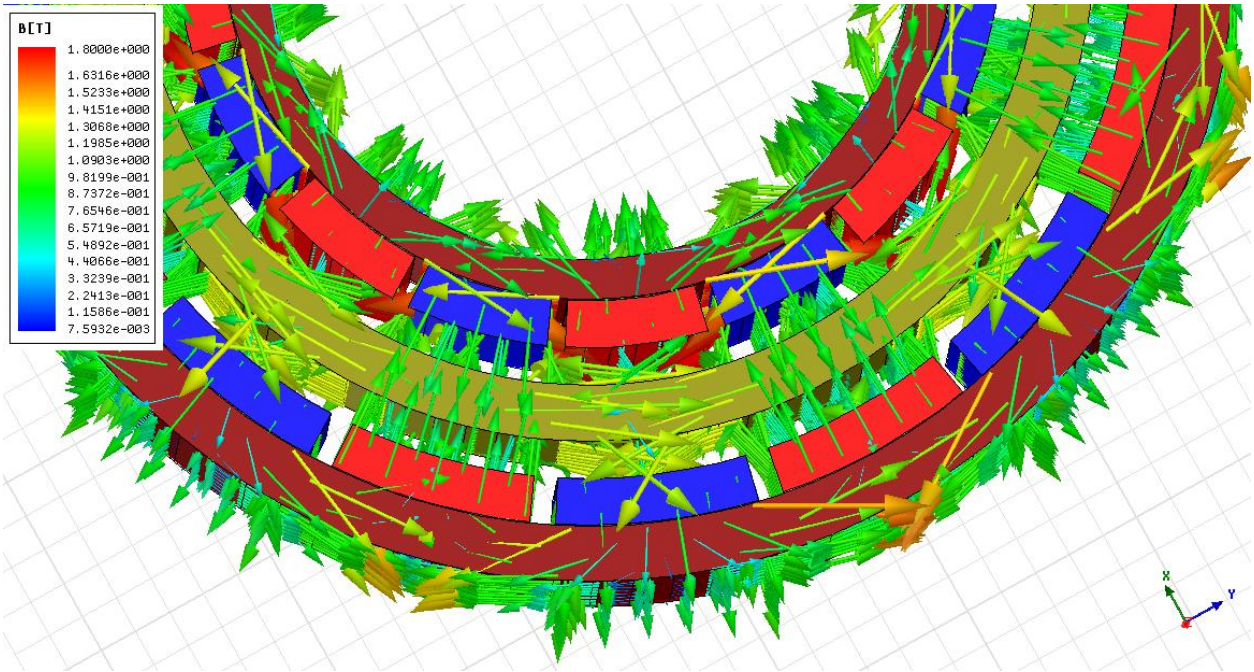

Fig. 7.4. Radial direction of magnetic flux

The flux density distribution in rotor and stator cores is shown in Fig. 7.5 (stator winding not shown in the figure). The magnetic flux density in stator is about 1.4 T while that in rotor is about 1.2 T. For comparison purpose with AFTR PMBL motor, magnetic flux density in the air-

gap of RFTR PMBL motor is maintained at 0.7 T. The air-gap flux density over two pitches is shown in Fig. 7.6.

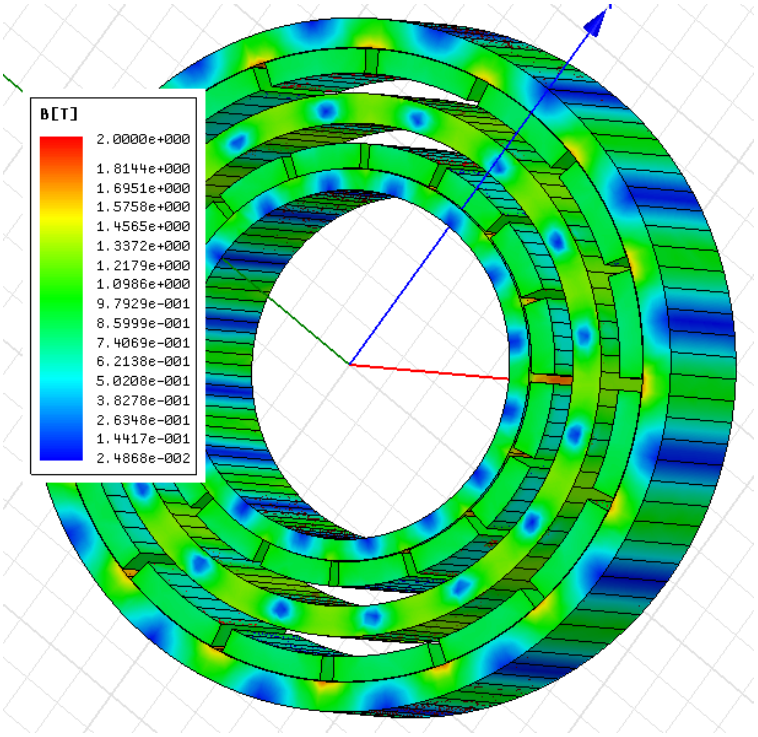

Fig. 7.5. Magnetic flux density distribution in rotor and stator cores

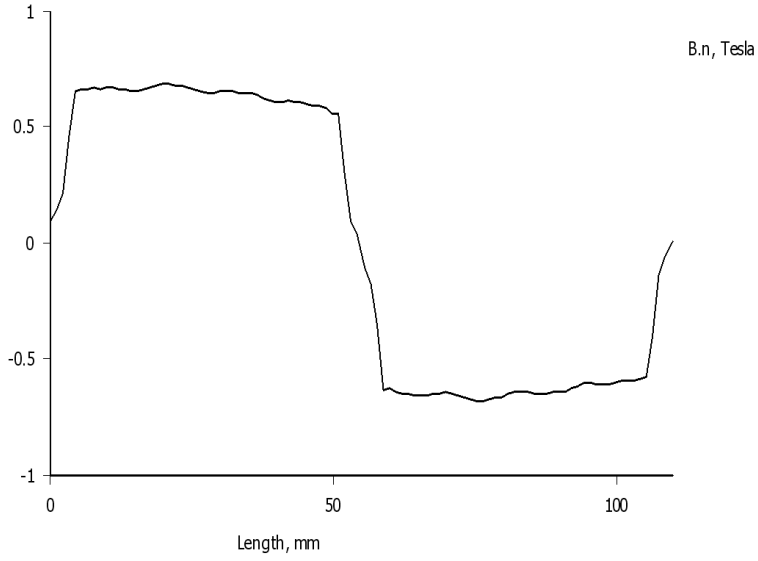

Fig. 7.6. Magnetic loading in the air-gap of RFTR PMBL motor

The stator is equipped with gramme type winding (can be seen in Fig. 7.3 (b)). The three phases are connected in Y and are supplied with a rated current of 33.94 A. The winding structure and direction of phasor currents is shown in Fig. 7.7. At the time instant shown in this figure, the PM flux is displaced from stator current by 90° and maximum torque is obtained when phase A is supplied by 33.94 A and phases B and C are supplied by -16.97 A.

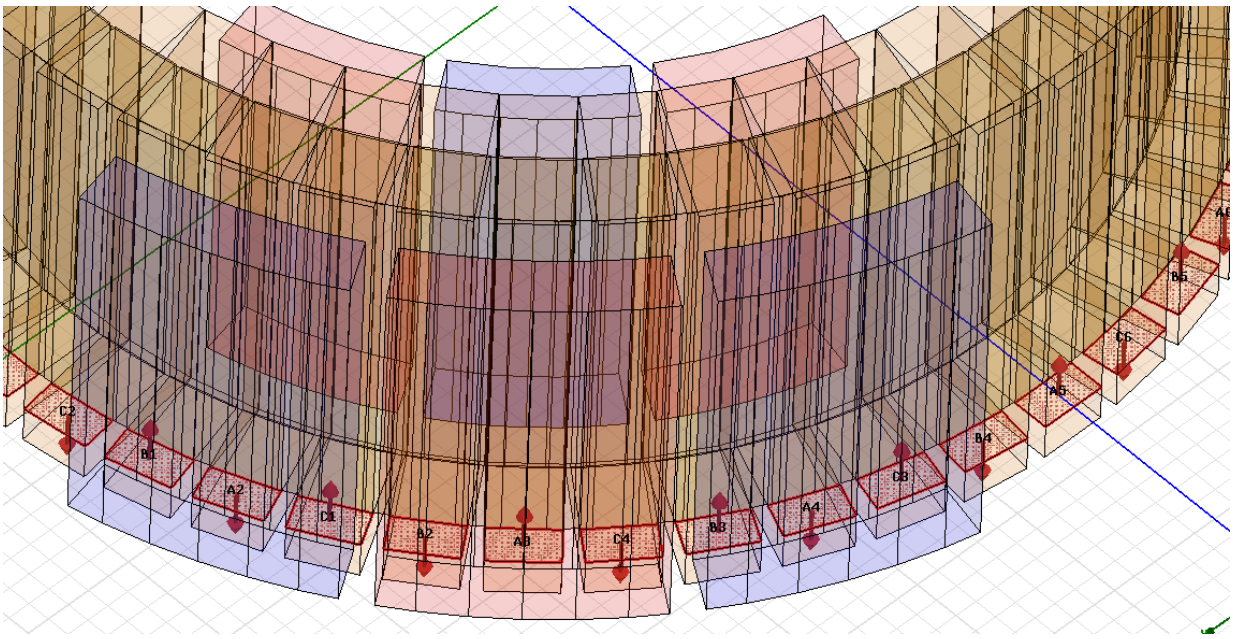

Fig. 7.7. Three-phase currents in gramme type stator winding

The electromagnetic torque of RFTR PMBL motor is determined in the same way as stated in the previous chapter (Section 6.2) by means of parametric analysis changing the three-phase currents and rotor position simultaneously. Thus, the average torque obtained is 179 Nm. The maximum torque output of the twin-rotor radial flux motor is 183.2 Nm and the minimum torque value is 174.8 Nm. The torque response of this motor as a function of rotor mechanical angle is shown in Fig. 7.8.

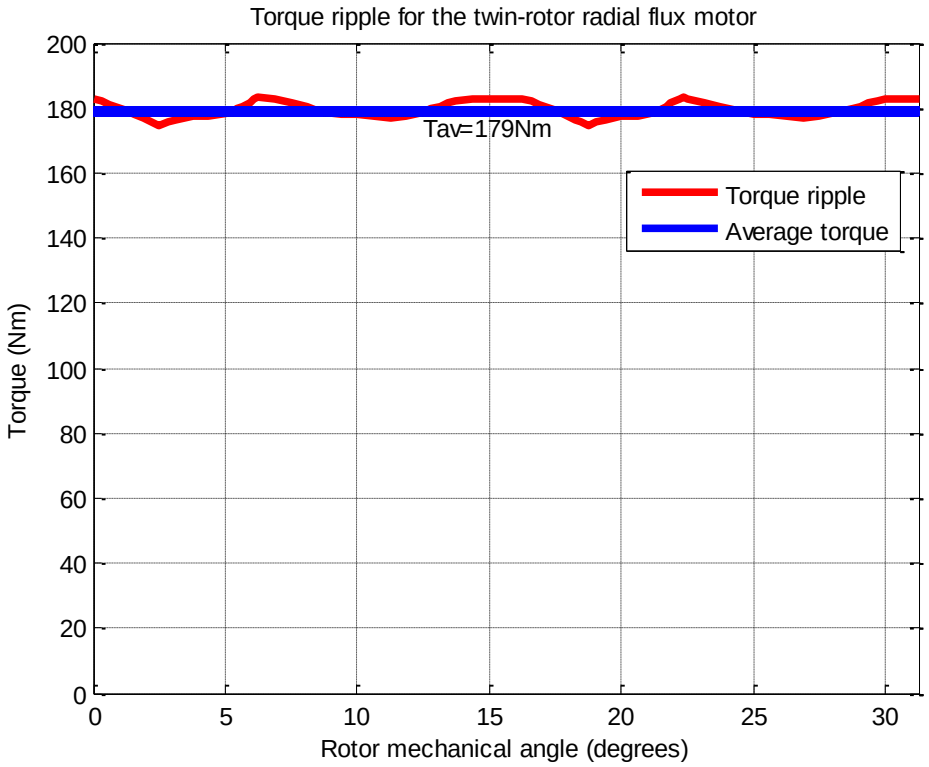

Fig. 7.8. Electromagnetic torque output of RFTR PMBL motor

The torque ripple of RFTR PMBL motor can be calculated as follows:

$$T_r = \frac{T_{max} - T_{min}}{T_{av}} \times 100 = 5\ \%$$

This torque ripple is much lower when compared to that of the AFTR PMBL motor, calculated as 0.12 Nm in previous chapter. The RFTR PMBL motor uses rectangular pole pieces unlike the trapezoidal shaped poles of AFTR PMBL motor. This might be one of the reasons influencing torque ripple.

7.3 Validation of ECM

From the FEM simulation results in Maxwell, the average torque obtained for RFTR PMBL motor is 179 Nm for an outer diameter of 334 mm and axial length of 82.5 mm with a

magnetic loading of 0.7 T and current loading of 41.5 A.turns/mm for a winding coefficient of 1.0. For the same motor, the torque value obtained from ECM is 181.2 Nm (referring to the result on page 64). Thus the error in ECM for RFTR PMBL motor is 1.2%.

Since we already have the FEM results for both AFTR and RFTR PMBL motors, we can also calculate the torque ratio and compare it with the value obtained from ECM. According to FEM simulation results from Maxwell, the ratio of torques obtained from AFTR PMBL motor to RFTR PMBL motor is:

$$T_{a/r(FEM)} = 122.6/179 = 0.69 \tag{7.1}$$

Referring to page 68, the torque ratio obtained from ECM for these two motors is 0.7.

$$T_{a/r(ECM)} = 0.7 \tag{7.2}$$

From (7.1) and (7.2), the error in computing the torque ratio of AFTR PMBL motor to RFTR PMBL motor using ECM is 1.5%.

CHAPTER 8: SINGLE ROTOR SLOT-LESS RF PM MOTOR: MODELING AND ANALYSIS

8.1 Motor Data

The third motor in the comparative study of this dissertation is a single rotor cylindrical motor with a slot-less stator. The schematic of this motor is shown in Fig. 8.1 with the dimensions marked.

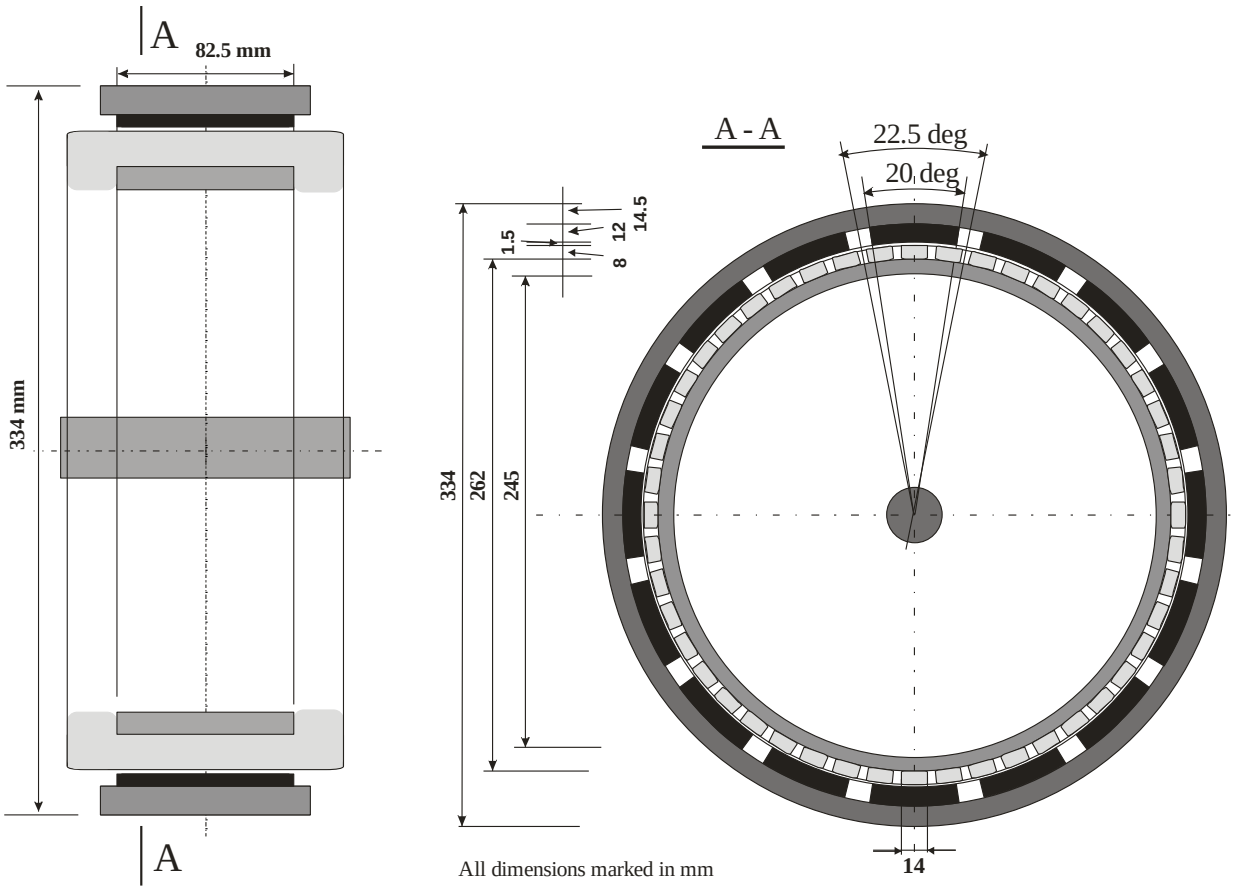

Fig. 8.1. Schematic of single rotor RF PMBL motor with slot-less stator

It should be noticed that the outer diameter and axial length of this motor is the same as that of the twin-rotor motors in the previous chapters. However, the thickness of the single-rotor motor is about half that of the twin-rotor motors, which is already accounted for in the derivation

of electromagnetic torque expression by ECM. The other electromagnetic parameters like electric loading, magnetic loading and the winding coefficient are maintained the same as that of twin-rotor motors. The design parameters of this motor can be read from Table 8.1.

Table 8.1. Design data of single-rotor RFPM motor

STATOR:	
Stator structure	Internal, slot-less
Stator core	Steel 1008
Permissible flux density in stator disc (T)	1.2
Stator outside diameter/thickness (mm)	262/8.5
WINDING:	
Number of phases	3
Number of coils	48
Number of parallel winding paths	2
Number of coils per phase per pole	1
Cross-section area of coil (mm^2)	112
Turn number per coil	15
Wire diameter (mm)	3.264 (AWG 8)
Wire cross-section area (mm^2)	8.36
Winding filling factor, k_{Cu}	0.61
Current Density (A/mm^2)	4.56
Rated Current (A)	33.94
Current Loading (A.turns/mm)	41.5
ROTOR:	
Rotor Configuration	External rotor with surface mounted NdFe magnets
Rotor outside diameter/thickness (mm)	334/14.5
Permissible flux density in rotor core (T)	1.4
Rotor Speed (rpm)	936

Rotor core	Iron
MAGNET:	
Number of PM poles	16
Magnet Grade	NdFeB 40
μ	1.049
H_c (kA/m)	979
B_r (T)	1.29
Magnet thickness (mm)	12
Magnetic flux density in air gap (T)	0.7
OTHER PARAMETERS:	
Length of air-gap (mm)	1.5
Motor length (mm)	82.5

From Fig. 8.1, it can be observed that the single-rotor RF PMBL motor is similar in structure to the RFTR PMBL motor only with the exception that the latter has two air gaps. The finite element modeling of the single-rotor RF PMBL motor with the above design parameters is discussed in the next subsection.

8.2 Finite Element Modeling of Motor

A 3D space model of the single-rotor RF PMBL motor is built in Maxwell v13 in order to verify the results of proposed ECM. The 3D FEM model is shown in Fig. 8.2 (a). The stator with three-phase winding is shown in Fig. 8.2 (b). From the practical point of view, the single-rotor cylindrical motor model uses an overlap winding, unlike the twin-rotor motor models which employ a gramme type winding (as discussed in Chapters 6 and 7).

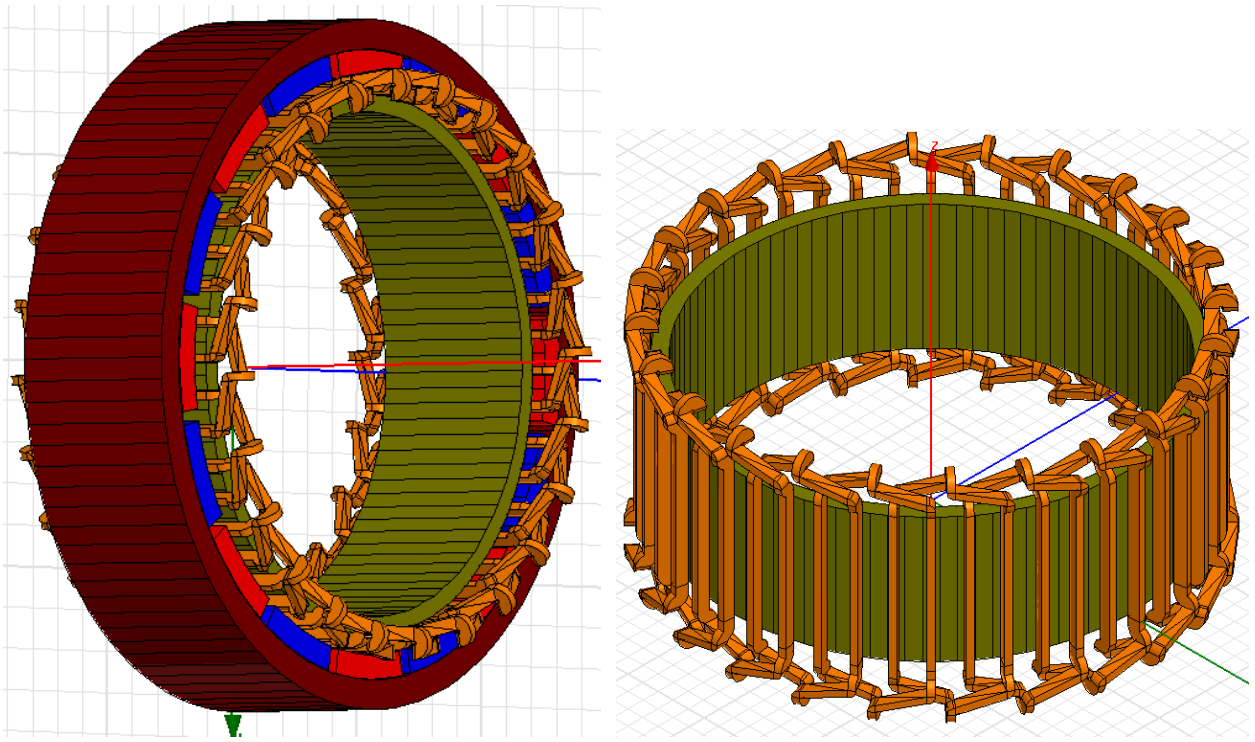

(a) **(b)**

Fig. 8.2. (a) 3D FEM model for single-rotor RF PMBL motor, (b) Stator core with overlap winding

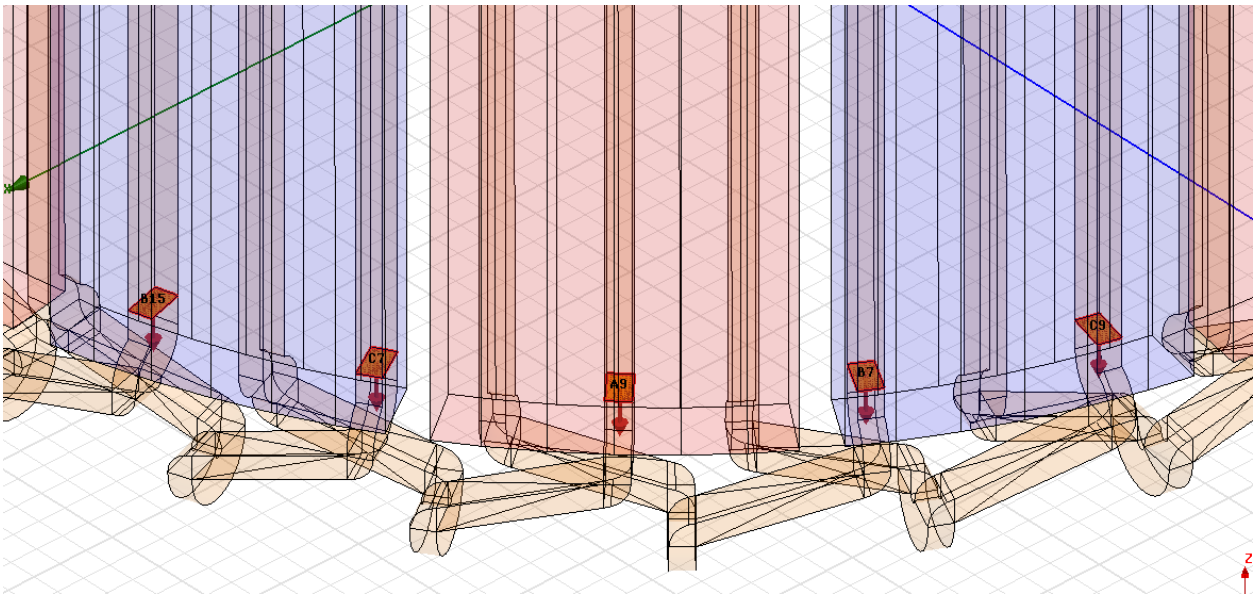

Fig. 8.3. Distribution of winding currents

The distribution of three-phase winding currents is shown in Fig. 8.3. The assignment of currents for the single-rotor RF PMBL motor looks different than that of the AFTR and RFTR PMBL motors. This is because the overlap winding used for the single-rotor RF PMBL motor is a user-defined part available in Maxwell 13 library, and the return path of each phase current need not be assigned. However, the gramme winding for twin-rotor motors is not available in Maxwell 13 library and is created manually, which is the reason the return path for phase currents had to be assigned, also manually.

The rated current for single-rotor cylindrical motor is 33.94 A, the same as that of the twin-rotor cylindrical motor. However, the number of turns of coil for the single-rotor motor (15 turns) is slightly higher than that of the twin-rotor motor (13 turns) to maintain the same electrical loading. To recollect, ECM assumes that electrical loading on the inner radius (of stator coils) of twin-rotor motor is equal to the electrical loading on rotor coils of single-rotor motor.

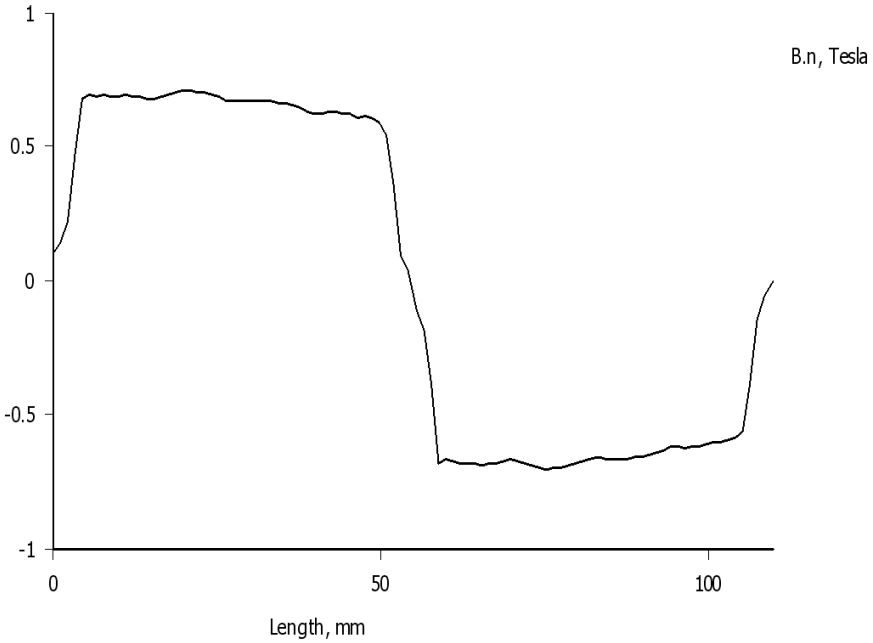

Fig. 8.4. Air gap flux density distribution

The magnetic flux density in the air gap is 0.7 T, as seen in Fig. 8.4. The direction of magnetic flux lines and the flux density distribution in rotor and stator cores is shown in Fig. 8.5. As in the case of RFTR PMBL motor, the direction of magnetic flux in the single-rotor RF PMBL motor is perpendicular to the motor shaft. The average flux density in the stator is about 1.3 T and in the rotor is about 1.4 T.

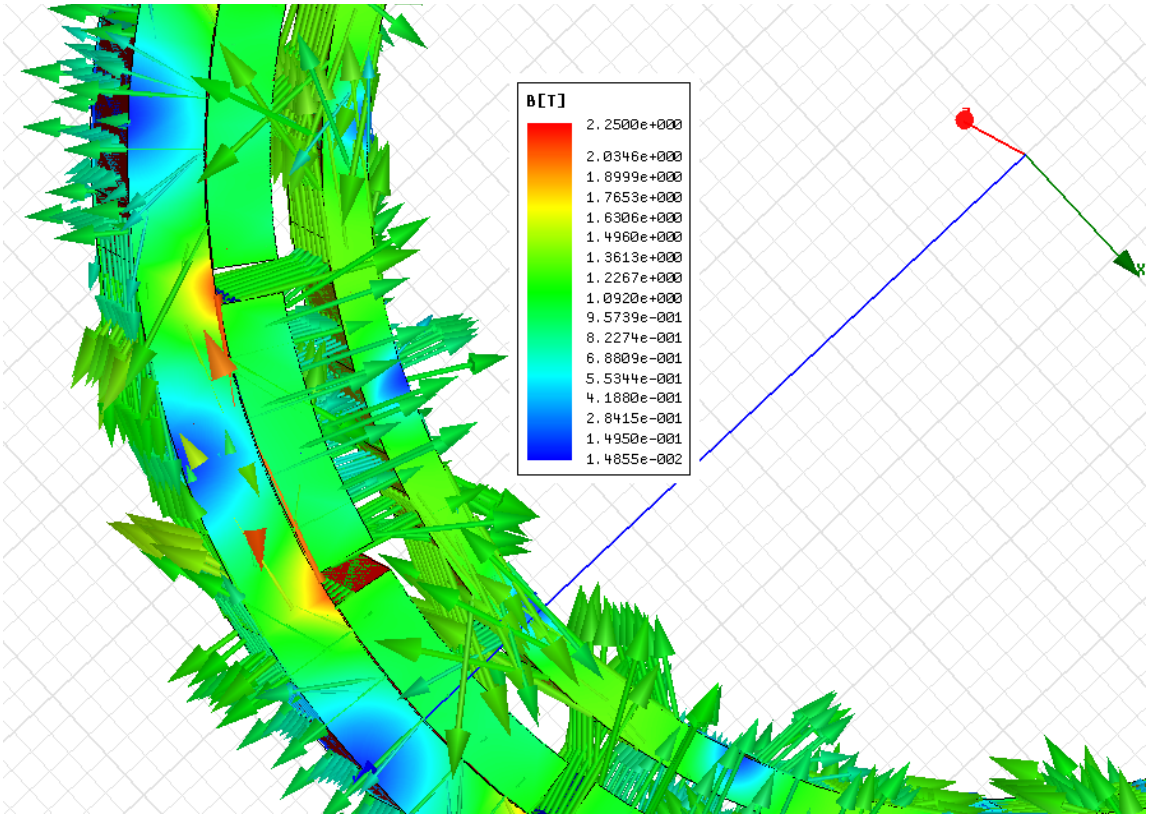

Fig. 8.5. Magnetic flux direction and density distribution in single-rotor RF PMBL motor

The same approach as AFTR and RFTR PMBL motors is followed to determine the torque response of the single-rotor RF PMBL motor. The torque plot as a function of rotor mechanical angle is obtained by parametric analysis. This torque plot is shown in Fig. 8.6. It can be seen that the average torque obtained from the single-rotor cylindrical PMBL motor is 150.8 Nm. The maximum torque output is about 157.1 Nm and the minimum torque is 144.6 Nm.

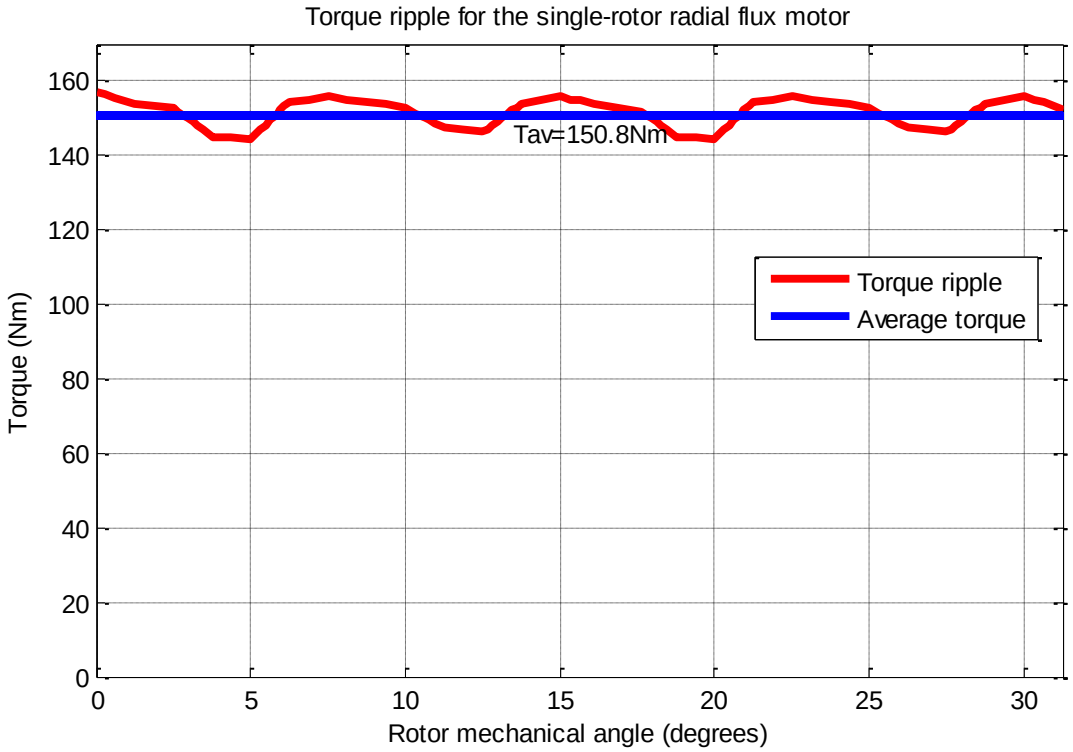

Fig. 8.6. Torque response of single-rotor RF PMBL motor with slot-less stator

Thus, the torque ripple can be calculated as:

$$T_r = \frac{T_{max} - T_{min}}{T_{av}} \times 100 = 8\ \%$$

The torque ripples of all the three motors, as obtained from 3D FEM are tabulated in Table 8.2. It can be concluded that the RFTR PMBL motor provided the most smooth torque response, followed by single-rotor RF PMBL motor and AFTR PMBL motor. In other words, the AFTR PMBL motor yielded the biggest torque ripple of the three motors.

Table 8.2. Torque ripple obtained from Maxwell 13

	Single-rotor RF motor	**RFTR motor**	**AFTR motor**
Torque ripple (%)	8	5	12

Using the results for AFTR and RFTR PMBL motors, the torque ratios with respect to single-rotor RF PMBL motor are determined and the ECM is verified, which is discussed in the following subsection.

8.3 Validation of ECM

The average torque obtained for a single-rotor RF PMBL motor of diameter 334 mm, axial length 82.5 mm, electrical loading 41.5 A.turns/mm and magnetic loading 0.7 T is 150.8 Nm in 3D Maxwell 13 based on finite element magnetics. The torque obtained for the same motor using ECM is 164.2 Nm (refer Table 5.1). Thus the error in computation of torque using ECM for a single-rotor RF PMBL motor is 8.9%.

From Table 5.2 in Chapter 5, the torque ratio of single-rotor RF PMBL motor to AFTR PMBL motor from ECM is 1.29.

$$T_{rs/a(ECM)} = 1.29$$

From Maxwell v12 results, the above torque ratio is calculated as:

$$T_{rs/a(FEM)} = 150.8/122.6 = 1.23$$

Thus, the error in computing torque ratio, $T_{rs/a}$ is 4.9%.

Similarly, the torque ratio of RFTR PMBL motor to single-rotor RF PMBL motor using ECM can be referred from Table 5.2 as 1.1.

$$T_{r/rs(ECM)} = 1.1$$

This torque ratio from 3D FEM can be calculated as:

$$T_{r/rs(FEM)} = 179/150.8 = 1.19$$

Therefore, the error in computing torque ratio, $T_{r/rs}$ using ECM is -7.6%.

It should be noted that the ECM ignores end winding connection lengths, however, the simulation result in 3D FEM includes the end winding connections of the overlap winding on stator core.

CHAPTER 9: PROTOTYPE OF WHEELCHAIR MOTOR

In this chapter, the software Maxwell v12 (used to model the AFTR, RFTR and single-rotor RF PMBL motors in Chapters 6, 7 and 8 and verify the proposed ECM) is validated using a prototype motor that was designed and fabricated for an electric wheelchair application.

9.1 Motor Data

A conventional single-rotor cylindrical (or radial flux) motor with slotted stator is designed for the gearless in-wheel motor drive of an electric wheelchair. The scheme of such a motor with outer rotor and surface mounted PMs is shown in Fig. 9.1.

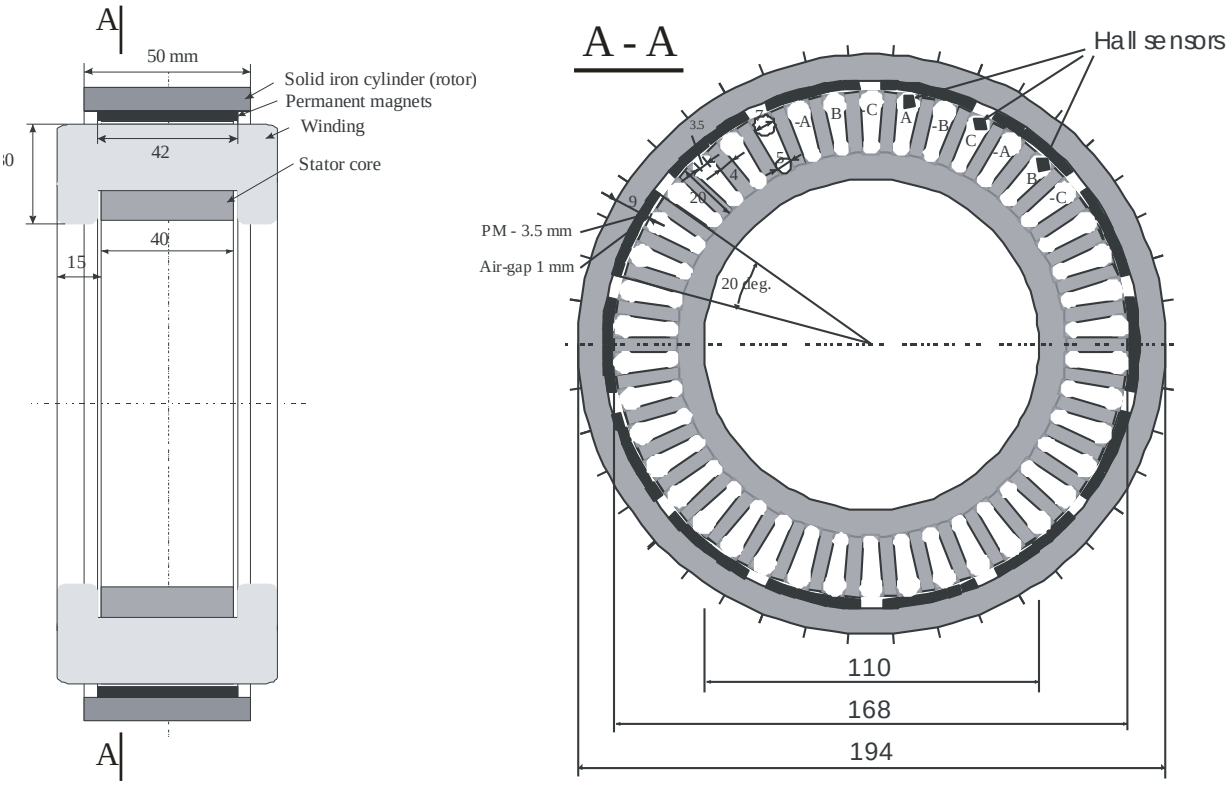

(a) **(b)**

Fig. 9.1. Scheme of conventional single-sided outer-rotor RFPM motor: (a) longitudinal cross-sectional view, (b) transverse cross-sectional view

A prototype was manufactured and the experimental results from this motor are used to validate the simulation results from the motor model analyzed in 3D FEM software, Maxwell v12. As seen from Fig. 9.1 (b), the outer diameter of this motor is 194 mm and the active length is 40 mm. The three-phase armature winding is located in stator slots. The rotor position is detected by Hall sensors and the winding current is switched on and off accordingly. The motor design data is given in Table 9.1.

Table 9.1. Design data of wheelchair motor

STATOR:	
Stator structure	Slotted with tooth skew of one tooth pitch
Stator core	Laminated US Steel type 2-S, 0.018 inch thickness
Number of slots/Skew angle (degrees)	42/8.57
Permissible flux density in stator disc (T)	1.6
Stator outside diameter (mm)	168
Stator inside diameter (mm)	110
WINDING:	
Number of phases	3
Number of coils per phase per pole	1
Turn number per coil	18
Wire diameter (mm)	1.8 (AWG 12)
Rated Current (A)	12
Supply Voltage (V)/Output Power (W)	24/200
ROTOR:	
Permissible flux density in rotor disc (T)	1.5
Rotor Configuration	Outer rotor with surface mounted NdFeB magnets
Rotor outer diameter/thickness (mm)	194/24
Rotor Speed (rpm)	170
Rotor core	Solid Steel 1117

MAGNET:	
Number of PM poles	14
Magnet grade	NdFeB40
μ	1.049
H_c (kA/m)	979
B_r (T)	1.29
Magnet thickness (mm)	3.5
Magnetic flux density in air gap (T)	0.9
OTHER PARAMETERS:	
Length of air-gap (mm)	1
Motor length (mm)	40

9.2 Finite Element Modeling of Motor

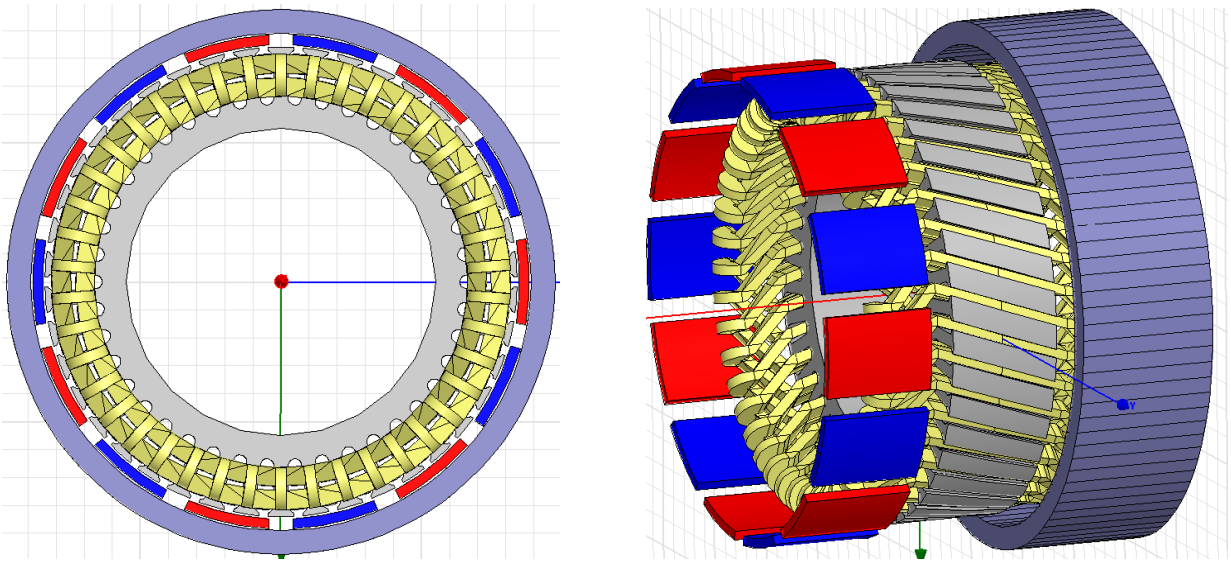

(a) **(b)**

Fig. 9.2. 3D FEM model: (a) cross-sectional view, (b) side view

The RFPM motor with the design specifications in Table 9.1 is modeled in 3D space using Maxwell v12. A cross-sectional view and side view of this motor is shown in Fig. 9.2. The stator slots are skewed by one stator slot pitch in order to reduce cogging torque. The skew angle can be noticed in Fig. 9.2 (b).

A six layer winding is employed to reduce the end winding connection length and hence the winding losses associated with it. The winding layout is shown in Fig. 9.3.

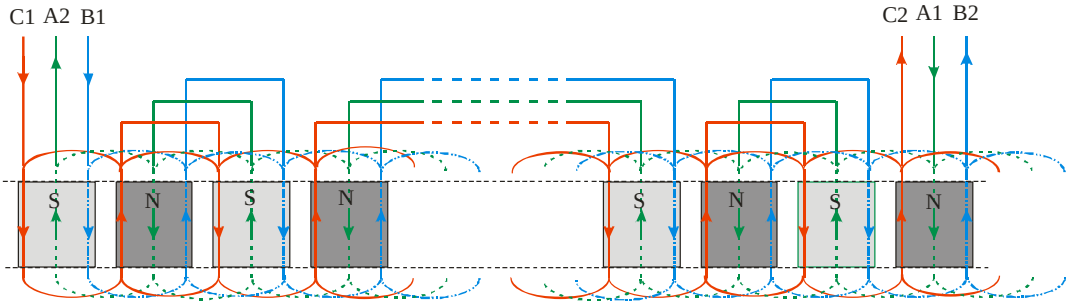

Fig. 9.3. Three-phase armature winding

The magnetic flux density plot in a section of the motor is shown in Fig. 9.4 (a).

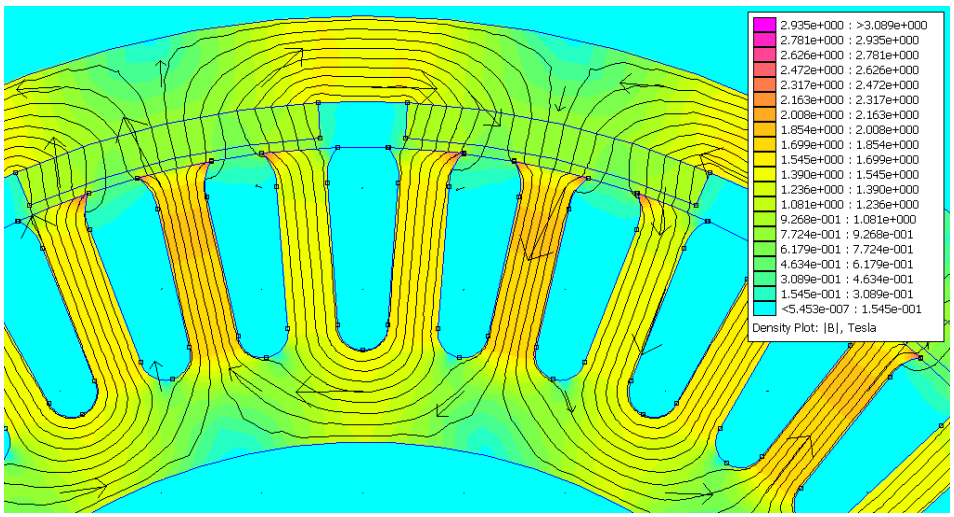

Fig. 9.4 (a). Magnetic flux density distribution in rotor and stator cores

It can be seen that the flux density is about 1.6 T in stator core and about 1.5 T in rotor back-iron. The flux density distribution in air-gap of the motor, obtained from Maxwell RMxprt is shown in Fig. 9.4 (b) and the maximum value is about 0.9 T. It should be noticed that the field density varies sharply at the two ends of the magnet. However, the field at the stator teeth which are located far from the magnet-ends is nearly constant.

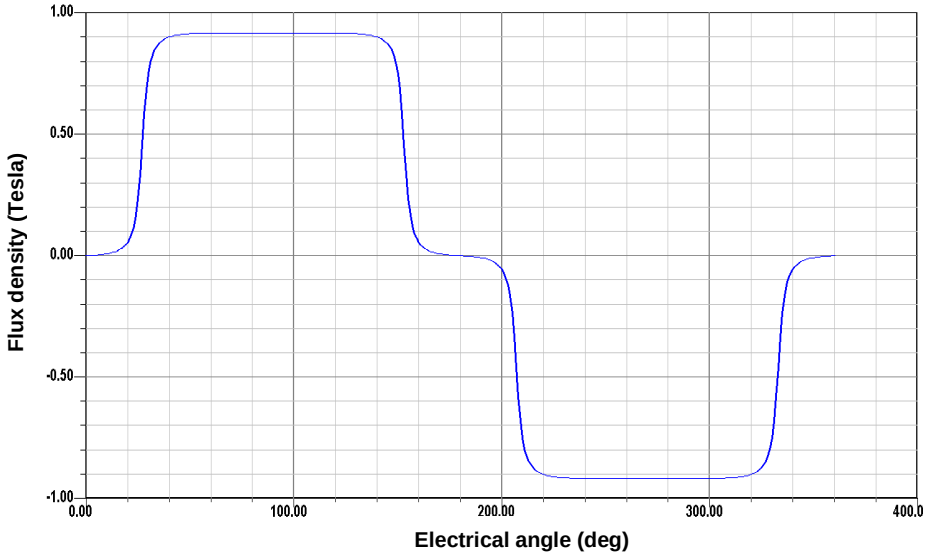

(b)

Fig. 9.4 (b). Flux density profile in the air-gap

The effect of stator skewing can be seen from the torque ripple and cogging torque plots in Figs. 9.5 and 9.6 respectively. The average torque obtained for the in-wheel motor of electric wheel chair is close to 14 Nm, by 3D FEM. Since this wheelchair application of RFPM motor demands a smooth operation, it is important to reduce the torque ripple to a minimum value. From Fig. 9.5, it can be seen that the torque ripple is reduced significantly from 8 % to 3 % with the introduction of a skew angle equal to 8.57°, which is equivalent to one full slot pitch.

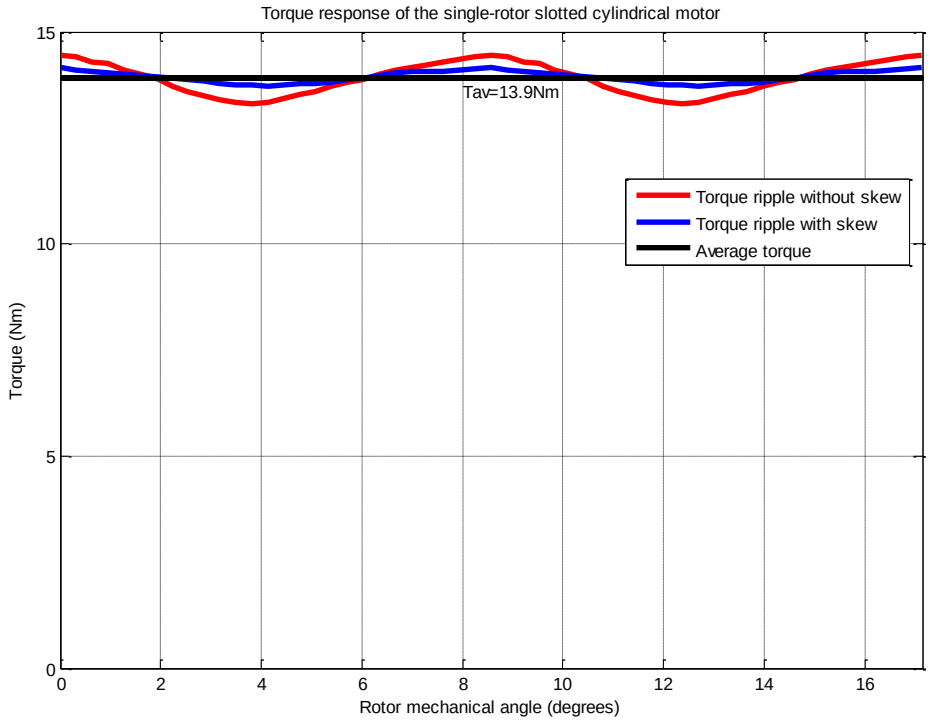

Fig. 9.5. Torque ripple and the effect of skewing

Cogging torque is one of the factors that contribute to torque ripple. As seen from Fig. 9.6, the cogging torque is reduced from 4.75 Nm to 1.5 Nm because of the stator slot skew. As a result, torque ripple of the motor is also lowered by skewing of stator slots.

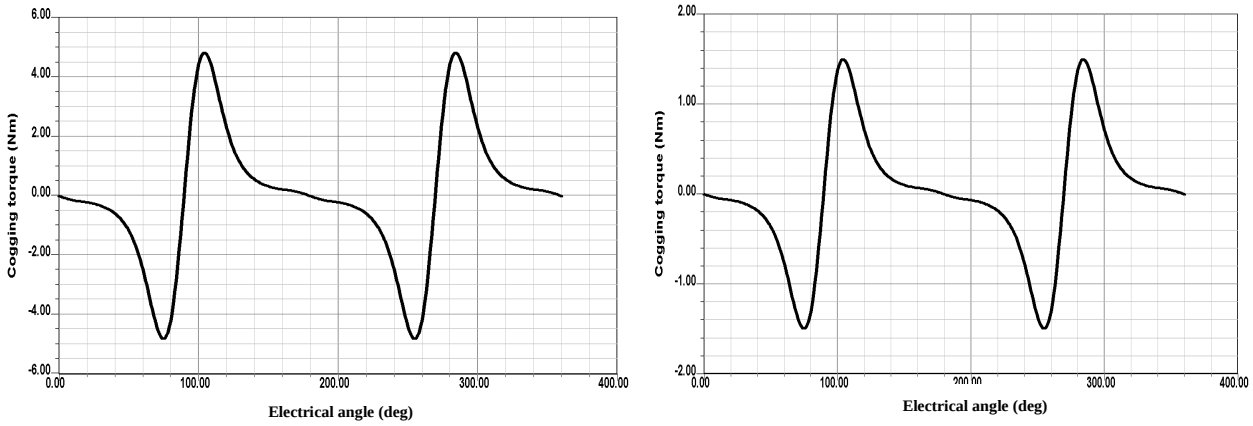

(a) **(b)**

Fig. 9.6. Cogging torque: (a) without tooth skew, (b) with tooth skew

9.3 Dynamic Analysis of the Motor in Simulink

To analyze the motor dynamics, the circuit model of three-phase motor along with supply is considered, which was presented in Chapter 2. The circuit parameters of motor winding can be calculated from the FEM model. Since the motor prototype was fabricated, see Fig. 9.8, these parameters were determined from the test. The motor parameters required for dynamic analysis are enclosed in Table 9.2.

Table 9.2. Winding parameters of the wheelchair motor

Parameter	**Value**
Phase resistance, R_a	0.188 Ω
Synchronous inductance, L_s	0.5 mH
Back emf constant, K_E	0.62 V/rad/s
Moment of inertia, J	0.01 $kg.m^2$
Friction Coefficient, B	0.04 Nm/rad/s

To model the motor, it was assumed that the inverter input voltage is constant. Under this assumption and using the winding parameters in the table above, the Simulink block diagram of the motor was developed and is shown in Fig. 9.7.

As an example, in the simulation, it was assumed that the motor starts up without any load being supplied from a DC source of 24.4 V. Then after reaching steady state, it was loaded by a torque of 8.85 Nm. The simulation results are shown in Figs. 9.8 to 9.11, in form of the following waveforms: electromagnetic torque, load torque, phase current, motor speed at the shaft, supply voltage and Electromotive Force (EMF).

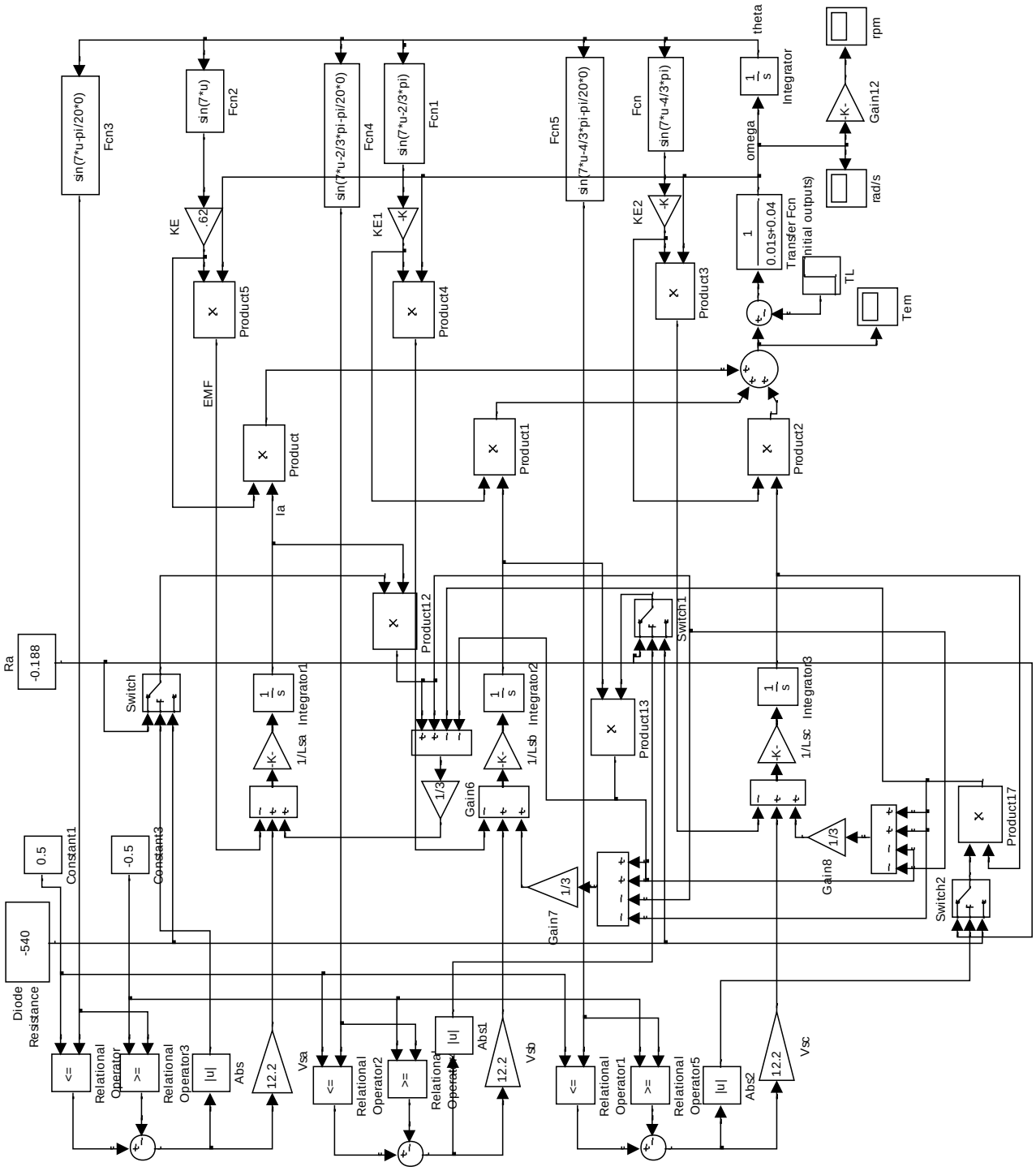

Fig. 9.7. Simulink model of the three-phase motor with supply circuit

Fig. 9.8 shows the electromagnetic torque waveform of the motor. The torque output increased to about 10.6 Nm when a load torque of 8.85 Nm is applied. The ripple in the torque waveform in this dynamic analysis can be contributed to the switching of transistors, that is, electronic commutation of currents between the phases.

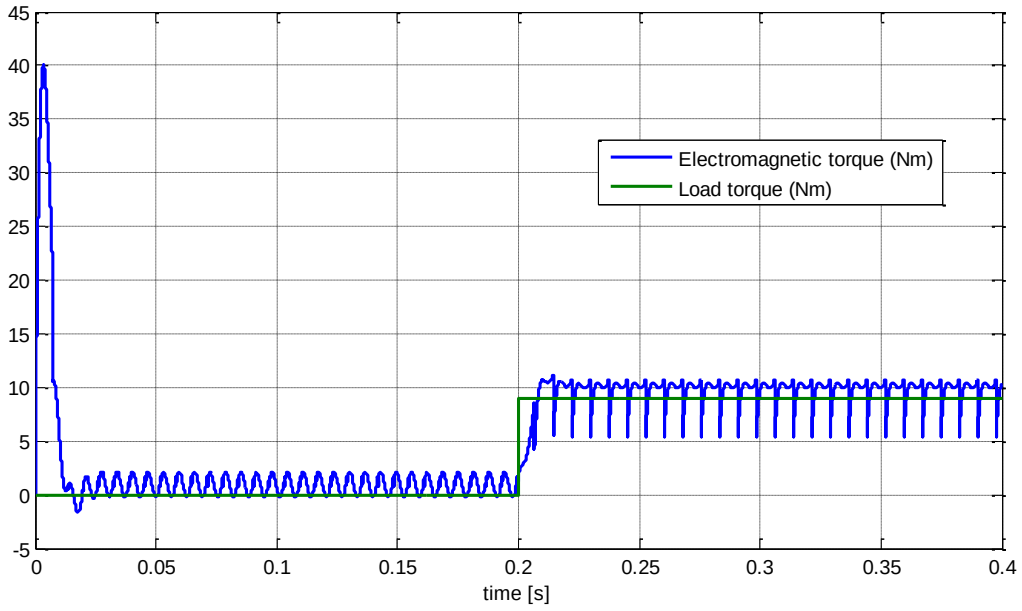

Fig. 9.8. Electromagnetic torque output of the wheelchair motor

The rotary speed characteristic of the wheelchair motor and the influence of load toque is shown in Fig. 9.9. As the load torque increased to 8.85 Nm at the time instant 0.2 s, the speed of the motor reduced from 223 rpm to approximately 186 rpm.

The armature current and phase voltage of the motor are shown in Fig. 9.10, and it can be inferred that the current waveform is square-wave shape, when load torque is applied. The ripple in the waveform is due to the switching of other two phases. As seen, a high current is drawn when the motor is under load and the current is almost zero when there is no load.

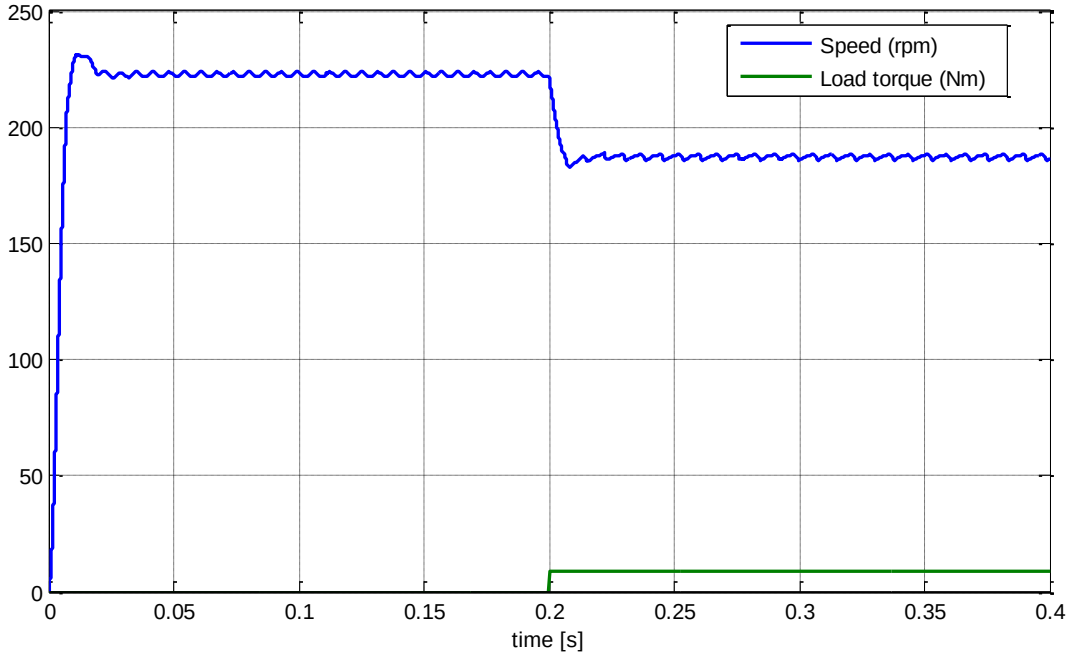

Fig. 9.9. Speed characteristic obtained from Simulink

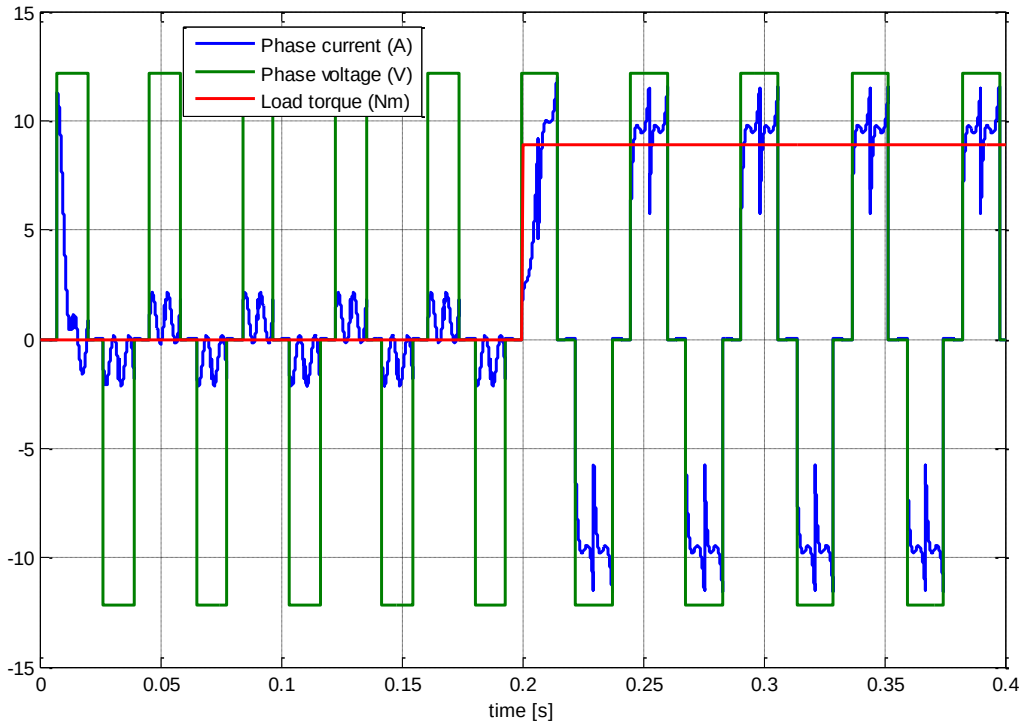

Fig. 9.10. Armature current and supply phase voltage

Fig. 9.11 shows the line-to-line supply voltage and induced EMF in the winding of the motor. The supply is a square wave voltage of 24.4 V and the induced EMF is sinusoidal in shape. The induced EMF is in phase with the armature current. A slight phase difference can be observed between the supply voltage and induced EMF. This is because the Simulink block diagram considers the practical scenario of delay caused due to switching of phases and includes a delay.

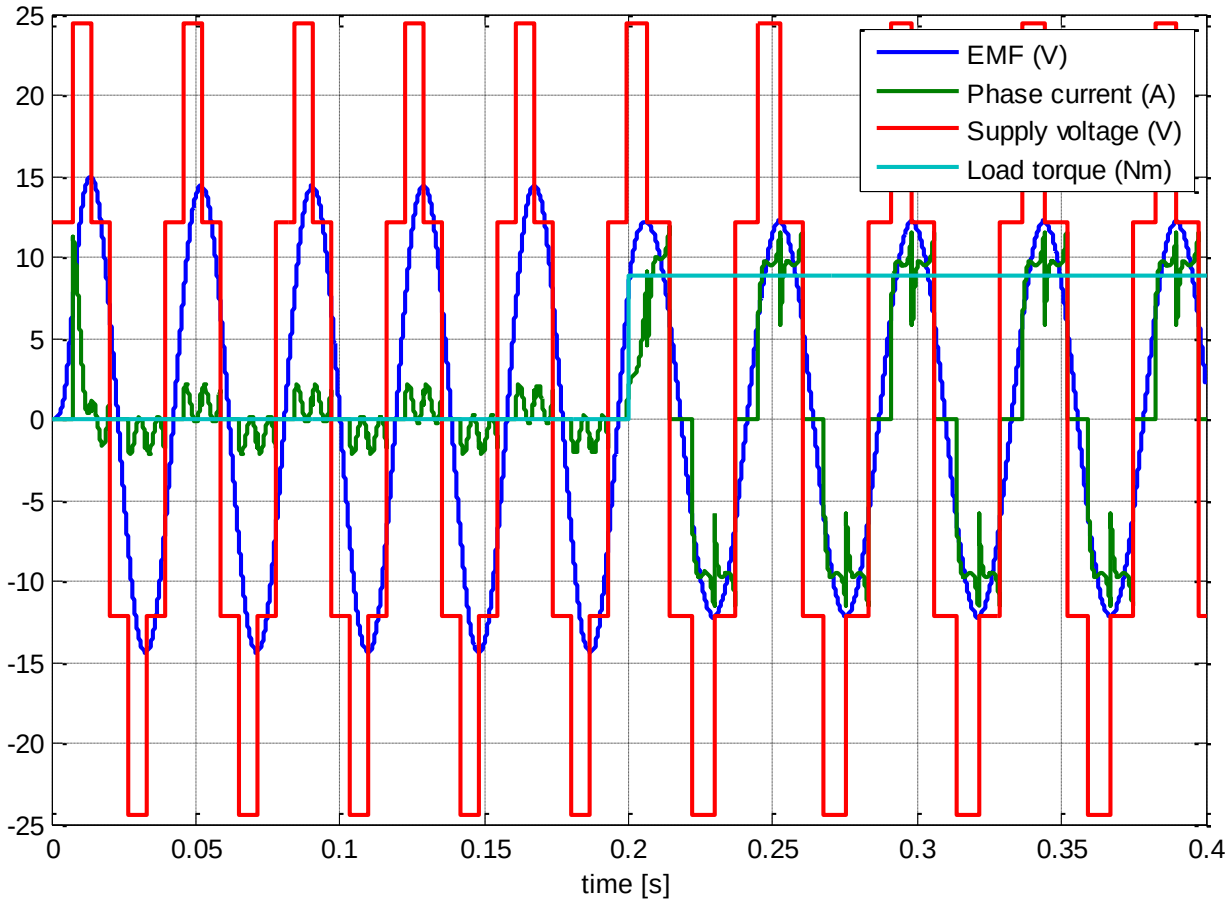

Fig. 9.11. Waveforms of line voltage, phase current and emf at no-load and load condition

The dynamic analysis from Simulink is validated using the prototype motor as discussed in the following subsection.

9.4 Experimental Results

A prototype of the outer-rotor cylindrical motor with slotted stator is manufactured for the gearless (direct) drive application of electric wheelchair. Pictures of wheelchair fitted with the in-wheel motor are shown in Figs. 9.12 (a) and (b). The motor with multi-layer armature winding is shown in Fig. 9.12 (c). Laboratory experiments are carried out to validate the FEM and Simulink results.

(a)

(b)

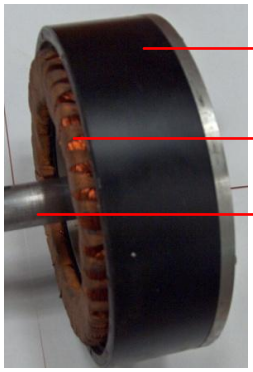

(c)

Fig. 9.12. (a) Electric wheel chair with the prototype in-wheel motor, (b) Cylindrical motor embedded into the wheel, (c) Single-rotor cylindrical motor for electric wheelchair

The experimental setup includes a supply source, which is a 24V DC battery, the prototype motor and a T20WN torque transducer from HBM to read the torque output. The motor is loaded by a permanent magnet DC generator. The torque transducer is supplied from a 12 V source. The torque output is sensed as a voltage signal ranging between -10 V and +10 V, the sign indicating the direction of rotation. Thus, the torque is calibrated as voltage in the case of T20WN and 10 V corresponds to 50 Nm. This voltage is read using Fluke meter. The laboratory set-up is shown in Fig. 9.13.

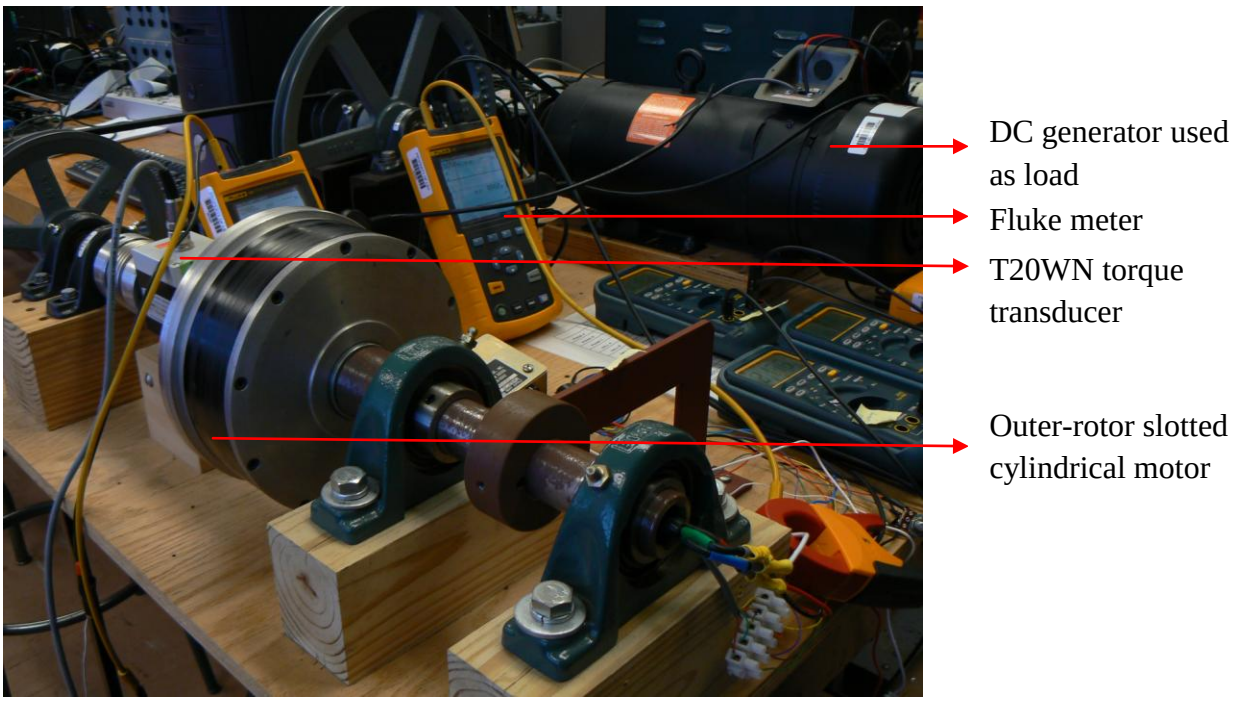

Fig. 9.13. Laboratory setup for wheelchair motor testing

The speed, current, efficiency and mechanical power characteristics of the wheelchair motor are experimentally determined at a supply voltage of 24 V and are plotted as a function of torque, which are shown in Fig. 9.14.

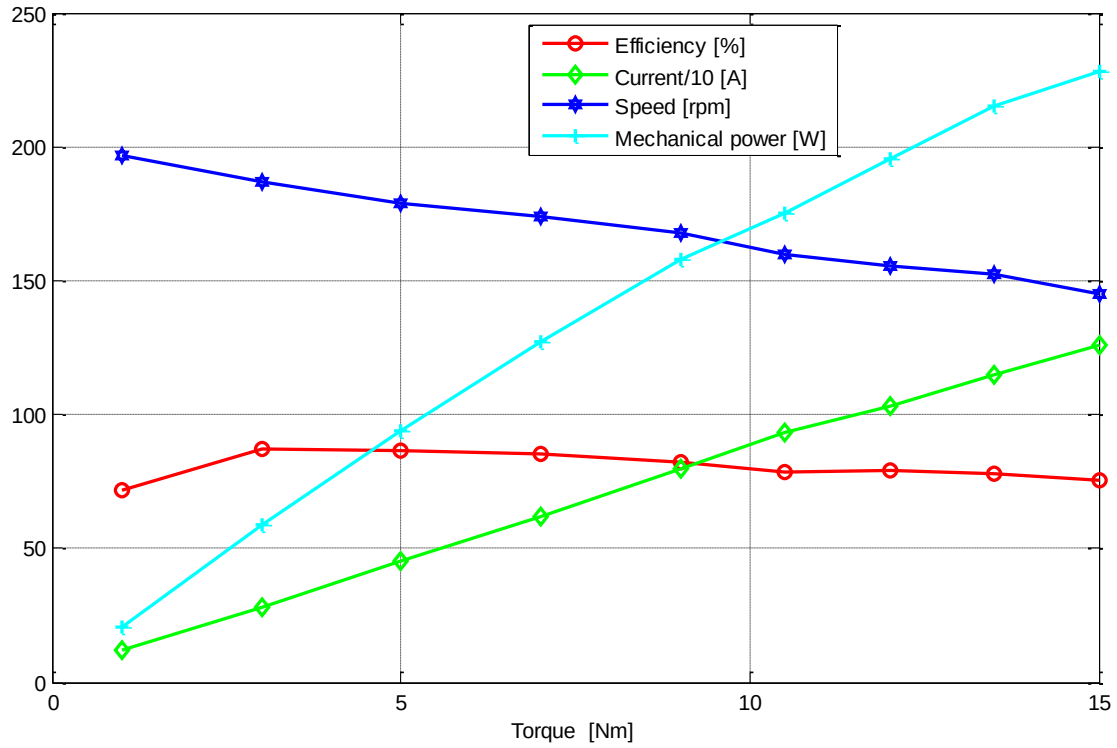

Fig. 9.14. Experimental characteristics of the wheelchair motor at steady-state at 24 V DC supply voltage

From this figure, it can be referred that the prototype motor developed a torque of 14.2 Nm at a rated current of 12 A. The efficiency of the motor at these conditions is about 76.8%. The torque value obtained from 3D FEM analysis in Maxwell 13 is 13.9 Nm. Thus, the error in the torque value computed from software is approximately 2%.

Figure 9.15 shows the current waveform obtained when the motor is supplied by 24.4 V and is loaded by a torque of 8.85 Nm. The waveform shape is close to trapezoidal or square wave indicating the operation of a PM brushless DC motor. The current waveform determined in no-load condition when the motor was supplied by 25.3 V is shown in Fig. 9.16 As seen, the peak current is about 9.6 A when the motor is loaded and is very low when the motor operates under no-load. The simulation results from Simulink are shown in Figs. 9.15 (a) and 9.16 (a). The

laboratory results are showed in Figs. 9.15 (b) and 9.16 (b). It can be observed that the simulation results and laboratory results are almost identical.

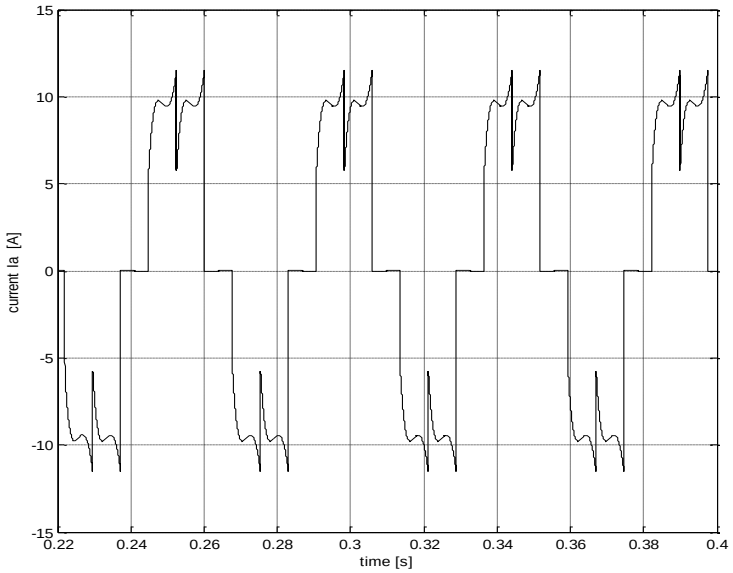

(a)

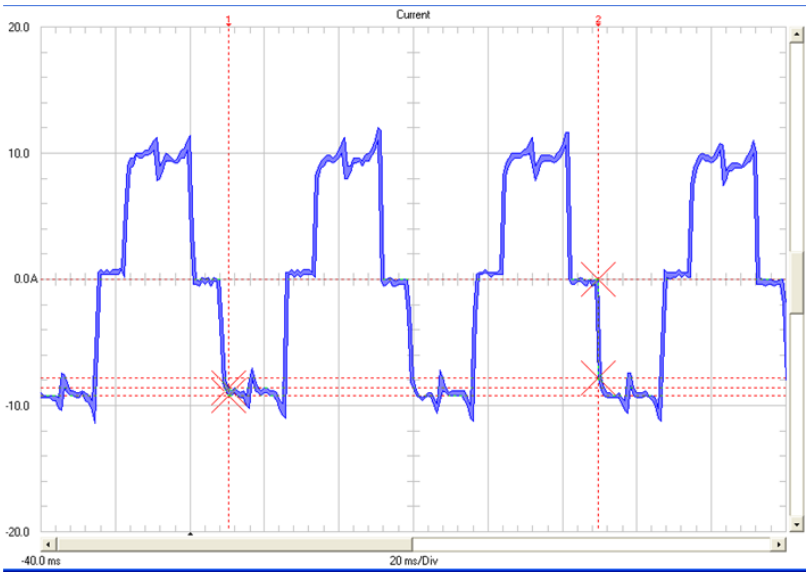

(b)

Fig. 9.15. Current waveform of prototype motor supplied by 24.4V with a load torque of 8.85Nm: (a) Simulation result, (b) Experimental result

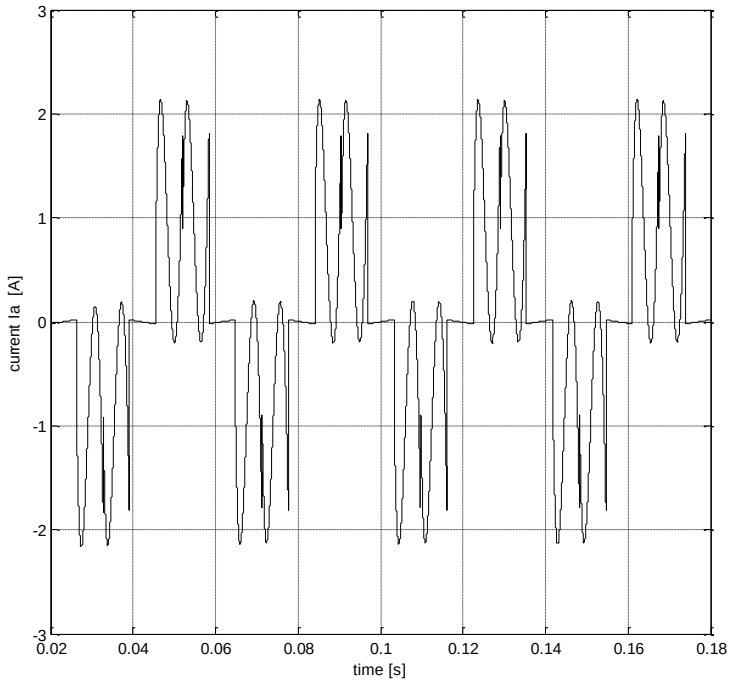

(a)

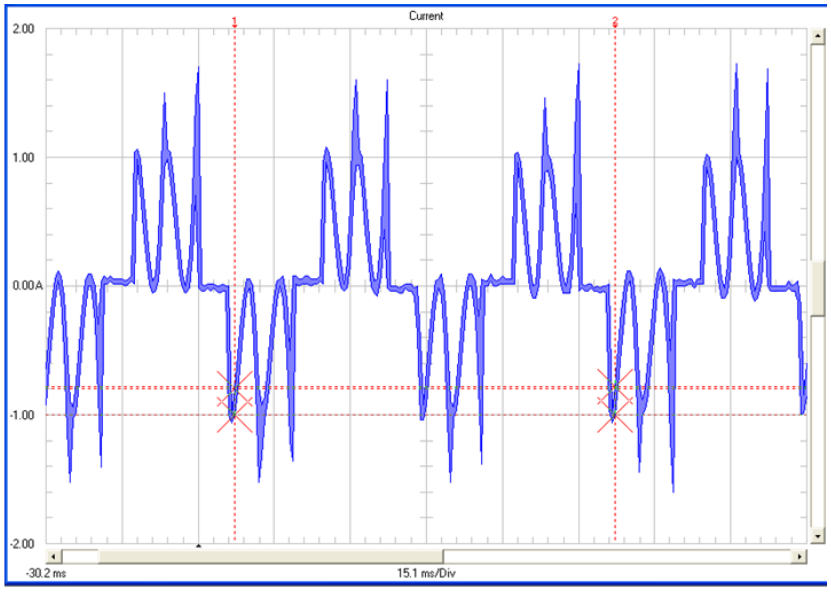

(b)

Fig. 9.16. Current waveform of prototype motor under no-load operation supplied by 25.3V: (a) Simulation result, (b) Experimental result

CHAPTER 10. CONCLUSIONS AND FUTURE SCOPE OF STUDY

10.1 Comparison of ECM and FEM Results

The Express Comparative Method is a software-free analytical approach to determine the torque output of axial flux twin-rotor PMBL motor, radial flux twin-rotor PMBL motor and single-rotor radial flux PMBL motor. It allows to evaluate the torque ratio of any two motors for a particular motor diameter and axial length at the assumption that the magnetic loading, electric loading and speed for all the three motors are the same.

In this dissertation, the ECM is validated using 3D FEM software, Maxwell 13. All the three motors are modeled and analyzed for an outer diameter of 334 mm and axial length of 82.5 mm. The magnetic loading is 0.7 T, electric loading is 41.5 A·turns/mm and the speed is 936 rpm for all the three motors. A few of the important design parameters for the AFTR, RFTR and single-rotor RF PMBL motors are listed in Table 10.1.

Table 10.1. Design data of the motors under comparison

Parameter	**AFTR PMBL**	**RFTR PMBL**	**Single-rotor RF PMBL**
Outer Diameter, r_o (mm)	334	334	334
Axial Length, l (mm)	82.5	82.5	82.5
Air gap flux density, B_{av} (T)	0.7	0.7	0.7
Current Density, J (A/mm^2)	4.56	4.56	4.56
Rated Current, I (A)	30.16	48	48
Number of magnetic poles, p	16	16	16
Number of coils, N_c	48	48	24
Number of turns per coil, N_t	17	13	15
Speed, ω (rpm)	936	936	936

The results from ECM, FEM and the computation error of ECM for the three motors are tabulated in Table 10.2.

Table 10.2. ECM results and validation

	ECM	**FEM**	**Error (%)**
AFTR PMBL motor torque	127.2 Nm	122.6 Nm	3.8
RFTR PMBL motor torque	181.2 Nm	179 Nm	1.2
Single-rotor RF PMBL motor torque	164.2 Nm	150.8 Nm	8.9
AFTR to RFTR torque ratio	0.7	0.69	1.5
Single-rotor RF to AFTR torque ratio	1.29	1.23	4.9
RFTR to Single-rotor RF torque ratio	1.1	1.19	-7.6

10.2 Conclusions

The objectives of this dissertation set in the Introduction chapter have been accomplished. In particular:

- An express method was developed for the comparison of slot-less axial flux and radial flux permanent magnet brushless motors for in-wheel motor application in electric vehicles.
- The analytical method was validated using 3D finite element modeling software, Maxwell 13. The error is higher in case of single-rotor RF PMBL motor due to larger end winding connection length (of an overlap winding). The end connection influence was not included in ECM. The error is less than 5 % in case of both AFTR and RFTR PMBL motors.

- The software Maxwell 13 was validated with the experimental results obtained from a prototype motor designed for gearless drive of an electric wheelchair. The error in the computation of torque by Maxwell 13 is found to be approximately 2%. However, the experimental and simulation results of the current match closely.

The conclusions deduced from the presented results are as follows:

- Among AFTR and RFTR PMBL motors, the RFTR PMBL motor provided a greater torque for wheel diameter greater than 167 mm. Among single-rotor RF and RFTR PMBL motors, the RFTR PMBL motor provided higher torque for diameters over 295 mm. The single-rotor RF PMBL motor is superior to AFTR PMBL motor for most of the wheel diameters except at very high diameter and very low axial length, where the AFTR PMBL motor gave better torque performance.
- The driving wheel of wheelchair is of 8″ in diameter and a motor of 194 mm outer diameter has been applied. For prototype, a single rotor RF PMBL motor was chosen because it gives higher torque than the other two motors at this particular diameter according to ECM.
- The efficiency of the wheelchair motor is found to be 76.8%, much higher than that of a traditional geared wheelchair.

10.3 Future Scope of Study

In the current dissertation, dimensions of end winding connection lengths are ignored. The ECM may be revised by considering the effect of end winding connection length. Also, similar method can be proposed for slotted PMBL motors.

BIBLIOGRAPHY

[1] P.H. Mellor, T. Allen, and D. Howe, "Hub-Mounted Electric Drive-Train for a High Performance All-Electric Racing Vehicle", *IEE Colloquium on Machines and Drives for Electric and Hybrid Vehicles (Digest No:1996/152),* 1996, Pages: 3/1 – 3/6.

[2] X.D. Xue, K.W.E. Cheng, and N.C. Cheung, "Selection of Electric Motor Drives for Electric Vehicles", *2008 Australasian Universities Power Engineering Conference (AUPEC'08).*

[3] Ernest A. Mendrela, *Introduction to Brushless DC Motors,* Lecture Notes, Louisiana State University, Baton Rouge, LA.

[4] Stephen J. Chapman, *Electric Machinery Fundamentals,* Fourth Edition, McGraw-Hill, New York, 2005.

[5] *Rare-Earth Permanent Magnets: Vacodym. Vacomax,* Edition 2007, VacuumSchmelze GmbH & Co. KG, Hanau

http://www.vacuumschmelze.de/fileadmin/documents/broschueren/dmbrosch/PD-002_e_310807.pdf

[6] E.A. Mendrela, M. Jagiela, R. Wrobel, "An Influence of Permanent Magnet Shape on the Torque Ripple of Disc-type Brushless DC Motors", *International Symposium on Electromagnetic Fields in Electrical Engineering,* Maribor, Slovenia, September 18-20, 2003

[7] G.S. Liew, N. Ertugrul, Wen Liang Soong, J. Gayler, "An Investigation of Advanced Magnetic Materials for Axial Field Brushless Permanent Magnet Motor Drives for Automotive Applications", *37th IEEE Power Electronics Specialists Conference,* 2006

[8] Jacek F. Gieras, Mitchell Wing, *Permanent Magnet Motor Technology - Design and Applications, Second Edition, Revised and Expanded,* Marcel Dekker Inc., New York.

[9] E.S. Hamdi, *Design of Small Electrical Machines,* John Wiley & Sons Ltd., England, 1994.

[10] Iqbal Husain, *Electric and Hybrid Vehicles – Design Fundamentals,* CRC Press LLC, Florida, USA, 2003.

[11] N. Bianchi, S. Bolognani, Ji-Hoon Jang, Seung-Ki Sul, "Advantages of Inset PM Machines for Zero-Speed Sensorless Position Detection", *IEEE Transactions on Industry Applications,* pp. 1190 - 1198, 2008.

[12] R. Vyas, S. Murthy, T. Sebastian, "Evaluation of brushless permanent magnet motor rotor configurations for square wave current excitation", *Proceeding of the 1996 International Conference on Power Electronics, Drives and Energy Systems for Industrial Growth,* Volume 2, pp. 895 – 899, 1996.

[13] J.S. Hsu, B.P. Scoggins, M.B. Scudiere, L.D. Marlino, D.J. Adams, P. Pillay, "Nature and Measurements of Torque Ripple of Permanent-Magnet Adjustable-Speed Motors", *Oak Ridge National Laboratory, US Department of Energy's Office of Scientific and Technical Information.*

[14] T. Li, G. Slemon, "Reduction of cogging torque in permanent magnet motors", *IEEE Transactions on Magnetics,* Volume 24, No. 6, November 1988.

[15] M.S. Islam, R. Islam, T. Sebastian, "Experimental verification of design techniques of permanent magnet synchronous motors for low torque ripple applications", *IEEE Energy Conversion Congress and Exposition 2009,* pp. 214 – 219.

[16] S. M. Hwang, D. K. Lieu, "Reduction of torque ripple in brushless dc motors", *IEEE Transactions on Magnetics,* Volume 31, No. 6, November 1995, pp. 3737 – 3739.

[17] A. N'diaye, C. Espanet, A. Miraoui, "Reduction of the troque ripples in brushless PM motors by optimization of the supply – Theoretical method and experimental implementation", *2004 IEEE International Symposium on Industrial Electronics,* Volume 2, pp. 1345 – 1350.

[18] S. Murthy, B. Derouane, B. Liu, T. Sebastian, "Minimization of torque pulsations in a trapezoidal back-emf permanent magnet brushless DC motor" *1999 IEEE Conference Record of the Industry Applications Conference,* Volume 2, pp. 1237 – 1242.

[19] P. Upadhyay, K.R. Rajagopal, "Effect of armature reaction and skewing on the performance of radial-flux permanent magnet brushless DC motor", *International Conference on Power Electronics, Drives and Energy Systems,* pp. 1 – 5, 2006.

[20] R. Carlson, M. Lajoie-Mazenc, J.C.dos S. Fagundes, "Analysis of torque ripple due to phase commutation in brushless dc machines", *IEEE Transactions on Industry Applications,* Volume 28, No. 3, pp. 632 – 638, May/June 1992.

[21] Y. Liu, Z.Q. Zhu, D. Howe, "Commutation-torque-ripple minimization in direct-torque-controlled PM brushless DC drives", *IEEE Transactions on Industry Applications,* Volume 43, No. 4, July/August 2007.

[22] X. Xi, W. Yufei, C. Jianyun, L. Yongdong, W. Xiangheng, "Performance analysis of multi-phase PM brushless DC motor drive system", *Sixth International Conference on Electrical Machines and Systems,* Volume 1, pp. 84 – 87, 2003.

[23] Pavani Gottipati, "Comparative study on double-rotor PM brushless motors with cylindrical and disc type slot-less stator", *Thesis Document, Louisiana State University,* August 2007.

[24] R. Krishnan, *Electric Motor Drives: Modeling Analysis, and Control,* Prentice Hall of India Private Limited, New Delhi, 2005.

[25] Jacek F. Gieras, Rong-Jie Wang, Maarten J. Kamper, *Axial Flux Permanent Magnet Brushless Machines,* Kluwer Academic Publishers, Netherlands, 2004.

[26] Z. Zhang, M. Santamaria, F. Profumo, A. Tenconi, "Analysis and Experimental Validation of an Axial Flux Brushless PM DC Motor Performance", *IEEE International Magnetics Conference,* pp. AQ-05 – AQ-05, 1997.

[27] Y.P. Yang, C.H. Cheung, S.W. Wu, J.P. Wang, "Optimal Design and Control of Axial-Flux Brushless DC Wheel Motor for Electric Vehicles", *Proceedings of the 10th Mediterranean Conference on Control and Automation – MED 2002,* Portugal, July 9 – 12, 2002.

[28] P.R. Upadhyay, K.R. Rajagopal, B.P. Singh, "Design of a Compact Winding for an Axial-Flux Permanent-Magnet Brushless DC Motor Used in an Electric Two-Wheeler", *IEEE Transactions on Magnetics,* Volume 40, No. 4, pp. 2026 – 2028, July 2004.

[29] B. Hredzak, S. Gair, "Elimination of Torque Pulsations in a Direct Drive EV Wheel Motor", *IEEE Transactions on Magnetics,* Volume 32, No. 5, pp. 5010 – 5012, September 1996.

[30] E.A. Mendrela, R. Beniak, R. Wrobel, "Influence of Stator Structure on Electromechanical Parameters of Torus-type Brushless DC Motor", *IEEE Transactions on Energy Conversion,* Volume 18, No. 2, pp. 231 – 237, June 2003.

[31] J.R. Mevey, "Sensorless Field Oriented Control of Brushless Permanent Magnet Synchronous Motors", *Thesis Document,* Department of Electrical and Computer Engineering, Kansas State University, 2009.

[32] R. Qu, T.A. Lipo, "Dual-Rotor, Radial-Flux, Toroidally Wound, Permanent Magnet Machines", *IEEE Transactions on Industry Applications,* Volume 39, No. 6, pp. 1665 – 1673, November/December 2003.

[33] R. Qu, T.A. Lipo, "Design and Optimization of Dual-Rotor, Radial-Flux, Toroidally-Wound, Permanent-Magnet Machines", *Industry Applications Conference,* Volume 2, pp. 1397 – 1404, October 2003.

[34] A. Toba, H. Ohsawa, Y. Suzuki, T. Miura, T.A. Lipo, "Experimental Evaluations of the Dual-Excitation Permanent Magnet Vernier Machine", *IPEC Conference Records,* Tokyo, pp. 1884 – 1889, April 3 – 7, 2000.

[35] A. Toba, T.A. Lipo, "Novel Dual-Excitation Permanent Magnet Vernier Machine", *IEEE - Industry Applications Conference Records,* Volume 4, pp. 2539 – 2544, August 2002.

[36] X. Liu, H. Lin, Z.Q. Zhu, C. Yang, S. Fang, J. Guo, "A Novel Dual-Stator Hybrid Excited Synchronous Wind Generator", *IEEE Transactions on Industry Applications,* Volume 45, No. 3, pp. 947 – 953, May/June 2009.

[37] S. Huang, M. Aydin, T.A. Lipo, "A Direct Approach to Electrical machine Performance Evaluation: Torque Density Assessment and Sizing Optimization", *International Conference on Electrical Machine,* ICEM 2002.

[38] A. Chen, R. Nilssen, A. Nysveen, "Performance Comparisons Among Radial-flux, Multistage Axial-Flux, and Three-Phase Transverse-Flux PM Machines for Downhole Applications", *IEEE Transactions on Industry Applications,* Volume 46, No. 2, pp. 779 – 789, March/April 2010.

[39] A. Parviainen, M. Niemela, J. Pyrhonen, J. Mantere, "Performance Comparison Between Low-Speed Axial-Flux and Radial-Flux Permanent-Magnet Machines Including Mechanical Constraints", *IEEE International Conference on Electric Machines and Drives,* pp. 1695 – 1702, 2005.

[40] E. Bomme, A. Foggia, T. Chevalier, "Double Air-Gaps Permanent Magnets Synchronous Motors Analysis", *International Conference on Electrical Machines,* pp. 1 – 5, September 2008.

[41] R. Qu, M. Aydin, T.A. Lipo, "Performance Comparison of Dual-Rotor Radial-Flux and Axial-Flux Permanent-Magnet BLDC Machines", *IEEE International Electric Machines and Drives Conference,* Volume 3, pp. 1948 – 1954, June 2003.

[42] V.I. Chrisanov, P. Szymczak, W. Kaminski, "The Generalized Geometric Approach to Comparative Study of Permanent Magnet Synchronous Machines and Mechatronic Modules", *12th International Power Electronics and Motion Control Conference,* pp. 1002 – 1007, September 2006.

[43] E. Mendrela, M. Lukaniszyn, K. Macek-Kaminska, *Disc-Type Brushless DC Motors,* Polish Academy of Science, 2002.

[44] A. Di Napoli, F. Caricchi, F. Crescimbini, G. Noia, "Design Criteria of a Low-Speed Axial-Flux PM Synchronous Machine," *International Conference on Evolution and Modern Aspects of Synchronous Machines,* Zurich, August 27-29, 1991.

[45] P. Paplicki, "Configurations of slotless permanent magnet motors with counter-rotating rotors for ship propulsion drives", *Przeglad Elektrotechniczny,* ISSN 0033-2097, R. 83 NR 11/2007.

[46] Pavani Gottipati, "Comparative study on double-rotor PM brushless motors with cylindrical and disc type slot-less stator", Thesis Document, Louisiana State University, Baton Rouge, August 2007.

[47] David Meeker, "Finite Element Method Magnetics, Version 4.2, User's Manual" November 26, 2009.

[48] Ansoft, "Maxwell v12 Magnetostatic Guide, Getting Started with Maxwell: Designing a Rotational Actuator", Ansoft Corporation, USA, February 2008.

[49] Federico Caricchi, Fabio Crescimbini, Fabio Mezzetti, Ezio Santini, "Multistage Axial-Flux PM Machine for Wheel Direct Drive", IEEE Transactions on Industry Applications, Volume 32, No. 4, pp. 882 – 888, July/August 1996.

APPENDIX A: M-FILES FOR ECM

(a) M-file for plotting torque ratios of any two motors by ECM, as shown in Figs. 5.10, 5.11 and 5.12

```
rmin=.10; lmin=0.070;
rmax=0.170; lmax=0.120;
r=rmin:rmax/100:rmax; %outer radius
l=lmin:lmax/100:lmax;
[r,l]=meshgrid(rmin:rmax/100:rmax,lmin:lmax/100:lmax);
d=2*r;
kio=0.613;
Cts=(r-3/4*l).*(2*r-l/2)./r.^2;
Cdt=r.^3*(Kio-Kio.^3)./l*(r-3/4*l).*(2*r-l/2);
Csd=l./r*(Kio-Kio.^3);
clf
figure(1),
surfc(d,l,Cts,'EdgeColor','None');
xlabel('diameter [m]');ylabel('length [m]');zlabel('Torque ratio');
title('Torque ratio of RFTR PMBL motor to single-rotor RF PMBL motor');
colorbar;
figure(2),
surfc(d,l,Cdt,'EdgeColor','None');
xlabel('diameter [m]');ylabel('length [m]');zlabel('Torque ratio');
title('Torque ratio of AFTR PMBL motor to RFTR PMBL motor');
colorbar;
figure(3),
surfc(d,l,Csd,'EdgeColor','None');
xlabel('diameter [m]');ylabel('length [m]');zlabel('Torque ratio');
title('Torque ratio of single-rotor RF PMBL motor to AFTR PMBL motor');
colorbar;
```

(b) M-file for plotting torque ratios for motors of length 82.5 mm, as shown in Fig. 5.13

```
%calculations of torque ratios of three types of motors. Each motor has the
%the same volume and outer diameter, no end connections of the winding are
%considered.

rmin=.08;
rmax=0.200;
r=rmin:rmax/100:rmax; %outer radius
Kio=0.613;
l=0.0825;
CTD=l*(r-3/4*l).*(2*r-l/2)./(r.^3*(Kio-Kio^3));     %Ctd=Tt./Td;
CTS=(r-3/4*l).*(2*r-l/2)./(r.^2);                   %Cts=Tt./Ts;
CDS=r*(Kio-Kio^3)./l;                          %Cds=Td./Ts;
Y1=1/1.4246;
Y2=1.1035;
Y3=1/0.7746;
```

```
X=0.334;
clf
figure(1),
plot(2*r,1./CTD,'r-',2*r,CTS,'b-',2*r,1./CDS,'k-
',X,Y1,'gp',X,Y2,'gp',X,Y3,'gp','LineWidth',3);

legend('AFTR to RFTR','RFTR to single-rotor RF','Single-rotor RF to
AFTR','Torque ratios at diameter 334mm');

text(0.32,0.78,'(0.334,0.702)');
text(0.34,1.05,'(0.334,1.1035)');
text(0.32,1.38,'(0.334,1.291)');
xlabel('Wheel Diameter (m)');
ylabel('Torque ratio');
title('Torque ratios from Express Comparative Method');
grid;
```

APPENDIX B: M-FILE FOR WHEELCHAIR MOTOR CHARACTERISTICS

(a) M-file for plotting steady-state experimental characteristics of prototype motor as shown in Fig. 9.14

```
% Performance Characteristics of Brushless DC Motor for wheelchair
% Measurement results
I=[1.2 2.8 4.5 6.2 8 9.3 10.3 11.5 12.6];
U=[24 24 24 23.8 23.7 23.7 23.6 23.5 23.4];
R=0.375;
M=[1 3 5 7 9 10.5 12 13.5 15];
OMEGA=(24-U)/1.12+pi/30*[197 187 179 172 165 157 152 148 140];
P=24*I;
Pm=M.*OMEGA;
n=OMEGA*30/pi;
Eff=Pm./P*100;

CLF;
figure(1),
plot(M,Eff,'ro-',M,10*I,'gd-',M,n,'bh-',M,Pm/1,'c+-','linewidth',2),grid,
xlabel('Torque  [Nm]'),
legend('Efficiency [%]','Current/10 [A]','Speed [rpm]','Mechanical power
[W]');
```

APPENDIX C: DATA TABLES FOR TORQUE RIPPLES

(a) Data table for plotting torque waveforms shown in Figs. 6.9, 7.7, 8.6

Note: Data only provided for rotation over one coil pitch with only few data points at an interval of 1.25 mechanical degrees or 10 electrical degrees

Mechanical Angle (deg)↓ / Torque (Nm)→	AFTR PMBL motor	RFTR PMBL motor	Single-rotor RF PMBL motor
0	129.71	183.2	157.08
1.25	126.88	179.2	154.06
2.5	119.92	177.56	147.55
3.75	115.38	174.84	144.6
5	120.86	178.49	146.27
6.25	125.88	181.84	152.74
7.5	127.38	183.04	156.03

(b) Data table for plotting torque waveform shown in Fig. 9.5

Note: Data only provided for rotation over one coil pitch with only few data points at an interval of 1.43 mechanical degrees or 10 electrical degrees

Mechanical Angle (deg)↓ / Torque (Nm)→	Wheelchair motor (without skew)	Wheelchair motor (with skew)
0	14.45	14.15
1.43	14	14.03
2.86	13.60	13.88
4.29	13.29	13.73
5.72	13.70	13.83
6.15	14.10	14.06
8.57	14.40	14.13

VITA

Pavani Gottipati was born, in 1983, in Gudivada, India. She received her Bachelor of Technology degree, with distinction in Instrumentation, from Andhra University, India in 2004. She graduated with a Master of Science in Electrical Engineering from Louisiana State University, U.S.A. in 2007. With a continued interest in the field of machine design, she joined the doctoral program at LSU, where she is currently a candidate for the degree of Doctor of Philosophy. She held internships with Visakhapatnam Steel Plant, India, and Otis Elevator Company, Connecticut, USA. She is currently working as a Teaching Assistant for the Department of Electrical and Computer Engineering at Louisiana State University, where she worked as a Research Assistant in the past. She is a graduate student member of IEEE and a collegiate member of Society of Women Engineers (SWE). Her fields of interest include modeling and finite element analysis of electric machines, simulation of motor dynamics, vehicle propulsion systems, permanent magnet machines and electric motor drives.